Velocity Field Measurements around Taylor Bubbles Rising in Stagnant and Upward Moving Liquids

A thesis submitted to the College of Graduate Studies and Research in partial fulfillment of the requirements for the degree of
Doctor of Philosophy
in the
Department of Mechanical Engineering
University of Saskatchewan

by

Gaballah SAAD

Permission to Use

In presenting this thesis in partial fulfillment of the requirements for a postgraduate degree from the University of Saskatchewan, I agree that the libraries of this University may make it freely available for inspection. I further agree that permission for copying of this thesis in any manner, in whole or in part, for scholarly purposes may be granted by the professor who supervised my thesis work or, in his absence, by the Head of the Department or the Dean of the College in which my thesis work was done. It is understood that any use of this thesis or parts thereof for financial gain shall not be allowed without my written permission. It is also understood that due recognition shall be given to me and to the University of Saskatchewan in any use which may be made of any material in my thesis.

Requests for permission to copy or to make other use of material in this thesis in whole or in part should be addressed to:

Head of the Department of Mechanical Engineering

University of Saskatchewan

Saskatoon, Saskatchewan S7N 5A9, Canada

Abstract

Gas-liquid, two-phase flow is encountered in a wide variety of industrial equipment. A few examples are steam generators, condensers, oil and gas pipelines, and various components of nuclear reactors. Slug flow is one of the most common and complex flow patterns and it occurs over a broad range of gas and liquid flow rates. In vertical tubes, most of the gas is located in large, bullet-shaped bubbles (Taylor bubbles) which occupy most of the pipe cross section and move with a relatively constant velocity. The objectives of this work are to increase our understanding of slug flow in vertical tubes, to provide reliable data for validation of numerical models developed to predict the behaviour of slug flow, to interpret the behaviour of Taylor bubbles based on knowledge of the velocity field, and to determine the shape of the Taylor bubbles rising in stagnant and upward flowing liquid under various experimental conditions.

To achieve these objectives, an experimental facility was designed and constructed to provide instantaneous two-dimensional (2-D) velocity field measurements using particle image velocimetry (PIV) around Taylor bubbles rising in a vertical 25 mm tube containing stagnant or upward moving liquids at Reynolds number based on the superficial liquid velocity (Re_L = 250 to 17,800). The working fluids were filtered tap water and mixtures of glycerol and water (μ = 0.0010, 0.0050 and 0.043 Pa·s) and air.

Mean axial and radial velocity profiles, axial turbulence intensity profiles, velocity vectors, and streamlines are presented for Taylor bubbles rising in stagnant and upward flowing

liquids. The measurements were validated by a mass balance around the nose of the bubble. In stagnant liquids, the size of the primary recirculation zone in the near wake of the Taylor bubble depends on the inverse viscosity. For low viscosity liquid, the length of the primary recirculation zone is 1.23*D* (*D* is the tube diameter), for the intermediate viscosity it is 1.2*D*, and for the high viscosity it is 0.68*D*. Based on the velocity measurements, the minimum stable liquid slug length (the minimum distance needed to re-establish a fully-developed velocity distribution in the liquid in front of the trailing Taylor bubble) for stagnant cases was found to be in the range of 2~12*D*.

In the flowing liquid, the flow structure of the wake depends on the relative motion between the two phases and the liquid viscosity. The wake is turbulent in all cases except at high viscosity where the wake is transitional. In general, the length of the primary recirculation zone increases with increasing liquid flow rate. For low viscosity cases, in a frame of reference moving at the bubble velocity, the length of the recirculation zone is 1.73*D* for Re_L =9,200 and become essentially constant at 1.90*D* for $Re_L \geq 13{,}600$. For the intermediate viscosity, the length of the recirculation zone is 1.22*D* for Re_L = 1,500. The length of the recirculation zone is increased to 1.34*D* for Re_L = 3,900. For the high viscosity, the length of the recirculation region is elongated to 1.4*D* for Re_L = 260. As the liquid flow rate increases the oscillations of the bottom surface increase and the number of small bubbles shed from the bubble bottom increases. The liquid slug minimum stable length for turbulent upward flowing liquid is around 12*D*. For laminar flow, the minimum stable length is 10*D* for Re_L = 260 (high viscosity) and > 28*D* for Re_L=1,500 (intermediate viscosity) and depends on the wake flow pattern and the liquid flow rate.

Acknowledgements

First of all, I thank God. I express my sincere gratitude to my supervisor, Professor Jim D. Bugg, for his support, advice, idea, and patience. I know that I would not have finished without his continued support.

My sincere thanks go to my advisory committee members; Professors D. Sumner, J. Kells and C. Simonson. Thanks should also go to Dave Deutscher for his technical assistance.

I gratefully acknowledge the financial support from a University of Saskatchewan Graduate Scholarship, the Department of Mechanical Engineering, the University of Saskatchewan, and the Libyan Ministry of Education.

Finally, I thank my family and friends for their emotional support and for putting up with my continued absence while I finished this thesis.

Dedication

To my parents, my wife, and my children.

Table of Contents

Permission to Use…… i
Abstract ……..….. ii
Acknowledgements……...…. iv
Dedication……. v
Table of Contents……..……. vi
List of Figures……..…… viii
List of Tables……..... xii
Nomenclature…… xiv
1 Introduction 1
1.1 Two-Phase Flow Patterns in Vertical Pipes..... 2
1.2 Scope of the research..... 5
1.3 Objectives..... 5
1.4 Thesis outline 6
2 Literature Review 7
2.1 Taylor Bubbles in Stagnant Liquids 7
2.2 Taylor bubbles in moving liquids 21
2.3 Summary..... 26
3 Experimental Apparatus and Instrumentation..... 34
3.1 Apparatus 34
3.1.1 Creating Taylor bubbles 36
3.1.2 Phase transition detectors 37
3.1.3 Optical correction box 38
3.2 Particle Image Velocimetry 39
3.2.1 Introduction 39
3.2.2 Flow Seeding Considerations 39
3.2.3 Light Sheet..... 42
3.2.4 Image Capture..... 43
3.2.5 PIV Image analysis 48
3.2.6 Uncertainty Analysis in PIV..... 52
3.3 Taylor Bubble Shape..... 56
3.3.1 Preliminary processing..... 57
3.3.2 Bubble shape measurements..... 58
3.4 Run Matrix..... 59
3.5 Experimental Procedure..... 60
3.6 The Mass Balance 61
3.7 Averaging Data 63
4 Taylor Bubbles Rising in Stagnant Liquids: Results and Discussion..... 65
4.1 Introduction 65
4.2 The Velocity Field Near The Nose And in the Film 67
4.3 Wakes of Taylor Bubbles Rising in Stagnant Liquids 72
4.3.1 Introduction 72
4.3.2 Mean Flow Field in the Wake..... 73
4.3.3 Axial Velocity Profiles..... 83
4.3.4 Radial Velocity Profiles 90

4.3.5 Axial Velocity Fluctuations..... 93
5 Taylor Bubbles Rising in Upward Flowing Liquids..... 96
5.1 Wakes of Taylor Bubbles Rising in Upward Flowing Water..... 96
5.1.1 Introduction 96
5.1.2 Mean Flow Field in the Near Wake 97
5.1.3 Axial Velocity Profiles 103
5.1.4 Radial Velocity Profiles..... 107
5.1.5 Axial Velocity Fluctuations Profiles..... 109
5.2 Wakes of Taylor Bubbles Rising in an Upward Flowing Mixture of Water and Glycerol (μ=0.005 Pa. S)..... 111
5.2.1 Introduction..... 111
5.2.2 Mean Flow Field in the Near Wake 113
5.2.3 Axial Velocity Profiles..... 116
5.2.4 Radial Velocity Profiles..... 120
5.2.5 Axial Velocity Fluctuations Profiles..... 121
5.3 Wakes Of Taylor Bubbles Rising in an Upward Moving Mixture of Water and Glycerol (μ=0.043 Pa.S)..... 123
5.3.1 Introduction..... 123
5.3.2 Mean Flow Field in the Near Wake 124
5.3.3 Axial Velocity Profiles 126
5.3.4 Radial Velocity Profiles..... 128
5.3.5 Axial Velocity Fluctuations..... 128
5.4 Effects of the Upward Flowing Liquid on the Wake 130
5.5 Effects of the Upward Flowing Liquid on the Bubble Shape..... 134
5.5.1 Nose Shape 134
5.5.2 Falling Film 136
5.5.3 Trailing Edge Oscillation 136
5.6 Bubble Coalescence 137
5.6.1 Stagnant Liquid 138
5.6.2 Laminar Upward Liquid Flow 140
5.6.3 Turbulent Upward Liquid Flow 141
6 Conclusions and Recommendations ……. 142
References 150
Appendix A: Taylor bubble terminal velocity..... 155
Appendix B: Shape of the bottom surface of Taylor bubbles at different flow conditions …….. 158

List of Figures

Figure		Page
1-1:	Flow regimes in vertical upward two-phase flow (http://drbratland.com/PipeFlow2).....	1
1-2:	Schematic of a Taylor bubble rising in a liquid.....	3
2-1:	The wake patterns of Taylor bubble rising in a stagnant liquid. (Pinto & Campos, 1988).....	13
3-1:	Schematic diagram of the apparatus used to create isolated Taylor bubbles in an upward-flowing liquid.....	35
3-2:	Light sheet generation using a spherical lens and a cylindrical lens.....	43
3-3:	A picture of the acrylic tube at the test section.....	46
3-4:	The PIV system and triggering components.....	46
3-5:	The timing diagram of the PIV system.....	47
3-6:	Three sequences of images (A, B and C) that cover the entire region behind the bubble.....	48
3-7:	Stages involved in PIV image analysis.....	49
3-8:	PIV analysis using the cross-correlation technique.....	51
3-9:	Sequence of image processing operations used to determine Taylor bubble shape.....	59
3-10:	Sketch of the control volume used to check the mass balance around a rising Taylor bubble.....	62
3-11:	The mean axial velocity at the centerline of the tube as a function of the distance from the bubble tail for both shifted and non-shifted images.....	64
3-12:	The axial turbulent intensity at the centerline of the tube as a function of the distance from the bubble tail for both shifted and non-shifted images…….	64
4-1:	Coordinate system for the velocity measurements presented in this thesis……....	66
4-2:	PIV measurements of the velocity field near the nose of a Taylor bubble rising in stagnant water (Case 1: Re_{TB} =4,400, N=12,600).....	68
4-3:	Axial velocity measurements along the tube axis above the nose of Taylor bubbles rising in stagnant liquids.....	69
4-4:	Radial profiles of axial velocity at four axial positions above the nose of a Taylor bubble rising in stagnant water (Case 1: Re_{TB} =4,400, N=12,600).....	71
4-5:	Radial profiles of radial velocity at four axial positions above the nose of a Taylor bubble rising in stagnant water (case 1: Re_{TB} =4,400, N=12,600)……..	71
4-6:	Radial profiles of axial velocity at four axial positions below the nose of a Taylor bubble rising in stagnant water (case 1: Re_{TB} =4,400, N=12,600)……..	72
4-7:	Shape of the bottom surface of Taylor bubbles rising in stagnant liquids: (a) Case 1 (Re_{TB} =4,400, N=12,600), (b) Case 2 (Re_{TB} =1,000, N=2,900) (c) Case 3 (Re_{TB} =120, N=350).....	74
4-8:	The mean velocity vectors and streamlines in the near wake of the Taylor bubble shown in a moving frame of reference (Case 1: Re_{TB} =4,400, N=12,600)	78
4-9:	The mean velocity vectors and streamlines in the near wake of the Taylor bubble shown in a moving frame of reference (Case 2: Re_{TB} =1,000, N=2,900).....	79

4-10: The instantaneous velocity vectors and streamlines in the near wake of the Taylor bubble shown in a moving frame of reference (Case 3: Re_{TB} =120, N=350)..... 80
4-11: Dividing streamlines for the three cases in a moving frame of reference……. 82
4-12: Effect of reference frame velocity on the visualization of this vortex for case 2 .. 83
4-13: Radial profiles of axial velocity at various axial positions in the wake of a Taylor bubble rising in stagnant water (case 1: Re_{TB} =4,400, N=12,600) ……. 85
4-14: Radial profiles of axial velocity at various axial positions in the wake of a Taylor bubble (case 2: Re_{TB} =1,007, N=2,900) 86
4 15: Radial profiles of axial velocity at various axial positions in the wake of a Taylor bubble (case 3: Re_{TB} =120, N=350) 86
4-16: Comparison of radial profiles of axial velocity at selected axial locations in the wake of Taylor bubble rising in stagnant liquids..... 89
4-17: Comparison of the axial velocity at the centreline of the tube in the wake of Taylor bubbles rising in stagnant liquids..... 89
4-18: Radial profiles of radial velocity at various axial positions in the wake of a Taylor bubble rising in stagnant water (Case 1: Re_{TB} =4,400, N=12,600) …… 90
4-19: Radial profiles of radial velocity at various axial positions in the wake of a Taylor bubble (Case 2: Re_{TB} =1,000, N=2,900) 91
4-20: Radial profiles of radial velocity at various axial positions in the wake of a Taylor bubble (Case 3: Re_{TB} =120, N=350). 91
4-21: Comparison of radial profiles of radial velocity at selected axial locations in the wake of Taylor bubble rising in stagnant liquids..... 92
4-22: Radial profiles of axial turbulence intensity at various axial positions in the wake of a Taylor bubble rising in stagnant water (case 1: Re_{TB} =4,400, N=12,600) 94
4-23: Radial profiles of axial turbulence intensity at various axial positions in the wake of a Taylor bubble (case 2: Re_{TB} =1,000, N=2,900). 94
4-24: Comparison of radial profiles of axial fluctuations at selected axial locations in the wake of Taylor bubble rising in stagnant liquids..... 95
5-1: Images of the bottom surfaces of Taylor bubbles rising in upward flowing water under the following conditions (a) Case 4 (Re_{TB} =15,400, Re_L =9,200) (b) Case 5 (Re_{TB} =20,700, Re_L =13,600) (c): Case 6 (Re_{TB} =25,800, Re_L =17,800) …… 98
5-2: The mean velocity vectors and streamlines in the near wake of the Taylor bubble shown in a moving frame of reference (case 4: Re_{TB} =15,400, Re_L =9,200). 100
5-3: The mean velocity vectors and streamlines in the near wake of the Taylor bubble shown in a moving frame of reference (case 5: Re_{TB} =20,700, Re_L =13,600)..... 101
5-4: The mean velocity vectors and streamlines in the near wake of the Taylor bubble shown in a moving frame of reference (case 6: Re_{TB} =25,800, Re_L =17,800)..... 102

5-5: Comparison of the axial velocity at the centreline of the tube in the wake of Taylor bubbles rising in upward moving water shown in a fixed frame of reference (cases 4, 5 and 6)……..... 104

5-6: Radial profiles of axial velocity at various axial positions in the wake of a Taylor bubble rising in turbulent flowing water (case 4: Re_{TB} =15,400, Re_L =9,200)..... 106
5-7: Radial profiles of axial velocity at various axial positions in the wake of a Taylor bubble rising in turbulent flowing water (case 5: Re_{TB} =20,700, Re_L =13,600)..... 106
5 8: Radial profiles of axial velocity at various axial positions in the wake of a Taylor bubble rising in turbulent flowing water (case 6: Re_{TB} =25,800, Re_L =17,800)..... 107
5-9: Radial profiles of radial velocity at various axial positions in the wake of a Taylor bubble rising in turbulent flowing water (case 4: Re_{TB} =15,400, Re_L =9,200)..... 108
5-10: Radial profiles of radial velocity at various axial positions in the wake of a Taylor bubble rising in turbulent flowing water (case 5: Re_{TB} =20,700, Re_L =13,600) 108
5-11: Radial profiles of radial velocity at various axial positions in the wake of a Taylor bubble rising in turbulent flowing water (case 6: Re_{TB} =25,800, ReL =17,800)..... 109
5-12: Radial profiles of axial turbulence intensity at various axial positions in the wake of a Taylor bubble rising in turbulent flowing water (case 4: Re_{TB} =15,400, Re_L =9,200)..... 110
5-13: Radial profiles of axial turbulence intensity at various axial positions in the wake of a Taylor bubble rising in turbulent flowing water case 5: Re_{TB} =20,700, Re_L =13,600)..... 110
5-14: Radial profiles of axial turbulence intensity at various axial positions in the wake of a Taylor bubble rising in turbulent flowing water (case 6: Re_{TB} =25,800, Re_L =17,800)..... 111
5-15: Bottom surfaces of Taylor bubbles rising in an upward flowing mixture of water and glycerol: (a) Case 7 (Re_{TB} =3,800 & Re_L =1,200) (b) Case 8 (Re_{TB} =5,700 & Re_L =3,900)..... 113
5-16: Mean velocity vectors and streamlines in the near wake of the Taylor bubble shown in a moving frame of reference (case 7: Re_{TB} =3,800, Re_L =1,200) 114
5-17: Mean velocity vectors and streamlines in the near wake of the Taylor bubble shown in a moving frame of reference (case 8: Re_{TB} =5,700, Re_L =3,900)…….. 115
5-18: Comparison of the axial velocity at the centreline of the tube in the near wake of Taylor bubbles rising in an upward moving liquid (case 7 and case 8)……. 117
5-19: Radial profiles of axial velocity at various axial positions in the wake of a Taylor bubble rising in laminar flowing liquid (case 7:Re_{TB} =3,800, Re_L =1,200) 119
5-20: Radial profiles of axial velocity at various axial positions in the wake of a Taylor bubble rising in turbulent flowing liquid (case 8:Re_{TB} =5,700,Re_L =3,900)…… 119
5-21: Radial profiles of radial velocity at various axial positions in the wake of a Taylor bubble rising in laminar flowing liquid (case 7:Re_{TB} =3,800, Re_L =1,200) 120
5 22: Radial profiles of radial velocity at various axial positions in the wake of a Taylor bubble rising in a turbulent flowing liquid (case 8: Re_{TB} =5,700, Re_L =3,900) 121

5-23: Radial profiles of axial turbulence intensity at various axial positions in the near wake of a Taylor bubble rising in laminar flowing liquid (case 7: Re_{TB} =3,800, Re_L =1,200)…… 122
5-24: Radial profiles of axial turbulence intensity at various axial positions in the near wake of a Taylor bubble rising in turbulent flowing liquid with (case 8: Re_{TB} =5,700, Re_L =3,900)..... 122
5-25: Bottom surface of a Taylor bubble rising in upward flowing mixture of water and glycerol: Case 9 (Re_{TB} =620 & Re_L =260)..... 124
5-26: Mean velocity vectors and streamlines in the near wake of the Taylor bubble shown in a moving frame of reference (case 9: Re_{TB} =620, Re_L =260)……. 125
5 27: Axial velocity at the tube centreline in wake of Taylor bubble rising in upward laminar flow (case 9: Re_{TB} =620, Re_L =260)…….. 127
5-28: Radial profiles of axial velocity at various axial positions in the wake of a Taylor bubble rising in laminar flowing liquid (case 9: Re_{TB} =620, Re_L =260)…. 127
5-29: Radial profiles of radial velocity at various axial positions in the wake of a Taylor bubble rising in laminar flowing liquid (case 9: Re_{TB} =620, Re_L =260)…. 129
5 30: Radial profiles of axial turbulence intensity at axial positions in the wake of a Taylor bubble rising in laminar flowing liquid (case 9: Re_{TB} =620, Re_L=260)… 129
5-31: Dividing streamlines for the low viscosity cases..... 132
5 32: Dividing streamlines for (a): the intermediate viscosity cases (b): the high viscosity cases……. 133
5-33: Bubble shape counter for the intermediate viscosity in stagnant, laminar and turbulent flows)..... 135
5-34: Schematic diagram of two Taylor bubbles rising in a vertical tube shown in a fixed frame of reference)..... 139
A-1: The velocity of Taylor bubbles rising in stagnant water……..…….. 155
A-2: The velocity of Taylor bubbles rising in Concurrent upward flowing water……. 156
B-1: Shape of the bottom surface of Taylor bubbles rising in stagnant liquid Case 1 (Re_{TB} =4,400, N=12,600)…….. 157
B-2: Shape of the bottom surface of Taylor bubbles rising in stagnant liquid Case 2 (Re_{TB} =1,000, N=2,900)…… 158
B-3: Shape of the bottom surface of Taylor bubbles rising in stagnant liquid Case 3 (Re_{TB} =120, N=350)……..……. 159
B-4: Images of the bottom surfaces of Taylor bubbles rising in upward flowing water under case 4 (Re_{TB} =15,400, Re_L =9,200)..... 160
B-5: Images of the bottom surfaces of Taylor bubbles rising in upward flowing water 5 (Re_{TB} =20,700, Re_L =13,600) 161
B-6: Images of the bottom surfaces of Taylor bubbles rising in upward flowing water Case 6 (Re_{TB} =25,800, Re_L =17,800)…….. 162
B-7: Bottom surfaces of Taylor bubbles rising in an upward flowing mixture of water and glycerol: (a) Case 7 (Re_{TB} =3,800 & Re_L=1,500) 163
B-8: Bottom surfaces of Taylor bubbles rising in an upward flowing mixture of water and glycerol case 8 (Re_{TB} =5,700 & Re_L=4,000) ……..…….. 164
B-9: Bottom surface of a Taylor bubble rising in upward flowing mixture of water and glycerol: Case 9 (Re_{TB}=620 & Re_L=25) ……. 165

List of Tables

Table	page
2-1: Summary of experimental and theoretical studies for Taylor bubbles rising in vertical tubes…….……	28
3-1: Summary of uncertainty in data results:…….	56
3-2: List of experimental parameters for Taylor bubble velocity field measurements……...	60
4-1: Experimental conditions for the study of Taylor bubbles rising in stagnant liquids……...	66
4-2: Summary of the main vortex parameters for the stagnant cases……	81
5-1: Experimental conditions for Taylor bubbles in flowing water……..	97
5-2: Summary of the primary recirculation zone parameters for cases 4, 5 and 6…	103
5-3: Experimental conditions for Taylor bubbles rising in a flowing water-glycerol mixture (μ=0.005 Pa•s)……..	112
5-4: Summary of the primary recirculation zone parameters for cases 7 and 8……	116
5-5: Experimental conditions of Taylor bubbles in a flowing water-glycerol mixture (μ=0.043 Pa•s)……	123
5-6: Summary of the primary recirculation zone parameters for case 9……...	126
5-7: Summary of the primary recirculation zone parameters for all cases……	131
5-8: Some minimum stable liquid slug length results from the literature…….	138

Nomenclature

Roman

$C(\vec{s})$	cross-correlation function
b_V	systematic standard uncertainty in the velocity
C	velocity coefficient in equation (2.18)
c_1	velocity coefficient in equation (2.17)
D	tube diameter
d_p	particle diameter
E_O	Eötvös number
Fr	Froude number
g	acceleration due to gravity
IA	interrogation area
l_{min}	minimum liquid slug length required for no interaction between two bubbles
l_s	minimum bubble length required for a fully-developed liquid film
l_w	near wake length
M	Morton number
N	inverse viscosity number
R	tube radius
r	distance from the tube centre
Re_f	Reynolds number based on the liquid film velocity
Re_L	Reynolds number based in superficial liquid velocity
Re_R	Reynolds number based on the velocity of the liquid relative to the bubble
S_V	random standard uncertainty in the velocity

U velocity

U_{cl} liquid centreline velocity

U_L mean superficial liquid velocity

U_m mixture velocity

U_t particle terminal velocity

U_{TB} Taylor bubble terminal velocity

V_w wake volume

V_Z axial velocity component

Z distance from the bubble bottom

z distance from the bubble nose

Greek

α calibration factor

ΔT separation time between the two laser pulses

ΔX average particle displacement

δ equilibrium film thickness

μ liquid dynamic viscosity

ρ liquid density

ρ_G gas density

ρ_p particle density

σ surface tension

1 Introduction

1.1 Two-Phase Flow Patterns in Vertical Pipes

Two-phase flow is encountered in a wide variety of industrial equipment. A few examples are steam generators, condensers, oil and gas pipelines, and various components of nuclear reactors. The gas and liquid is distributed in the pipe in configurations called flow patterns or flow regimes. The flow regime is determined by the fluid properties, the flow rates, and the orientation of the tube. The basic flow regimes that exist in upward gas-liquid flow are illustrated in Figure 1-1. These flow regimes are described for increasing gas flow rate, as follows:

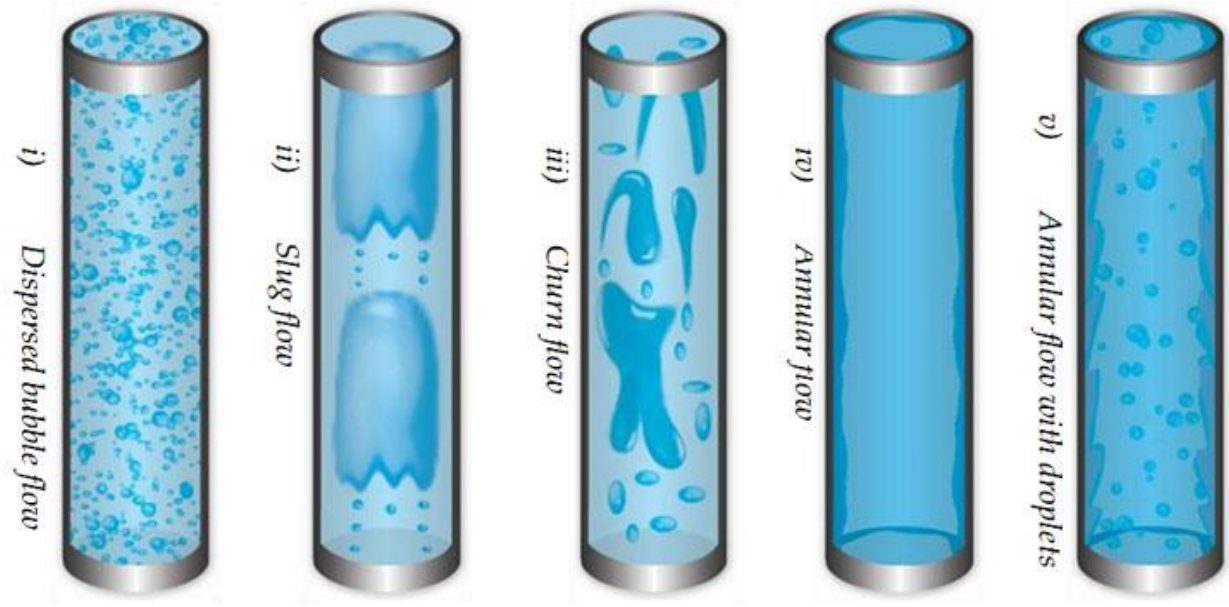

Figure 1-1: Flow regimes in vertical upward two-phase flow (http://drbratland.com/PipeFlow2)

- ***Bubbly flow:*** The liquid is the continuous phase and the gas is dispersed fairly uniformly in the form of small bubbles.
- ***Slug flow:*** As the gas flow rate is increased, the small bubbles coalesce to form large bullet-shaped bubbles called Taylor bubbles. The liquid slugs between these bubbles often contain many small bubbles. This is the flow regime of interest in the thesis.
- ***Churn flow:*** A highly disordered flow with oscillating vertical liquid motion of the liquid. The gas bubbles become irregularly shaped destroying the continuity of the liquid slug.
- ***Annular flow:*** This regime consists of an annular wavy liquid film (Figure 1-1 (iv)) which may contain small bubbles and a gas core which usually contains liquid droplets (Figure 1-1 (v)).

Slug flow is a common flow pattern and occurs over a large range of gas and liquid flow rates. The existence of slug flow can be dangerous due to the high momentum of liquid slugs. This can cause severe damage to large piping structures (Fabre and Line, 1992). In vertical tubes, large bullet-shaped bubbles occupy most of the pipe cross section and move with a relatively constant velocity. Figure 1-2 shows a schematic of a Taylor bubble. A thin film of liquid flows between the Taylor bubble and the pipe wall. When the liquid film penetrates into the liquid slug behind the bubble, it creates vortices and intense mixing. The liquid slug may or may not contain a dispersion of small gas bubbles. The size and structure of the wake behind a Taylor bubble depends on the liquid properties and the tube diameter as well as the relative motion between the bubble and the background flowing liquid. The interaction between consecutive Taylor bubbles is important to the development of slug flow. In general,

it is assumed that the trailing bubble nose is affected by the velocity field in the liquid ahead of it. The wake of the leading bubble strongly affects the shape and the velocity of the trailing bubble. Therefore, a detailed understanding of the hydrodynamics of Taylor bubble wakes is very important to the task of modeling slug flow.

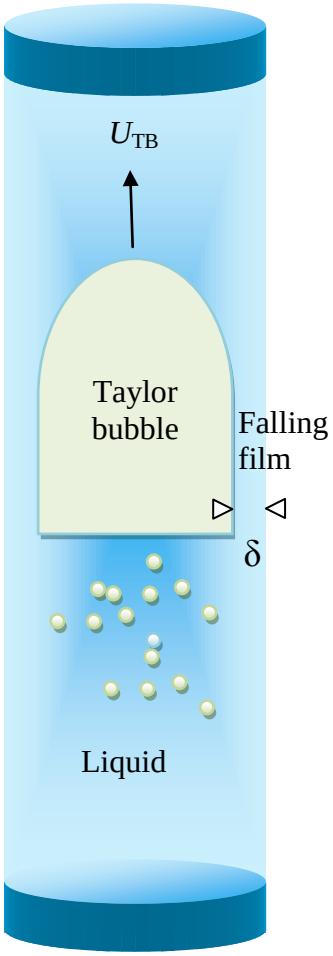

Figure 1-2: Schematic of a Taylor bubble rising in a liquid

Knowledge of the velocity field is important in understanding the physical nature of two-phase flow regimes. It also helps to more clearly understand the fluid dynamic and heat transfer characteristics of these flows. Particle Image Velocimetry (PIV) is a full-field velocity measurement technique which makes non-intrusive velocity measurements at thousands of points simultaneously. For this reason, it is well-suited to studying spatial variations in the velocity field. A PIV system consists of a two-dimensional light sheet to illuminate the flow field, seeding particles in the flow to scatter the light, an image recording device to record the position of the particles, and a system for analyzing the image to determine the particle motion. The illumination is pulsed twice and the resulting particle images are recorded using digital cameras. Knowing the time between the illumination pulses, the instantaneous velocity can be determined from the measured particle displacement. The fluid velocity is estimated from the motion of the seed particles. The ability of PIV to capture whole-field instantaneous velocity data non-invasively provides a powerful tool to achieve reliable high-quality experimental data. The presence of the bubble is a challenge in making a velocity measurement in the liquid around Taylor bubbles due the intense laser reflection caused by the gas-liquid interface. This reflection affects the measurement of bubble shape and the liquid velocity measurements close to the interface. Also, optical distortions due the tube wall curvature make the velocity measurement close to the wall difficult. Another challenge is that the bubble is moving. Therefore, a technique is needed to trigger the PIV system components based on the bubble position.

1.2 Scope

This experimental study concentrates on a simplified form of the slug flow regime for vertical flow. It considers the case of a single Taylor bubble rising in stagnant or upward flowing liquids in a vertical tube in both laminar and turbulent flow. To achieve good PIV measurements in the wake of the bubbles, special care is taken to produce Taylor bubbles with wakes that are free of small bubbles.

1.3 Objectives

The overall objectives of this of this work are to increase our understanding of slug flow in vertical tubes and to provide reliable data for validation of numerical models developed to predict the behaviour of slug flow. The main objectives of this research are:

1. To make detailed velocity field measurements in the liquid around Taylor bubbles rising in stagnant and upward flowing liquid using Particle Image Velocimetry (PIV).
2. To interpret the behaviour of Taylor bubbles based on knowledge of the velocity field. For example, the mechanism of Taylor bubble coalescence depends heavily upon the velocity field in the wake of the bubbles.
3. To determine the shape of the Taylor bubbles rising in stagnant and upward flowing liquid using digital photography and image processing, and to discuss the influence of this shape on the velocity field and wake structure.

1.4 Thesis Outline

The outline of this thesis is as follows. In Chapter 2, a review of some previous investigations of slug flow and Taylor bubbles is presented. Chapter 3 describes the experimental method which was used to achieve successful PIV measurements around Taylor bubbles. Chapter 4 presents the experimental results for Taylor bubbles rising in stagnant liquids. Chapter 5 presents the experimental results for Taylor bubbles rising in upward flowing liquids. Finally, Chapter 6 concludes the thesis and presents suggestions for future study.

2 Literature Review

Slug flow has been studied both theoretically and experimentally by numerous researchers. A literature review for slug flow in vertical tubes is introduced in the following paragraphs. The first part of this literature review focuses on Taylor bubbles rising in stagnant liquids and the second part discusses Taylor bubbles rising in upward moving liquids. This review is mainly focused on experimental works.

2.1 Taylor Bubbles in Stagnant Liquids

When a large volume of gas rises in an unconfined liquid it takes on a spherical-cap shape. The upper surface is almost perfectly spherical and the lower surface is flat. The rise of a spherical cap bubble through stagnant ideal fluid (i.e. one without viscosity or surface tension) in a large tank was first treated theoretically by Davies and Taylor (1950). Using potential flow theory and considering the bubble nose as a sphere, they expressed the velocity near the nose of the bubble as

$$q^2 = \frac{9}{4}U^2 sin^2\theta, \tag{2.1}$$

where q is the local liquid velocity relative to the bubble, U is the rise velocity of the bubble and θ is a polar coordinate specifying the position from the leading edge stagnation point. Applying Bernoulli's equation and considering the pressure inside the bubble constant yields

$$q^2 = 2gz, \tag{2.2}$$

where z is the vertical distance measured downward from the nose and g is the acceleration due to the gravity. Substituting 2.2 into 2.1 for small θ yields

$$U = \frac{\sqrt{2}}{3}\sqrt{gD_{\mathrm{b}}} = 0.471\sqrt{gD_{\mathrm{b}}}\,, \qquad 2.3$$

where D_{b} is the bubble diameter. They also modified equation 2.3 taking into account the bubble rise in a confined pipe. They obtained the same result as equation 2.3 but with a constant of 0.328 and the tube diameter D instead of 0.471 and D_{b}. Other workers achieved the same result as equation 2.3 with a constant of 0.35 so that

$$U = 0.35\sqrt{gD} = U_{\mathrm{TB}}, \qquad 2.4$$

where D is the tube diameter and U_{TB} is the Taylor bubble rise velocity.

White and Beardmore (1962) undertook a systematic experimental investigation of the rise velocity of Taylor bubbles in a variety of stagnant liquids in vertical tubes. They presented their experimental results in terms of the following dimensionless groups:

$$Fr = \frac{U_{\mathrm{TB}}}{\sqrt{gD(\rho - \rho_{\mathrm{G}})}} \qquad 2.5$$

$$Eo = \frac{gD^2(\rho - \rho_{\mathrm{G}})}{\sigma} \qquad 2.6$$

$$M = \frac{g\mu^4(\rho - \rho_{\mathrm{G}})}{\rho^2\sigma^3} \qquad 2.7$$

where the Froude number, *Fr*, represents the ratio of inertia to gravity forces, the Eötvös number, *Eo*, represents the ratio of the gravity forces and the surface tension, and the Morton number, *M*, is a property group which is mainly governed by the liquid viscosity. In these groups, μ is the liquid viscosity, ρ is the liquid density, σ is the surface tension, ρ_G is the gas density, g is the acceleration due to gravity, and U_{TB} is the terminal velocity of the bubble. White and Beardmore (1962) represented the effect of the inertial, viscous, gravitational, and

interfacial forces in a graphical correlation of Froude number as a function of Eötvös number and Morton number covering the range $3 < Eo < 400$ and $10^{-12} < M < 10^{3}$. They indicated that viscous forces are negligible if $Eo > 70$, inertia forces are negligible if $Fr < 0.05$ and the bubble will not rise unless $Eo > 4$. They showed that the bubble rise velocity is well predicted by equation 2.4 when viscosity and surface tension effects are negligible.

Moissis and Griffith (1962) realised the technical difficulties in measuring the velocity profiles behind an air bubble. In order to overcome these obstacles, they simulated the actual flow by placing a plastic model of a Taylor bubble suspended in a pipe with a downflow of water and measured the velocity using a Pitot tube in the wake of the model. They made an important observation. When two bubbles rise close together, the trailing bubble shape and velocity is affected by the flow field ahead of it which results from the leading bubble wake. They concluded that the minimum separation distance between the two bubbles needs to be about 8-16 tube diameters for there to be no effect on the trailing bubble.

Goldsmith and Mason (1962) experimentally and theoretically studied Taylor bubbles rising in viscous flow (*Re* varies from 10^{-5} to 1.0 and the dimensionless group $\left(\frac{U_{TB}\mu}{\sigma}\right)$ from 2×10^{-4} to 2×10^{-2}). They came up with expressions for the velocity profiles in both phases. They related the film thickness to the bubble velocity in viscous flow. They also studied the shape of the bubbles and showed that the ends of the bubble are prolate and oblate spheroids. The exact shape was dependant on surface tension.

Brown (1965) developed a model to predict the velocity around a Taylor bubble rising in a stagnant liquid. He modified the potential flow solution by Davies and Taylor (1950) to account for the effect of the liquid viscosity in the film around the bubble. He considered the film region as a steady, laminar falling film and came up with the following expression for the velocity in the film,

$$u = \frac{g\rho}{\mu}\left[\frac{R^2 - r^2}{4} - \frac{(R-\delta)^2}{2}\ln\frac{R}{r}\right], \tag{2.8}$$

where u is the velocity in the film (relative to the wall), R is the tube radius, μ is the viscosity of the liquid, and δ is the equilibrium film thickness where the film gravity forces are balanced by the wall shear stress. This expression is equivalent to that obtained by Goldsmith and Mason (1962). He also gave an expression for δ valid for rather large tubes (D > 20 mm) as follows.

$$\delta = \left[\frac{3\mu}{2g\rho}U_{\mathrm{TB}}(R-\delta)\right]^{1/3} \tag{2.9}$$

This may be simplified further to

$$\delta = \left[\frac{3\mu R U_{\mathrm{TB}}}{2g\rho}\right]^{1/3}, \tag{2.10}$$

if $\delta << R$.

Zukoski (1966) performed an experimental study of the motion of Taylor bubbles in closed tubes at various angles of inclination. The experiment was carried out with a number of fluids and with a number of tube diameters. He studied the influence of surface tension, viscosity and tube inclination on the terminal velocity. He reported that the terminal velocity of the

bubble reaches a maximum value at intermediate angles of inclination, around 40° to 60° from the horizontal. The effect of the surface tension can be substantial, particularly for small-diameter tubes. The terminal velocity decreases considerably with increasing surface tension and decreasing tube diameter. The effect of viscosity can be neglected for Reynolds number (based on bubble velocity and tube diameter) greater than 200.

Campos & Guedes de Carvalho (1988) photographically studied the wake region behind rising Taylor bubbles in tubes of 19-25 mm diameter. The bottom half of these tubes was filled with a coloured liquid while the top half was filled with a clear liquid. When the bubble rose through the colored liquid into the clear liquid a photograph was taken which was used to help determine the structure of the wake. They pointed out that the flow pattern in the wake of a gas bubble rising in a vertical tube is likely to depend on the tube diameter, D, the viscosity, μ, liquid density, ρ, the surface tension, σ, the acceleration due to gravity, g, and the length of the bubble, l_s. Their dimensional analysis shows that the dimensionless wake volume V_w/D^3 and the dimensionless wake length l_w/D depend on l_s/D and N (the dimensionless inverse viscosity) where

$$N = \frac{(g\rho D^3(\rho - \rho_G))^{1/2}}{\mu} \quad . \qquad 2.11$$

To simplify the analysis, they took into account two important considerations. First, except for D < 20 mm, the dependence of the wake on Eötvös number is negligible. Second, the dimensionless wake parameters are independent of bubble length if the flow in the liquid film is fully developed. They estimated the minimum bubble length required for a fully-developed liquid film using equation 2.12

$$l_s = \frac{(g\rho\delta^2/2\mu + U_{TB})^2}{2g}. \quad 2.12$$

After this simplification, the type of the wake is dependent only on *N*. According to them, there are three different flow patterns in the wake of a Taylor bubble:

Type I Closed axisymmetric wake: $N < 500$

A laminar wake of liquid was observed rising up at the velocity of the bubble as in Figure 2-1(a). The wake had a toroidal vortex located just behind the tail of the bubble. The wake length increases with *N* and they suggested the following relationship to estimate the wake length:

$$\frac{l_w}{D} = 0.30 + 1.22 \times 10^{-3} N. \quad 2.13$$

The wake length is defined as the vertical distance between the lower surface of the bubble and the lower stagnation point in the wake.

Type II Closed unaxisymmetric wake: $500 < N < 1500$

In this case, the vortex ring still exists but the wake starts to oscillate as in Figure 2-1(b) and the wake is transitional. The size of the wake also increases with *N* but no expression relating these two parameters was given.

Type III Open wake with recirculating flow: $N > 1500$

The wake can be described as turbulent with obvious recirculation as in Figure 2-1(c). However, these authors concluded that the extent of mixing was similar for all Taylor bubble lengths that they studied.

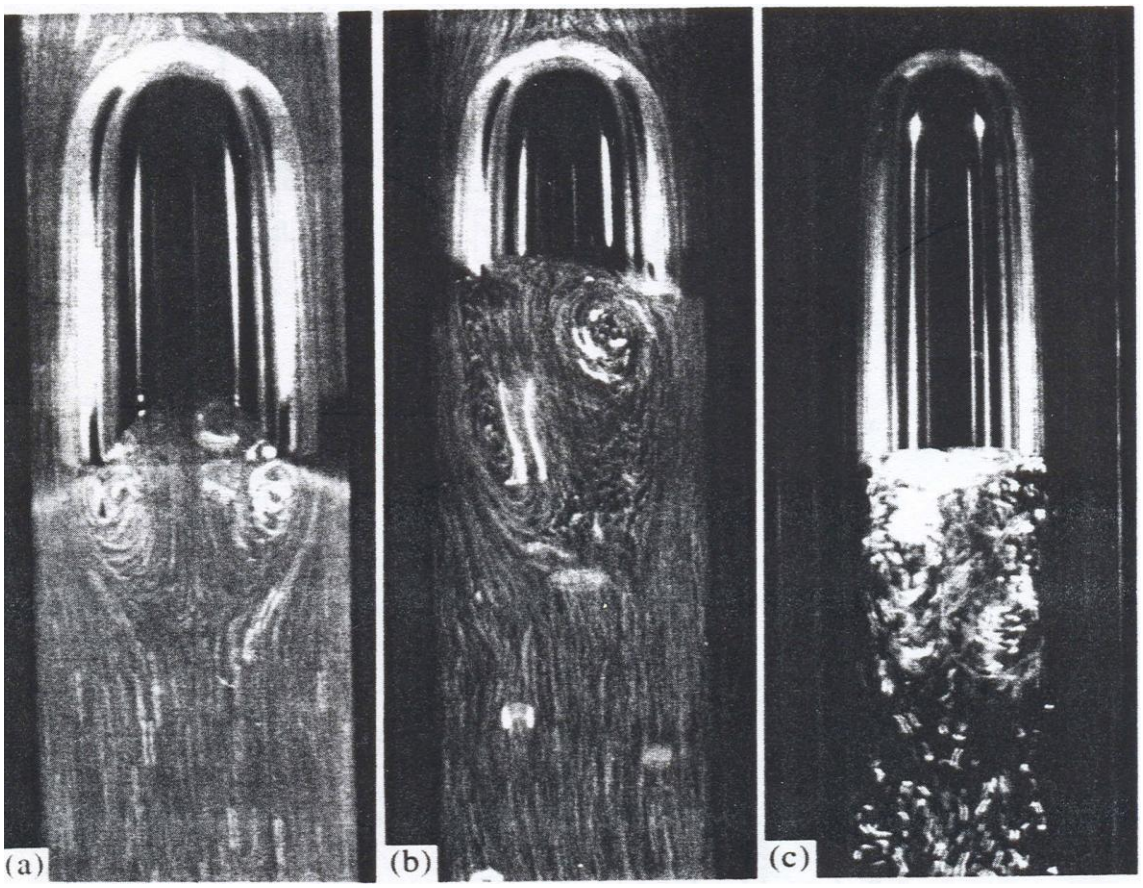

Figure 2-1: The wake patterns of Taylor bubble rising in a stagnant liquid. (Campos and Geudes de Caravlho, 1988)

Mao and Dukler (1991) experimentally and numerically studied the motion of Taylor bubbles rising through stagnant liquids. Their experimental results suggest that Taylor bubbles create a developing free film around themselves which can require a large distance to become fully-developed. This means that the film continues to accelerate for long distances behind the top of the bubble. Their computational results showed that for low viscosity and surface tension, the terminal velocity is independent of the liquid properties. On the other hand, the film thickness and the wall shear stress are strongly effected by the viscosity. The film thickness increases with increasing viscosity.

DeJesus *et al.* (1995) made detailed velocity field measurements around Taylor bubbles rising in stagnant kerosene in a vertical 25.4mm diameter tube ($Eo = 194$ and $M = 2.9\times10^{-9}$) using a photochromic dye activation technique with a digital high-speed video camera and image analysis. The measurement showed the general features of the flow in the nose and film regions. Near the nose, the flow changes direction and starts to accelerate downward. In the film, the velocity profile is a fully-developed laminar falling film. Their measurements in the wake region seem rather unclear. This may be due to the high mixing in the wake and to limitations of their camera framing rate.

Pinto and Campos (1996) conducted experiments to study the interaction between two bubbles rising in stagnant liquids of different viscosities. The tube sizes were 19, 32, and 52 mm. The minimum stable distance for no interaction between the two bubbles was measured. Values of the velocity and the distance between bubbles were obtained from pressure transducer signals. They related N to the minimum distance $l_{\min}$ that should separate two successive bubbles for no influence to occur and they developed the following expressions:

1. For laminar flow in the wake, $l_{\min}/D$ changes linearly with N.

$$\frac{l_{\min}}{D} = 1.46 + 4.75\times10^{-3} N \qquad \text{for } 100 < N < 500 \qquad 2.14$$

2. For transition flow in the wake, $l_{\min}/D$ still changes linearly with N but according to

$$\frac{l_{\min}}{D} = 0.692 + 7.9\times10^{-3} N \qquad \text{for } 500 < N < 1500 \qquad 2.15$$

3. For turbulent flow in the wake, $\frac{l_{\min}}{D}$ is constant.

$$\frac{l_{\min}}{D} = 12.5 \qquad \text{for } N > 1500 \qquad 2.16$$

They reported that the near wake (they called it also part one of the minimum stable length) occupies 24% of the stable liquid slug length regardless of the flow pattern of the wake. They fitted a correlation to their data and related the trailing and leading velocity to the distance between them. However, the transient nature of the motion of the bubble in the wake raises a question about the accuracy of the trailing bubbles velocity measurements.

Tomiyama *et al*. (1996) carried out a systematic investigation to examine the effect of *E*o and M on the shape of Taylor bubbles. In their experiments, *E*o was varied by changing the diameter of the tube (*D* = 5.4, 10.2 and 15.1 mm) and M was varied by adjusting the sucrose concentration of the fluid. The experiments covered a range of $0 < Fr \leq 0.35$. All the flows examined were laminar and the maximum Reynolds number was 87.3. Their observations can be summarised as follows:

(1) The trailing edge of the bubble is flattened by increasing *E*o or decreasing *M*.

(2) The liquid film thickness increases with increasing *M*.

(3) For high viscosity, the oblateness of the trailing edge increases with decreasing *E*o.

(4) The wave disturbance at the tail of the bubble affects the bubble tail shape. This disturbance appears when *E*o is low.

(5) The bubble nose bluntness increases with decreasing *M* under a constant *E*o.

In general, the findings from their work was consistent with others. The difference is that their work was presented in terms of *E*o and *M*. They also developed a numerical model to predict the terminal velocity of the bubble, the forces acting on the bubble, and the velocity

distribution in both phases. Their conclusion was that their model agreed with the available experimental data.

Bugg *et al.* (1998) developed a numerical model of the flow around Taylor bubbles rising in stagnant liquids using a volume-of-fluid method. The range of their study was $10 \leq Eo \leq 100$ and $10^{-12} \leq M \leq 10^{1}$. Their observation was that the rounded leading edge exists for all conditions. The trailing edge may be characterized by Froude number rather than by whether the flow regime is inertia-dominated or viscosity-dominated. A flat bottom was observed for all cases with $Fr>0.3$. The equilibrium in the film was achieved for all cases with $N \leq 100$. The terminal velocity prediction was within 10% of the experimental data of White and Beardmore (1962). The model also predicted the velocity field around the bubble. In the film, the velocity increases with the axial position and the thickness of the film decreases. A recirculation zone exists in the wake.

Aladjem Talvy *et al.* (2000) studied the interaction between two consecutive Taylor bubbles rising in stagnant water in a vertical tube. The tube was 25 mm in diameter and 4 m long. The experiments were performed for different ranges of liquid slug lengths. The interaction was measured by recording video sequences (illumination by 500 W halogen lamps) of the flow field of the trailing bubble. They reported increasing oscillation of the trailing bubble as the trailing bubble approaches the leading bubble and that interaction between the bubbles exists even at distances larger than 16*D*.

Polonsky *et al*. (1999a) studied the movement of Taylor bubbles in a vertical 25 mm diameter tube filled with water. The movement was recorded at different axial locations along the tube by two interlaced video cameras. The illumination was done either by laser light sheet or 500 W halogen lamps. They reported that the frequency of the bubble bottom oscillations is nearly constant but the amplitude increases strongly with bubble length and liquid velocity.

The velocity field above a Taylor bubble rising in stagnant and co-current flowing water was measured by Polonsky *et al.* (1999b) using PIV. However, they were not able to achieve measurements in the film and the wake due to the limitations imposed on the minimum time between frames.

Bugg and Saad (2002) carried out an experiment to measure the velocity field around a single Taylor bubble rising in stagnant olive oil in a 19 mm vertical tube (N = 90, E_O = 100 and M = 0.015). The velocity field was measured near the nose, in the film, and in the wake of the bubble using PIV. The measurements showed the expected behavior of the liquid around the bubble. There is a strong radial velocity at the nose of the Taylor bubble. Near the nose, the axial velocity is approximately equal to the terminal velocity of the bubble. From the nose, the liquid film accelerates downward as the radial profile of the axial velocity becomes characteristic of a freely falling film. Surprisingly, the falling film is decelerated substantially before entering the wake. This is most likely due to the rounded edge of the bubble tail. The effect of the wake in the falling film starts to be felt about 2 mm above the tail. The liquid film penetrates into the wake region creating a recirculation zone just underneath the bubble.

The wake was determined to be laminar and axisymmetric. These measurements were used to validate the model by Bugg *et al.* (1998). The model was generally in good agreement with the experimental results.

van Hout *et al.* (2002a) also performed PIV measurements around a single Taylor bubble rising in stagnant water. The tube size was 25 mm and the wake flow pattern was turbulent. The effect of the bubble was felt about 0.5*D* ahead of the bubble nose. They observed a distinct vortex up to 2*D* behind the bubble and a secondary, much weaker vortex, between 2*D* and 5*D*. The averaged velocities become negligible about 12*D* behind the bubble tail. However, the instantaneous velocity effects are felt even at 50*D* behind the bubble.

Taha and Cui (2006) numerically investigated the motion of single Taylor bubbles in stagnant and flowing liquids using the volume-of-fluid method. FLUENT was used for this numerical study. They claimed that their model compared favorably with the published experimental results in predicating the bubble shape and rise velocity, velocity distribution and wall shear stress.

Kang *et al.* (2010) investigated the behavior of a Taylor bubble rising in stagnant liquids using a front tracking technique coupled with the finite difference method. They studied the effects of density ratio (25 to 100), viscosity ratio (10 to 100), Eötvös number (*E*o) (120-300) and Archimedes number $(N)^2$ (1×10^2 to 2×10^5) on the dynamics of rising Taylor bubbles. They concluded that the dynamics of Taylor bubbles did not depend on the density ratio or the viscosity. However, Eötvös number and Archimedes number influenced the bubble

bottom shape and the wake structure. Their model was not able to successfully simulate large density ratios (1000).

Araújo *et al*. (2012) reported a numerical study based on volume-of-fluid technique and ANSYS FLUENT for a single Taylor bubble rising in stagnant liquid. The range of parameters that the simulation covers was wide ($4.72\times10^{-5} \leq M \leq 104$ and $6 \leq Eo \leq 900$). Under these conditions, the wake of the Taylor bubble was laminar. The numerical model calculates the rise velocity of a Taylor bubble, the velocity field around the nose, in the film and in the wake. They also provide a map that predicts the existence of wake structure and the concavity of the bubble bottom surface based on knowing M and Eo. They validate the model with their experimental results.

Most recently, Araújo *et al*. (2013) extended their numerical model to study the interaction between two consecutive the Taylor bubbles rising in stagnant liquids ($4.72\times10^{-5} \leq M \leq 104$, $15 \leq Eo \leq 575$, laminar wakes). The model estimated the rise velocity, nose shape, falling film and wake of the trailing bubble as it approaches the leading bubble. They presented the velocity ratio between the leading and trailing bubble for various flow conditions. The model showed that the nose of the trailing bubble first tends to sharpen and then it begins to flatten as it moves close to the bottom of the leading bubble. Also, the model showed that the falling film thickness, average velocity of the falling film, and the wake size for the trailing bubble increase as the trailing bubble approaches the leading one.

Most recently, Liu *et al*. (2013) experimentally investigated the wake structure of a single Taylor bubble rising in tubes with five different diameters (3, 5, 8, 14, and 16 mm) at various inclination angles (30º, 45º, 60º and 90º) in stagnant liquid nitrogen using PIV. Based on the ray tracing method, they developed an algorithm to correct for the optical distortion due to tube curvature and index of refraction difference between the liquid and the tube material. They obtained the velocity field in the wake. They found that the vortex size behind the bubble increases with decreasing inclination angle. Also, they noticed that the Campos's criterion (based on *N*) for classifying the wake of Taylor bubble rising in stagnant liquid is not applicable for liquid nitrogen two-phase flow. This may be due to the small tube sizes used which may affect the forces acting on the bubble.

Several researchers have studied this flow by placing a solid object in the shape of a Taylor bubble inside a tube. Tudose and Kawaji (1999) studied the total drag force acting on a fixed solid model of a Taylor bubble in a downward flowing liquid. One of their important findings is that using a solid model of Taylor bubble did not have a major effect on the structure of the wake.

Vassalow & Kumar (1997) used PIV to measure the velocity field in the wake region of a solid simulated Taylor bubble in a duct. Their measurements showed the recirculation zone behind the bubble. They suggested that the wake region decreases in size somewhat as Reynolds number increases even though their conclusion was based on testing just two different Reynolds numbers. However, there are some drawbacks to their measurements:

(1) The obstruction was not centred exactly in the duct.

(2) The solid obstruction is not dynamically equivalent to a bubble since the duct walls are fixed relative to the simulated bubble and the stress free boundary condition at the gas-liquid interface is not satisfied.

Velocity measurements in the wakes of confined axisymmetric bluff bodies in tubes are also reported in the literature. Taylor and Whitelaw (1984) studied the effects of the blockage ratio of the bluff body on the structure of the wake using Laser Doppler Velocimertry (LDV). They found that the near-wake length and the maximum centreline velocity increase with increasing blockage ratio. Sotiriadis and Thorpe (2005) used LDV to investigate the wake of cylindrical bluff bodies and ventilated cavities attached to a central sparger in turbulent flow. They suggest that the bluff body provides a convenient experimental substitute for studying a ventilated cavity. Also, they confirmed that the size of vortex in the near wake does not change with increasing liquid flow rate.

2.2 Taylor Bubbles in Moving Liquids

Griffith & Wallis (1961) modified equation 2.4 to account for the effect of the liquid velocity when the bubble rises in a flowing liquid. They suggested the following equation:

$$U_{\mathrm{TB}} = 0.35 c_1 \sqrt{gD} \qquad 2.17$$

They related c_1 by plotting it as a function of Reynolds number based on the liquid velocity and the Reynolds number based on the bubble velocity.

Nicklin *et al*. (1962) studied slug flow in vertical tubes. They suggested a more logical equation for the bubble rise velocity

$$U_{\mathrm{TB}} = C U_{\mathrm{m}} + 0.35\sqrt{gD}, \qquad 2.18$$

where the constant C takes the value of 1.2 when the liquid flow regime is turbulent and 2 when it is laminar. It represents how much faster the liquid at the tube centre moves compared to the mean velocity. U_{m} is the mixture velocity and $U_{\mathrm{m}} = U_{\mathrm{L}} + U_{\mathrm{G}}$ where U_{L} is the liquid superficial velocity and U_{G} is the gas superficial velocity.

Pinto *et al.* (1998) conducted an experimental investigation of the influence of the liquid flow on the coalescence of two Taylor bubbles rising in co-current flow for different tube sizes. The wake flow pattern in these investigations was turbulent and the liquid flow regimes were laminar and turbulent (Reynolds number based on the superficial velocity of the liquid). They used differential pressure transducers to measure the velocity and minimum stable slug length. They defined three different flow patterns in the wake based on the Reynolds number of the liquid relative to the bubble $Re_R = (U_{\mathrm{TB}} - U_{\mathrm{L}})\rho D/\mu$.

I. Laminar wake when $Re_{\mathrm{R}} < 175$
II. Transitional wake when $175 < Re_{\mathrm{R}} < 525$
III. Turbulent wake when $Re_{\mathrm{R}} > 525$

They concluded that when the liquid flow is turbulent the minimum liquid slug stable length is about 5D. For the laminar regime, coalescence occurs when the ratio between the average velocity in the fully-developed film and the liquid superficial velocity is greater than 25 and the minimum stable length is 10D. When this ratio is lower than 25 and the initial distance between the bubbles is longer than the wake length there will be no coalescence.

van Hout *et al.* (2002a) investigated the translation velocity of Taylor bubbles rising in stagnant and flowing water for various flow rates, pipe orientations, and pipe diameters (24 and 54 mm). They used optical fiber probes and image processing to measure the velocities. They concluded that the translation velocity predicted by equation 2.18 agreed well with the

experimental results. On the other hand, for a 54 mm tube the prediction was only good for a slightly inclined pipe and for the other angles the difference was very large between the predicted velocities and the measured ones.

Shemer *et al.* (2005) studied the wake of Taylor bubbles rising in upward moving liquids in a 26 mm tube using PIV. They investigated the mean and instantaneous velocity field for two liquid flow rates corresponding to laminar (Re_L = 820) and turbulent (Re_L = 7500) flow. The vortex rings behind the bubble existed for both flow rates. This similarity was due to the fact that the wake was turbulent regardless of the liquid flow regime. These toroidal vortex rings were not observed in the instantaneous velocity field. In both cases the velocity profile remained undeveloped even at very large distances behind the bubbles. The velocity profile approached the fully developed shape in the turbulent case much faster than in the laminar case.

Nogueira *et al.* (2006a) performed PIV measurements around single Taylor bubbles rising in stagnant and co-current flow in vertical 32 mm tubes. They combined the PIV measurements with a pulsed shadowgraphy technique to measure the bubble shape. This study was performed using water and glycerol solutions to produce a wide range of viscosities. The regions studied were the nose and the film. Their observations were that the bubble shapes at the nose closely agreed with the potential flow theory as the viscosity of the liquid decreased, the fully-developed film thickness is constant and the film transition from laminar to turbulent occurs around Re_f =80 ($Re_f = U_f \rho \delta / \mu$). They also obtained the mean velocity profile in the liquid film by averaging 60 instantaneous profiles along the fully-developed

film. Shear stress was calculated throughout the film based on these velocity profiles. These measurements showed a decrease of shear stress as the liquid viscosity decreases.

This work was extended by Nogueira *et al.* (2006b) to study the flow in the wake and near-wake regions of a Taylor bubble rising in stagnant and upward flowing liquid. They studied; laminar, transitional and turbulent wakes. The experiments were carried out in a 32 mm vertical tube for different liquids ($15 < N < 18{,}000$). However, the background liquid flow rates were quite small and yielded very low Reynolds numbers (Re_L = 11 to 214). They showed the mean and instantaneous velocity for different type of wakes. They also obtained the wake length and the minimum stable length of the liquid slugs from the velocity measurements.

This work was extended by Shemer *et al.* (2007) to include three different tube sizes at different flow rates (Re_L= 700 to 43,000). Their findings were consistent with their previous work. The near wake behind the bubbles (up to a distance of 4*D*) was similar for all cases regardless of the background flow regime. For the laminar background flow, the fully-developed flow velocity profile was not achieved even at distances of 70*D* while for turbulent flow re-development was achieved at around 25*D*. In all cases, the cores of the vortices are located at 0.5*D* to 0.7*D* from the bubble bottom and at 0.25*D* to 0.35*D* from the tube centerline.

Mayor *et al.* (2007) performed an experimental and simulation study on Taylor bubbles in vertical tubes with a laminar liquid background flow. In upward laminar flow, they found that the bubble-to-bubble interaction is strong for liquid slugs shorter than 2*D*. It is weaker

for longer slugs. They proposed a correlation for relating the trailing bubble velocity to the length of the liquid slug behind the leading one. Their simulation of bubble-to-bubble interaction was developed based on their proposed experimental correlation.

Mayor *et al*. (2009) extended their previous experimental work studying bubble-to-bubble interaction for Taylor bubbles rising in laminar upward flowing water to turbulent upward flowing water. They proposed a correlation that relates the trailing bubble velocity to the length of the preceeding liquid slug. The correlation is independent of the tube diameter, superficial velocities and the velocity and length of the leading bubble. They found that bubble-to-bubble interaction was found only for separating distance between bubbles shorter than 8-10*D*.

Lu and Prosperetti (2009) used a finite volume method to simulate Taylor bubbles rising in a vertical tube filled with stagnant, upward and downward flowing liquids. They illustrate in their model the effect of both Morton number and Eötvös number in bubble dynamics. They validated their model against the detailed measurements of Bugg and Saad (2002).

A numerical study of the effects of the co-current (upward and downward flows) on a rising Taylor bubble was performed by Quan (2011). In this study, the inverse viscosity number is $16 < N < 291$ and the velocity ratio ($U_L/U_{TB\ stagnant}$) between the liquid velocity and the bubble velocity in stagnant liquid is in the range of $-0.52 < U_L/U_{TB\ stagnant} < 0.36$. The bubbles tend to be elongated by the upward flow and shortened by the downward flow. Also, the upward flow elongates the skirted tail and makes it oscillate.

Li *et al*. (2013) presented a detailed numerical simulation of a single argon Taylor bubble rising in a vertical tube in liquid LBE (Lead-Bismuth Eutectic is used as a coolant in some nuclear reactors). Several simulations were performed for bubbles rising in stagnant and moving liquid (Eo = 118, $M = 9.53\times10^{-13}$, $U_L = 0 \sim 0.75\sqrt{gD}$). Their results included the rise velocity of the bubbles, velocity profiles around the nose, in the falling film and in the wake. They claim that their results agree well with other researchers numerical and experimental results.

Slug flow regime in microchannels has been investigated experimentally and numerically by various researchers. Channels are generally considered small when surface tension forces dominate gravitational forces (measured by Eo). Since this thesis focuses on Taylor bubbles rising in large tubes (inertia-controlled regime), the slug flow in a microchannels is out of the scope of this literature review. A good review article on Taylor bubbles in microchannels is reported by Angeli and Gavriilidis (2007).

2.3 Summary

A summary of experimental and theoretical studies for Taylor bubbles rising in vertical tubes is presented in Table 2-1. The velocity field ahead of a Taylor bubble has an effect on the shape and the velocity field around the bubble. The leading bubble's wake affects the shape and the velocity of the trailing bubble. Therefore, studying the velocity field in the liquid phase is essential to understanding the complicated nature of slug flow. The literature contains several different techniques to measure the velocity field in the liquid phase around Taylor bubbles. These works provide valuable insight into the characteristics of slug flow but

suffer from some shortcomings. Some experimental studies address only small ranges of superficial liquid velocities (e.g., Nogueira *et al.*, 2006(b), Re_L= 0 ~ 250; wake flow pattern: laminar, transitional and turbulent) whereas others cover narrow ranges of liquid properties (e.g. Shemer *et al.*, 2005 and 2007, water, Re_L = 700 ~ 43,000; wake flow pattern: turbulent). To the author's knowledge, these are the only two sets of PIV measurements in the wake of Taylor bubbles rising in upward flowing liquid. In this thesis, the bubble shape and the velocity field in the liquid phase is reported around rising Taylor bubbles in stagnant and moving liquids in a vertical tube using digital image processing and PIV techniques for all possible flow regimes in the liquid (laminar and turbulent) and in the wake (laminar, transitional and turbulent). The experiments were carried out in a 25 mm tube for a wide range of liquid viscosities (μ=0.00100, 0.00500 and 0.0430 Pa·s) and Reynolds numbers (Re_L = 250 to 17,800). The velocity measurements will be used to interpret the behaviour of Taylor bubbles. For example, the mechanism of the Taylor bubble coalescence depends heavily upon the velocity field in the wake of the bubbles. This work is an extension of the work done by Saad (1999). The knowledge gained from this work can also be used to validate numerical models.

Table 2-1: Summary of experimental and theoretical studies for Taylor bubbles rising in vertical tubes

References	**Methodology**	**Stagnant/ flowing liquid**	**Number of bubbles**	**Flow parameters**	**Techniques**
Davies and Taylor, 1950	Theoretical	stagnant	one		Using potential flow theory found $U_{\mathrm{TB}} = 0.328\sqrt{gD}$
White and Beardmore (1962)	Experimental	stagnant	one	$3 < Eo < 400$ $10^{-12} < M < 10^{3}$	Measured rise velocity of the bubble
Moissis & Griffith (1962)	Experimental	plastic model		Water in 25 mm diameter tube	Pitot tube
Goldsmith and Mason (1962)	Experimental Theoretical	stagnant	one	$Re_{\mathrm{TB}} = 10^{-5}$ to 1.0 $\left(\frac{U_{TB}\rho}{\sigma}\right)$=2×10^{-4} to 2×10^{-2}	Photography
Brown (1965)	Theoretical	stagnant	one		Potential flow theory
Zukoski (1966)	Experimental	stagnant	one	Different liquids (water, glycerin, mercury, ethyl alcohol)in different tube sizes (5 mm to178 mm) and inclinations	Measured rise velocity of the bubble
Campos and Guedes deCarvalho (1988)	Experimental	stagnant	one	Range of liquid properties at different tube diameters (19 - 25 mm)	Photography
Mao and Duckler (1991)	Experimental Theoretical	stagnant and flowing	one	Water in 50.8 mm tube	Conductance wires and shear stress probe

References	Methodology	Stagnant/ flowing liquid	Number of bubbles	Flow parameters	Techniques
DeJesus *et al.* (1995)	Experimental	stagnant	one	Kerosene in a 25 mm tube	Photochromic dye activation technique
Pinto and Campos (1996)	Experimental	stagnant	two	19, 32, and 52 mm tube, water and glycerol mixture ($140<N<37000$)	Pressure transducers
Tomiyama *et al.* (1996)	Experimental Theoretical	stagnant	one	5.4, 10.2 and 15.1 mm tube, sucrose and water mixtures	Photography
Bugg *et al.* (1998)	Numerical	stagnant	one	$10 < E_o < 100$ and $10^{-12} < M < 10^{1}$	Volume-of-fluid method
Aladjem *et al.* (1999)	Experimental	stagnant	two	Water in 25 mm tube	Photography
Polonsky *et al.* (1999a)	Experimental	stagnant	one	Water in 25 mm tube	Photography

References	Methodology	Stagnant/ flowing liquid	Number of bubbles	Flow parameters	Techniques
Polonsky *et al*. (1999b)	Experimental	stagnant & flowing	one	Water in 25 mm tube	PIV
Saad and Bugg (2002)	Experimental Numerical	stagnant	one	olive oil in a 19 mm tube (N = 90, E_o = 100 and M =0.015)	PIV and volume-of-fluid method
van Hout *et al.* (2002a) a	Experimental	stagnant	one	Water in 25 mm tube	PIV
Taha and Cui (2006)	Numerical	stagnant and flowing	one		Volume-of-fluid method
Kang *et al.* (2010)	Numerical	stagnant	one	1×10^2 <Archimedes number< $2\times10^{5,}$ $120<E_o<300$, density ratio (25 to 100), and viscosity ratio (10 to 100)	Front tracking coupled with finite difference method
Vassalow and Kumar (1997)	Experimental	plastic model		Downward flowing water two different Reynolds number	PIV

References	Methodology	Stagnant/ flowing liquid	Number of bubbles	Flow parameters	Techniques
Tudose and Kawaji (1999)	Experimental	plastic model		Downward flowing water	Drag force measurement
Griffith and Wallis (1961)	Experimental	flowing & stagnant	one	Water in 12.5, 17 and 25 mm tube	Measured rise velocities
Pinto *et al.* (1998)	Experimental	flowing	two	22, 32, and 52 mm tube, water and glycerol mixture ($2{,}400 < N < 18{,}000$)	Pressure transducers
van Hout *et al.* (2002b)	Experimental	flowing	continuous	Water in 24 and 54 mm tubes	Optical fiber probes
Shemer *et al.* (2005)	Experimental	flowing	one	Water in 25 mm tube, Re_L = 820 and 7,500	PIV
Nogueira *et al.* (2006a, 2006b)	Experimental	stagnant and flowing	one	Water and glycerol solution in 32 mm tube, $15 < N < 18000$, Re_L = 11 to 214	PIV

References	Methodology	Stagnant/ flowing liquid	Number of bubbles	Flow parameters	Techniques
Shemer *et al*. (2007)	Experimental	flowing	one	Water in14, 25, 54 mm tubes, Re_L = 700 to 43,000	PIV
Mayor *et al.* (2007, 2009)	Experimental Theoretical	flowing	continuous	Water in 32, 52 mm tubes (laminar and turbulent flows in background liquid)	Image analysis technique and a slug flow simulation code
Lu and Prosperetti (2009)	Numerical	stagnant and flowing	one		Volume-of-fluid method
Quan (2011)	Numerical	flowing	one	$16 < N < 291$ $-0.52 < U_L / U_{TBstagnant} < 0.36$	Front tracking coupled with finite difference method
Araújo *et al*. (2012)	Numerical	stagnant	one	$4.72\times10^{-5} \leq M \leq 104$ and $6 \leq Eo \leq 900$	Volume-of-fluid and ANSYS FLUENT
Araújo *et al*. (2013)	Numerical	stagnant	two	$4.72\times10^{-5} \leq M \leq 104$ and $15 \leq Eo \leq 575$	Volume-of-fluid and ANSYS FLUENT

References	Methodology	Stagnant/ flowing liquid	Number of bubbles	Flow parameters	Techniques
Li *et al*. (2013)	Numerical	flowing and stagnant	one	liquid LBE $Eo = 118$, $M = 9.53\times10^{-13}$, $U_L = 0 \sim 0.75\sqrt{gD}$	
Liu *et al*. (2013)	Experimental	stagnant	one	Nitrogen in 3, 5, 8, 14, and 16 mm tubes at various inclination angles (30º, 45º, 60º and 90º)	PIV

3 Experimental Apparatus and Instrumentation

The experiment described in this thesis is designed to provide instantaneous two-dimensional velocity field measurements around Taylor bubbles rising in a vertical tube containing a stagnant or moving liquid. To achieve this objective, the main experimental tasks are:

- to design and construct an apparatus to create Taylor bubbles,
- to select a pumping system which is able to deliver different liquids (range of viscosities) at the desired flow rates,
- to develop a triggering system that enables PIV data acquisition at different locations around the Taylor bubbles,
- to process the raw image data to locate the bubble surface at the nose and the bottom of the bubble, and
- to improve data averaging in the wake by shifting the velocity fields based on the location of the bubble bottom surfaces in the image.

The following sections explain the experimental apparatus, the image processing procedure used to measure bubble shape and the PIV system.

3.1 Apparatus

A schematic diagram of the apparatus is shown in Figure 3-1. The liquids were mixtures of filtered tap water and glycerol. The viscosity of the mixture was measured using Brookfield Digital Viscometer model DV-II. The Taylor bubbles contained air. The liquid flows in a

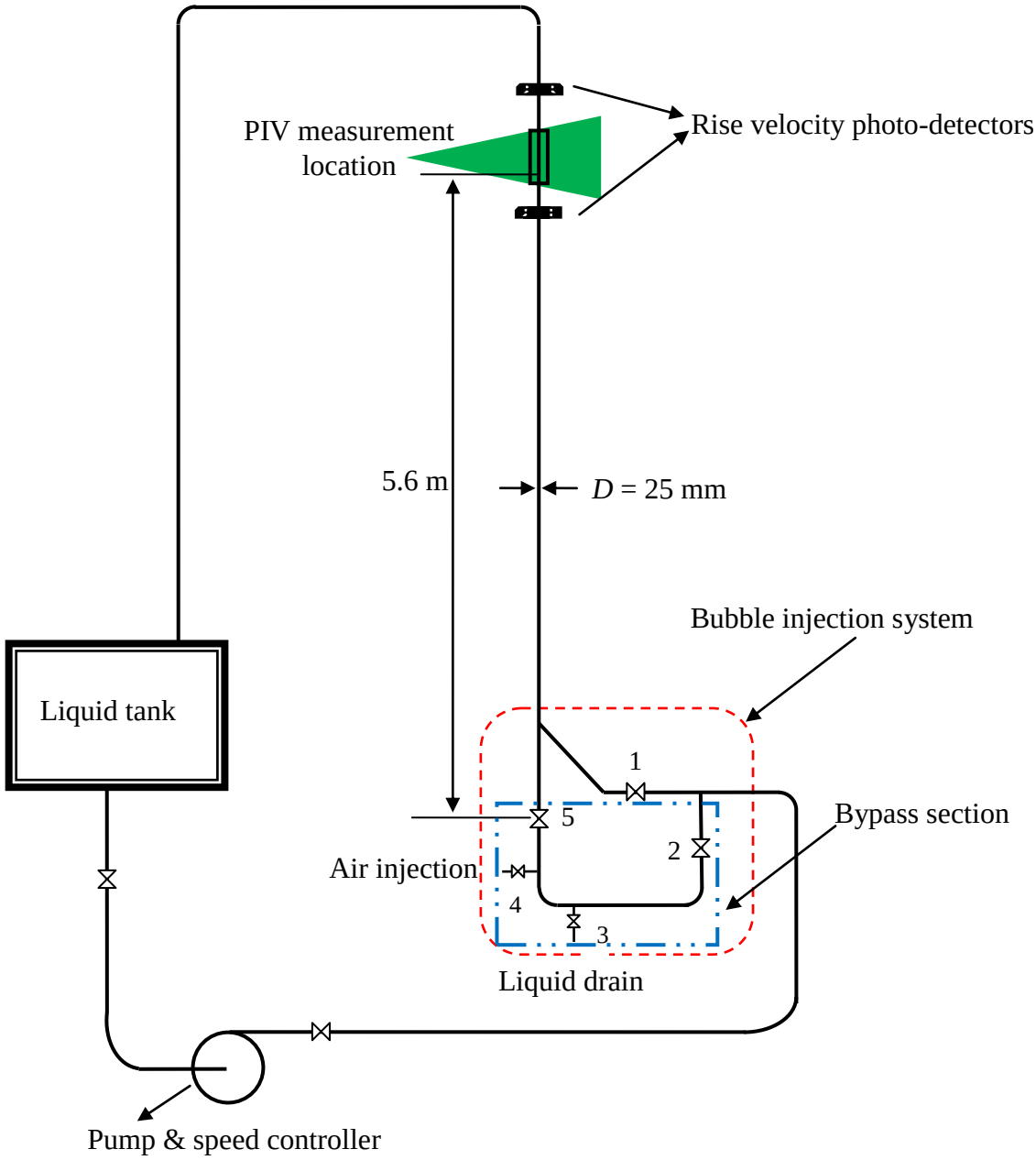

Figure 3-1: Schematic diagram of the apparatus used to create isolated Taylor bubbles in an upward-flowing liquid.

close loop driven by a Goulds vertical multi-stage centrifugal pump (ITT G and L series SSV) controlled by a Toshiba H3 variable-speed drive. The experiments were conducted in a 7.8 m long vertical acrylic tube. The tube inside diameter was 25.31 mm. The distance from the bubble release valve (5) to the test location (the development length) was 5.6 m. A large storage tank was filled with liquid. The tank was equipped with a filtering system consisting of a small centrifugal pump and two filters (range from 1 to 30 μm). A thermocouple was placed in the tank to monitor the temperature during the experiment. The injection of the bubbles, the detection of the bubbles, the triggering system, and the PIV system are discussed later in this chapter.

3.1.1 Creating Taylor Bubbles

In order to make good PIV measurements, it was necessary to produce Taylor bubbles with clear wakes (free of small bubbles). To produce an ideal Taylor bubble, other workers have tried several methods such as rotating air-filled hemispherical cups (Davies Taylor, 1950, Campos and Guedes de Carvalho, 1988). DeJesus (1995) used a "flexible developing section consisting of a horizontal section followed by a long sweeping gradually inclined bend". Shemer *et al.* (2005) used an inlet section which consisted of "a large settling chamber, a honeycomb, a number of screens and a converging nozzle". The air was introduced through a pipe placed in the middle of the inlet section. The air was injected manually after its volume was measured carefully. The size of the injected bubbles was 3~3.5*D*.

In this work, a very simple apparatus was used. The Taylor bubbles were produced in the lower part of a vertical 25 mm diameter tube. The bypass section was essential to produce

Taylor bubbles with wakes that were free of small bubbles especially for the flowing liquid cases. The injection system consists of an injection valve (4), drainage valve (3), a bubble release valve (5), and a bypass valve (2). It is illustrated in Figure 3-1. The following steps were performed to produce a single Taylor bubble:

Stagnant liquid

1. Open valves 1, 2, and 5 to fill the test section with liquid from a tank.
2. Close valves 1, 2, and 5.
3. Open valve 3 and inject the desired volume of air through valve 4 using a syringe.
4. Close valves 3 and 4. At this stage the volume of air will be trapped below the closed ball valve 5.
5. Open valve 5 quickly to release a single Taylor bubble.

In flowing liquid

1. Open valves 1, 2 and 5 to let the liquid flow in the loop.
2. Close valves 2 and 5.
3. Open 3 and inject the desired volume of air through valve 4 using a syringe.
4. Close valves 3 and 4. At this stage the volume of air will be trapped below the closed ball valve 5.
5. Open valves 5 and 2 quickly at the same time to release a single Taylor bubble in the flowing liquid.

3.1.2 Phase Transition Detectors

The vertical tube was equipped with two phase-transition detectors designed to detect the presence of Taylor bubbles in the liquid. Each detector consists of an infrared diode and an

infrared detector. The diode and the detector are perpendicular to the wall of the tube. A plastic base was used to hold the detector and the diode properly aligned. When the tube is full of liquid the infrared diode produces a continuous signal to the detector. The signal is interrupted when a bubble passes between the diode and the detector (see Figure 3-1). The signal from the lower phase detector is used to trigger the PIV measurements. Two such phase detectors were used to measure the rise velocity of the Taylor bubbles by placing them a known distance apart and measuring the time for the bubble to travel between them using a digital oscilloscope.

3.1.3 Optical Correction Box

In general, optical distortion affects all optical measurement techniques. In this work, one source of optical distortion is the curvature of the tube wall. To minimize the optical distortion induced by the curvature of the tube wall, a rectangular box filled with liquid was attached to the tube at the measurement location (Goldsmith and Mason, 1962). The box was designed so that it could be moved vertically along the tube. The base of the optical correction box was made from two acrylic blocks. The blocks were machined to fit around the tube and an O-ring was used to seal the gap between two acrylic pieces and to hold the box from sliding down the tube. The walls of the box were made of thin sheets of acrylic. The optical correction box was filled with pure glycerol. The index of refraction of the acrylic is 1.49. The index of refraction of water and pure glycerol are 1.33 and 1.47, respectively.

3.2 Particle Image Velocimetry

3.2.1 Introduction

In fluid mechanics research, the velocity field supplies valuable information required to understand the flow structure. Particle Image Velocimetry (PIV) is a full-field velocity measurement technique which makes non-intrusive velocity measurements at thousands of points simultaneously. For this reason, it is well-suited to studying spatial variations in the velocity field. A PIV system consists of a two-dimensional light sheet to illuminate the flow field, seeding particles in the flow to scatter the light, an image recording device to record the position of the particles, and a system for analyzing the image to determine the particle motion. In its classical form, the illumination is pulsed twice and the resulting pairs of particle images are recorded by a camera. Knowing the time between the illumination pulses, the instantaneous velocity can be estimated from the measured particle displacement. The fluid velocity is inferred from the motion of the seed particles. Details of the illumination, seeding process, image recording and analysis are discussed in the following sections.

3.2.2 Flow Seeding Considerations

It is important that the seeding particles have the ability to follow the flow and scatter sufficient light to be recorded by the camera. The choice of the seed particle diameter is a compromise between reducing the particle size to improve flow tracking and increasing the particle size to improve light scattering. Considering these requirements, the fluorescent particles used to seed the flow were PMMA Rhodamine B-Particles. These particles emit light with a wavelength of 584 nm and have a density of 1.51 gm/cm^3. A filter was placed on

the camera lens to attenuate reflected laser light (532 nm) from the bubble interface and the tube walls and allow only the particles images to be recorded on the camera's CCD.

One measure of the particle's ability to track a flow effectively is its terminal velocity. Assuming a spherical particle and a creeping flow, the terminal velocity (U_t) is given by Clift *et al*. (1978) as

$$U_t = g d_p^2 \frac{(\rho_p - \rho)}{18\mu} \quad 3.1$$

where g is the acceleration due to gravity, d_p is the particle diameter, ρ_p is the particle density, ρ is the fluid density and μ is the fluid dynamic viscosity. The fluorescent particles have a density of 1.51 gm/cm^3 and diameter of 1-20 μm. This yields a terminal velocity of the particle (10 μm) of 2.12×10^{-5} m/sec. Since this velocity is extremely small, there is confidence that the particle tracks the flow well.

Another important measure is by the following criterion (Clift *et al*., 1978):

$$St \ll \frac{2\chi+1}{9}. \quad 3.2$$

Here χ is the ratio of the particle density to the fluid density and *St* is the Stokes number which is defined as the ratio of the particle lag time to an appropriate fluid timescale ($St = \tau_s/\tau_f$). According to Raffel *et al.* (2007) the lag time is given by

$$\tau_S = d_{\mathrm{p}}^2 \frac{\rho_{\mathrm{p}}}{18\mu}. \qquad 3.3$$

This equation yields a value of τ_S =3.3×10^{-5} s.

An estimate of the fluid timescale can be obtained from

$$\tau_f = \frac{D}{U_{\mathrm{TB}}}, \qquad 3.4$$

where D is the tube diameter (0.025 m) and is used as the length scale. U_{TB} is the Taylor bubble rise velocity and is used as the velocity scale (range from 0.174 to 1.02 m/s). To ensure that the particles follow the flow, the largest Stokes number must be much smaller than 0.44 as suggested by equation 3.2. From equation 3.3, the particle time lag is 3.3×10^{-5} s. The velocity scale is 0.174 m/s and the length scale is 0.025 m. Therefore, the fluid timescale given by equation 3.4 is 0.145 s which yields a value of *St* of about 2.27×10^{-4}. This is very small compare to 0.44 (from equation 3.2) suggesting that the particles track the flow very well and do not affect the accuracy of the PIV measurements.

The spatial resolution of the velocity information that is obtained from PIV depends in part upon the number of particles per unit volume of the fluid. Each interrogation area must have a minimum number of particles (typically about 10 to 20) to make a successful velocity measurement. The particle concentration should be large enough to enable small interrogation areas that can resolve the thin falling film region of the Taylor bubble. Seeding the liquid properly is not difficult. In this experiment, the seeding process required two steps. The first step was to prepare a high-concentration stock by mixing a known weight of the seeding particles in a known volume of the test liquid. The second step was to estimate the

required amount of the high-concentration stock required and add it to the test liquid. The actual mass of seed particles required to seed the entire loop is too small to measure so making a high concentration stock is essential to seed the liquid. Another advantage of making this stock is to make sure that the powder is well mixed in the fluid. It is also very convenient to use the stock to increase the seeding density when there is not enough seed in the loop. The seeding occurs in the liquid tank before the test section is filled.

3.2.3 Light Sheet

The requirements of the illumination system are as follows:

- the illumination pulse duration must be short to avoid image blur caused by motion of the seed particles during the exposure time,
- the separation time between the two illumination pulses must be such that the particles travel a maximum of approximately 1/4 to 1/3 the length of the integration area between illumination pulses, and
- the illumination level must be high enough to provide sufficient intensity that individual particles can be detected.

The above requirements were achieved using a New Wave Research Inc. MiniLaseIII dual Nd:YAG laser. It provides very short duration (6 ns) pulses with 50 mJ/pulse at a wavelength of 532 nm. This laser is specially designed for PIV work. Since the repetition rate achievable with a single laser of this type is only 15 Hz, two identical lasers, which share beam delivery optics, are used. In this way the time between the two illumination pulses can be made arbitrarily short. A Berkeley Nucleonics Inc. 505 digital pulse/delay generator was used to trigger the two lasers and could be programmed to give any desired pulse separation.

The illumination must take the form of a thin sheet of light in the image recording device's field of view. To generate the light sheet, the laser beam passes through a spherical lens and a cylindrical lens. The spherical lens controls the light sheet thickness while the cylindrical lens controls the light sheet height (see Figure 3-2). The thickness of the light sheet is an important parameter. It needs to be thin enough to provide good spatial resolution and should be compatible to the depth of the field of the recording optics. The thinnest portion of the light sheet is located at the focal length of the spherical lens. In this work, the focal length of the lenses was 1000 mm for the spherical lens and -12.7 mm for the cylindrical lens. This gives a light sheet thickness of 1 mm.

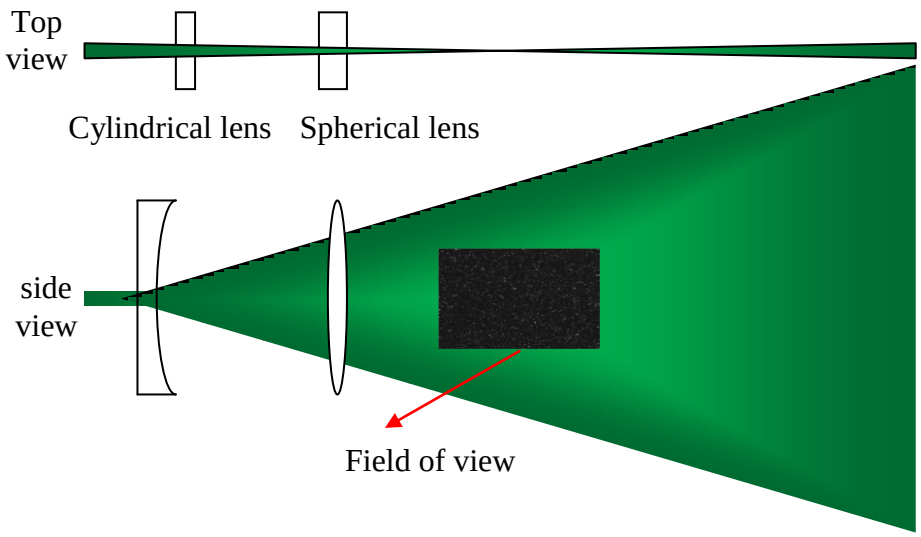

Figure 3-2: Light sheet generation using a spherical lens and a cylindrical lens

3.2.4 Image Capture

The illuminated plane was recorded using a Redlake MegaPlus ES4020 camera with 2048×2048 active pixels. The camera was fitted with an AF Micro-Nikkor 60 mm lens. A

filter was placed on the camera lens to block reflected laser light from the bubble interface and the tube walls and allow only the particles images to be recorded on the camera's CCD.

An important parameter, which can affect the quality of the particle images, is the focusing of the recording lens. The depth of field of the recording lens is the range of object distances for which acceptable focus is achieved on the recording plane. Since the depth of field was small and the light sheet was thin, accurate focusing was critical to achieving quality images. The camera was manually focused on the particles in the light sheet. This focusing was done with the room dark using a focus mode in the software PIVAcquire (developed in house). For focusing, the laser was set on a low energy level and 30 Hz frequency to minimize danger of eye damage from the laser. The camera lens was focused manually by turning the focus ring on the lens while checking the sharpness of the particle images on the computer screen. To make sure that good particle image focusing was achieved, several test images were taken with the laser at high energy and the image quality was checked.

Image calibration is important to convert the displacement data from camera coordinates (in pixels) to actual distance in the flow field. Since it would be very difficult to insert a calibration target in the measurement location, the tube outer diameter was used as the calibration target. A picture of the acrylic tube viewed through the optical correction box can be seen in Figure 3-3. To make the tube outside diameter very clear, it was illuminated with the laser light sheet and the room lights. Due to index of refraction mismatch between tube material and water, the inside wall of the tube was impossible to locate. Using Matrox Inspector® software, the picture was enhanced and the pixel positions for the wall outside edges were located manually. This, combined with the known outer diameter of the tube

(31.84 mm), was used to determine the calibration factor. It was found to be 22.727 μm/pixel. To check the accuracy of the calibration, the calibration factor was compared to one which was calculated from the bubble rise velocity using the two phase transition detector and the bubble rise velocity using PIV system. This calibration factor has been found to be very consistent. The difference was around 1.1%.

To obtain a velocity field measurement at the desired position relative to the bubble (nose, wake), the signal from the lower phase detector (when the nose of the bubble triggered it) was used to trigger a Berkeley Nucleonics 500B digital pulse/delay generator. The components of the PIV triggering system are shown in Figure 3-4. This delay generator waits for a programmed delay period before it initiates a trigger signal to the pulse generator which synchronizes the camera and the laser. A timing diagram for the PIV system is illustrated in Figure 3-5. The delay time is a function of the Taylor bubble velocity and the desired measurement location relative to the bubble. Each laser pulse is captured by the camera on a different frame and the resulting image (2048 x 4096) contains a pair of frames (each size 2048 x 2048). After triggering by the delay generator, a series of images was acquired. For each flow condition, an effort was made to capture part of the bubble's bottom surface in the field of view to use as a reference point when measuring locations for the velocity field in the wake.

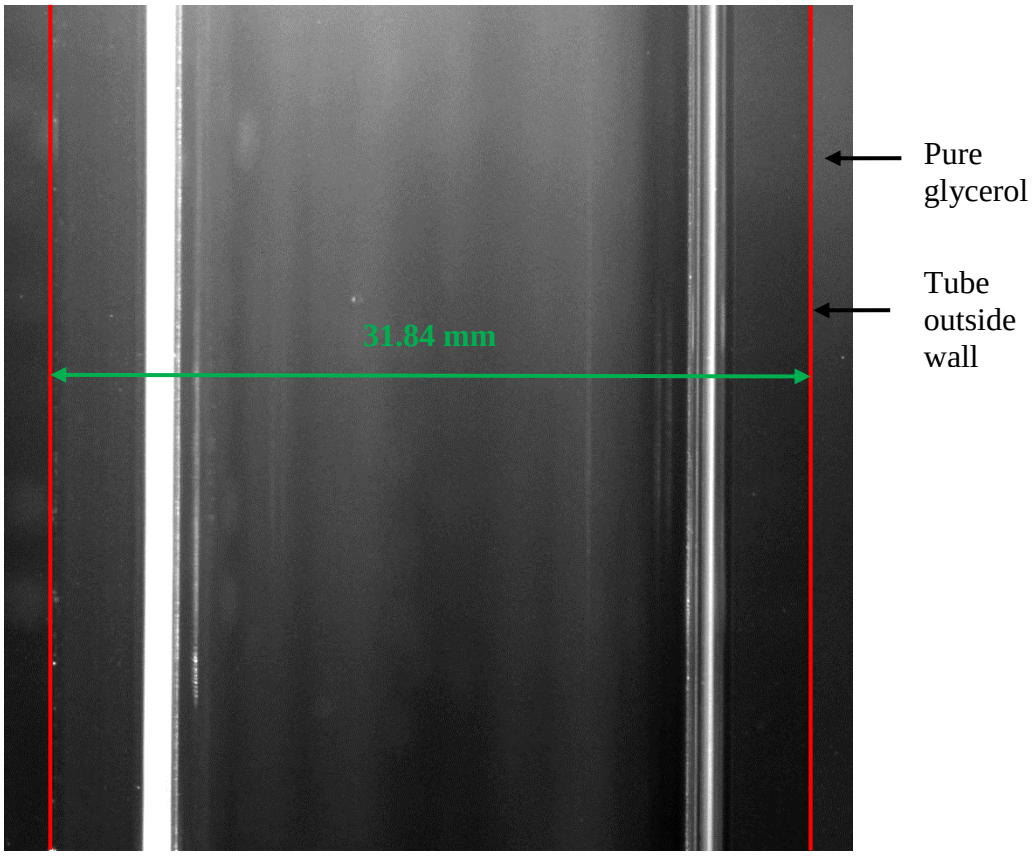

Figure 3-3: A picture of the acrylic tube at the test section

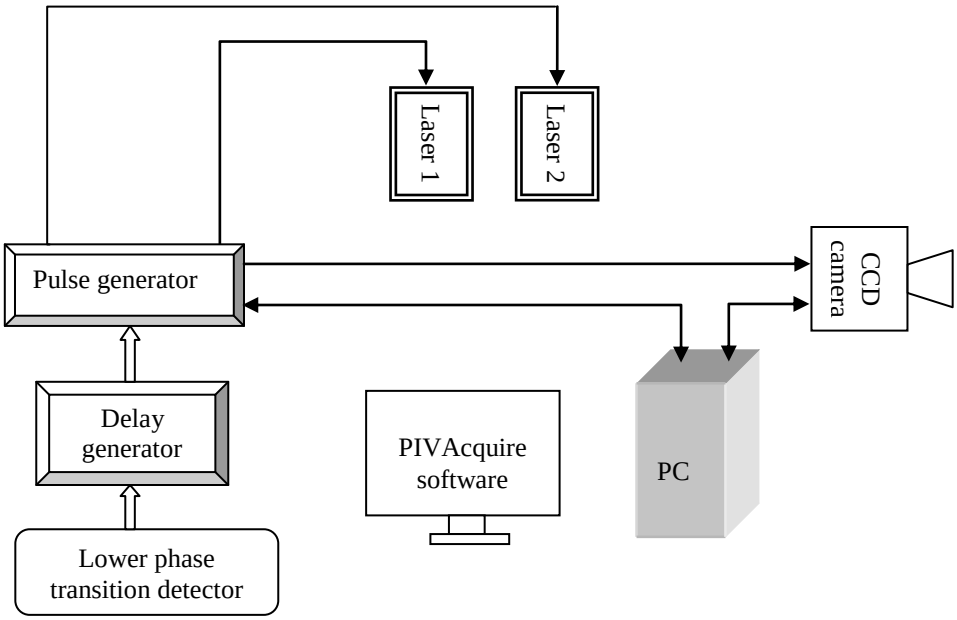

Figure 3-4: The PIV system and triggering components

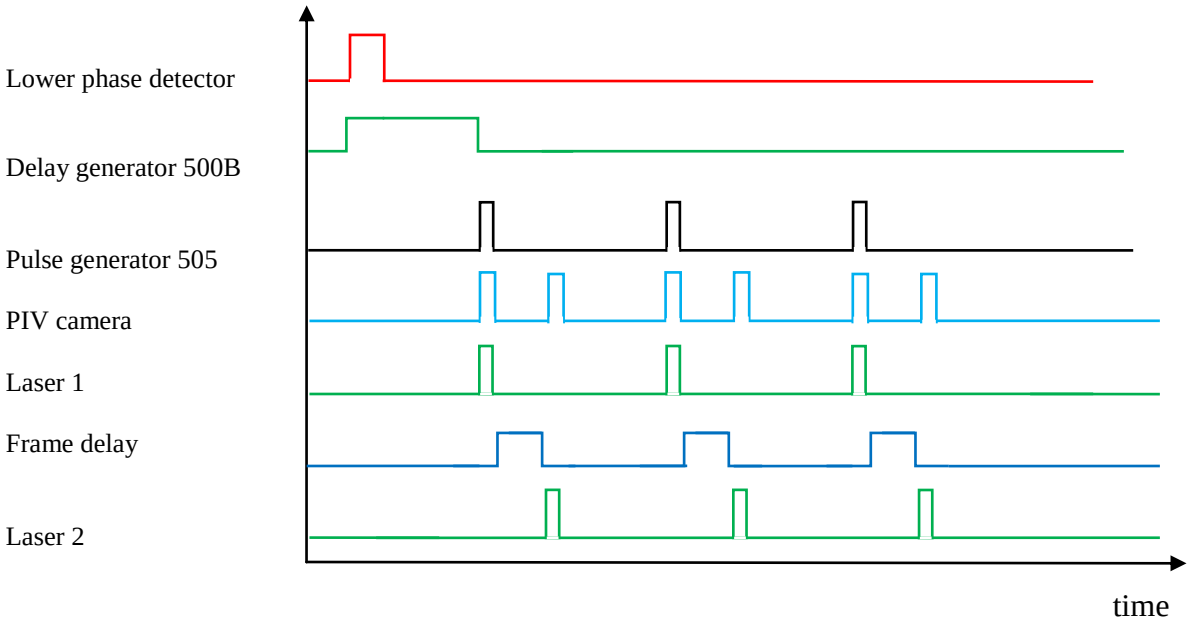

Figure 3-5: The timing diagram of the PIV system

For the flowing liquid cases, the bubble velocities were so fast that it was impossible to take a single sequence of images that covered the entire region behind the bubble (due to the low framing rate of the PIV system). To overcome this problem, three or four sequences were taken with appropriate delays to cover the entire wake. This strategy is illustrated in Figure 3-6. The delay was selected to have overlap regions between frames.

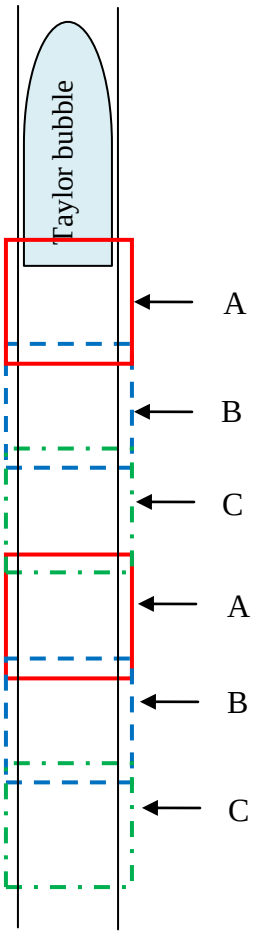

Figure 3-6: Three sequences of images (A, B and C) that cover the entire region behind the bubble.

3.2.5 PIV Image Analysis

Figure 3-7 illustrates the steps of PIV image analysis. In-house software was used to process the PIV images. PIV images are subdivided into small (typically 64×64 pixel) regions called interrogation areas. The mean particle displacement is determined statistically for each interrogation area by means of correlation techniques. This process involves calculating the cross-correlation function and then searching the correlation function for the appropriate displacement peak. In the following sections some specific PIV image analysis steps are discussed.

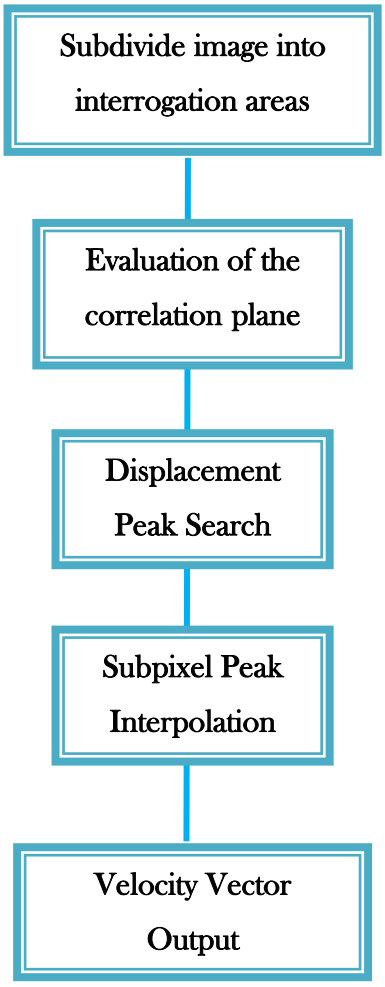

Figure 3-7: Stages involved in PIV image analysis

The Cross-correlation Technique

When two separate frames contain particle images from the respective light pulses (dual-frame PIV) it is possible to use cross-correlation techniques. The cross-correlation function is described by Adrian (1991) as

$$C(\bar{S}) = \iint I_1(\bar{x})\, I_2(\bar{x} + \bar{S})\mathrm{d}A, \qquad 3.5$$

where $C(\bar{s})$ is the cross-correlation function and $I_1(\vec{x})$ and $I_2(\vec{x})$ are two interrogation area images extracted from separate frames. Essentially, the cross-correlation function measures the similarity between the two images for a given displacement. Figure 3-8 presents a typical cross-correlation function. The highest peak in the correlation plane is the average particle image displacement. The calculation of the cross-correlation function can be done directly or by Fast-Fourier Transform algorithms (FFTs). In this thesis, the half-padded FFT integration technique was used to compute the spatial correlation. This technique may be summarized as follows. An interrogation area (IA) from the first image is padded with zeros to become twice its original size. The size of the second IA is selected to be twice of the original size of the first IA. Then the zero-padded IA from the 1st image is correlated with the 2nd IA from the 2nd image. The padding does not affect the spatial resolution. One of the advantages of this method is a good signal-to-noise ratio. The displacement of the highest correlation peak from the origin gives the mean displacement of the particles in the IA. The cross-correlation analysis produces an average displacement vector of all particles within the interrogation area (Adrian, 1991).

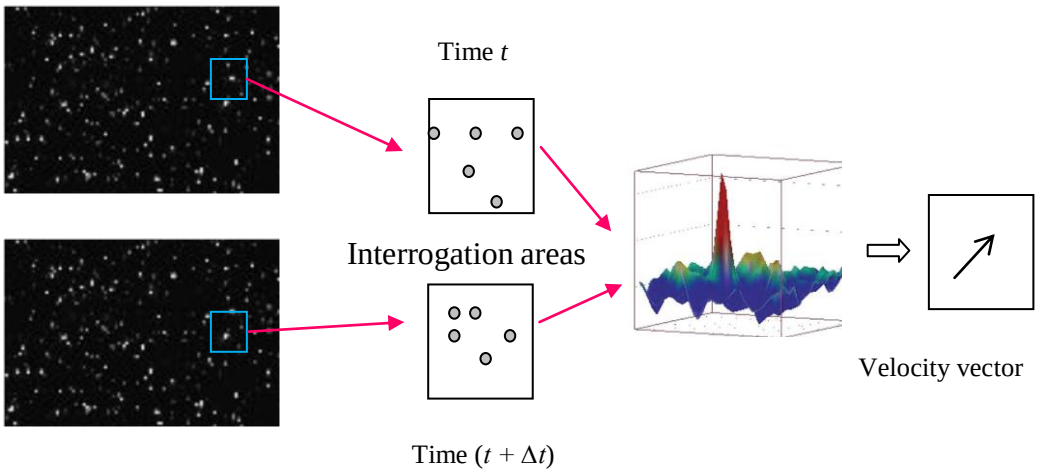

Figure 3-8: PIV analysis using the cross-correlation technique

Peak Finding

An important step in PIV analysis is to detect and locate the correlation peak. Since the correlation function is calculated at discrete locations, a simple search for all local maxima finds all peaks on the correlation plane. After all peaks are found, they are ranked by their height and the signal peak is assumed to be the highest peak. Because of the discrete nature of the correlation data, this process locates the displacement peak with an uncertainty of $\pm \frac{1}{2}$ pixel. To increase the accuracy, it is necessary to locate the correlation peak with sub-pixel accuracy. Estimation accuracies of the order of 0.05 - 0.1 pixel are achievable for 32x32 interrogation areas (Raffel *et al.*, 2007). There are many methods to accomplish this, such as centre of mass calculations, parabolic curve fitting and Gaussian curve-fitting methods (Bugg and Rezkallah, 1998). However, all of these methods amount to the fitting of a continuous function to the discrete correlation data in the neighborhood of the signal peak and locating

the maximum in this function to yield a peak location with sub-pixel accuracy. In this thesis, the Gaussian curve-fitting method was implemented for locating the correlation peak to sub-pixel accuracy.

Post Processing

The post-processing software was developed in house. The main task of this software is to identify the spurious velocity vectors which result from a bad correlation and then replace them with valid vectors based on information from neighboring good vectors. The outlier vectors are either very different from their neighbors or outside the physically possible velocity range. They are the results of interrogation areas that contain either insufficient particle images or have low single-to-noise ratio. The first step in the post processing is to identify these outlier vectors. This step was done using a cellular neural network (CNN) method (Shinneeb *et al*., 2004). After identifying and removing outliers from the data, the next step is to replace the outliers with Gaussian-weighted averages of neighboring good vectors. During post processing, the data were also converted to engineering units and the coordinates were transformed from camera coordinates to global coordinates using the calibration images.

3.2.6 Uncertainty Analysis in PIV

One of the challenges of PIV is to determine the measurement uncertainty. This uncertainty is generally a function of the experimental conditions and the particle displacement algorithms used (Huang *et al*., 1997). Significant improvements in the measurement uncertainty and reliability of PIV have continued over the last decades (Adrian, 2005). The velocity measured by PIV is calculated from

$$V = \alpha \frac{\Delta X}{\Delta T} \tag{3.6}$$

where α is the calibration factor, ΔX is the displacement, and ΔT is the separation time between the two laser pulses.

The uncertainty is calculated using the techniques outlined in ASME PTC 19.1-2005. The general form of the expression for determining the uncertainty of a measurement is the root-sum-square of the systematic and random standard uncertainties of the results. Equation 3.7 is used to calculate the combined standard uncertainty of the results,

$$u_{\mathrm{V}} = [(b_{\mathrm{V}})^2 + (s_{\mathrm{V}})^2]^{1/2}, \tag{3.7}$$

where

b_V is the systematic standard uncertainty in the velocity, and

s_V is the random standard uncertainty in the velocity.

The expanded uncertainty$(U_{V,95})$ in the results at approximately 95% confidence is given by

$$U_{V,95\%} = 2u_V \tag{3.8}$$

The absolute systematic standard uncertainty b_V in equation 3.7 may be determined from the uncertainties in α, ΔX, and ΔT using the propagation equation 3.9.

$$b_{\mathrm{V}} = \left(\left[\frac{\partial V}{\partial \Delta X} b_{\Delta \mathrm{X}} \right]^2 + \left[\frac{\partial V}{\partial \Delta T} b_{\Delta \mathrm{T}} \right]^2 + \left[\frac{\partial V}{\partial \alpha} b_{\alpha} \right]^2 \right)^{1/2}. \tag{3.9}$$

Similarily, the absolute random standard uncertainty in the velocity s_V may be determined from equation 3.10.

$$s_{\mathrm{V}} = \left(\left[\frac{\partial V}{\partial \Delta X} s_{\Delta \mathrm{X}} \right]^2 + \left[\frac{\partial V}{\partial \Delta T} s_{\Delta \mathrm{T}} \right]^2 + \left[\frac{\partial V}{\partial \alpha} s_{\alpha} \right]^2 \right)^{1/2}. \tag{3.10}$$

The calibration factor was calculated using:

$$\alpha = \frac{D_{\mathrm{m}}}{D_{\mathrm{pixel}}}, \tag{3.11}$$

where D_{m} tube diameter in meters measured using digital calipers and D_{pixel} tube diameter measured in pixels from the PIV images.

The outside tube diameter (31.84 mm) was measured 10 times using digital calipers and the random uncertainty was calculated from the standard deviation of the measurements. The digital caliper resolution is ±0.02 mm (the systemic uncertainty is 0.01 mm). Matrox Inspector® software was used to locate the outside walls of the tube. The error of locating the wall was estimated to be ±4 pixel. The tube outside diameter is 1407 pixel. An estimate of the uncertainty in α gives the following values:

$$b_{\alpha} = 3.29 \times 10^{-8} \frac{\mathrm{m}}{\mathrm{pixel}};$$

$$s_{\alpha} = 4.91 \times 10^{-8}\ \mathrm{m/pixel}.$$

The temporal resolution of the pulse generator used to control the laser pulses is 10 ns. This gives an uncertainty in ΔT of

$$b_{\Delta T} = 3.88 \times 10^{-5}\ s.$$

The PIV measurements of ΔX contain uncertainties that arise from several sources. These errors are influenced by many factors. Some of them are the noise in the recorded images, the size of the seeding particle image, the mis-match of paired particles images, the laser power fluctuation, and seeding density (Bugg and Rezkallah; 1998, Westerweel *et al*., 1997). The effect of velocity gradients, the inability of the seeding particle to follow the flow without slip, and integration area size were studied by Keane and Adrian (1990). Prasad *et al*. (1992) showed that the particle image diameter strongly influences the accuracy of the measured

velocities. Empirical estimates for the optimal particle image diameter range from 2 to 4 pixels (Adrian and Westerweel, 2011). One of the most often reported errors in PIV is the error originating from the peak-locking phenomenon (Lourenco and Krothapalli, 1995; Westerweel *et al.*, 1997). Peak-locking errors are due to the process of computing the signal peak location to sub-pixel accuracy. A variety of techniques have been reported in the literature to improve the sub- pixel accuracy of the displacement (Hart 2000, Westerweel *et al.* 1997).

From the above discussion, it is clear that the uncertainty in the PIV data is a function of many factors. This makes the task of uncertainty assessment difficult because the exact values are not known. For this reason, the uncertainty was estimated in this work by making conservative assumptions of the uncertainty based on the literature. Huang *et al.* (1997) stated that the random errors range from 0.03 to 0.1 pixels and a conservative random error which rises from the correlation algorithm estimate can be assumed to be 0.1 pixels. For the optimal particle image diameter (2-4 pixels), the bias error in the estimation of the particle image displacement has a value of around 0.05-0.1 pixel (Overmars *et al*., 2010). In this uncertainty estimate, a conservative estimate of the bias error is taken to be 0.1 pixels even though histogram of the displacement for the data obtained in this thesis showed very little evidence of peak-locking effects. As an example, the values of the absolute uncertainty estimate for the velocity at the centreline of the tube for a laminar flow case are presented in Table 3-1. This conservative estimate of the uncertainty leads to a relative uncertainty of 4% for the velocity.

An analysis was done to identify the largest contributor to the overall uncertainly. This analysis shows that the random errors and systematic errors in the displacement are the dominate contributors (99%) to the overall uncertainty in the velocity measurement. Since the displacement is the main contributor to the uncertainty, it was important to compare the uncertainty in the displacement in this estimate to those in the literature. The uncertainty in displacement for this study is 0.284 pixels. Shinneeb's (2006) uncertainty value is 0.29 pixels. Shinneeb's (2006) analysis was based on simulated images with a known pixel displacement and comparing that displacement to the one obtained through PIV image analysis.

Table 3-1: Summary of uncertainty in data results:

Calibration factor α (m/pixel)	**Pulse separation time** ΔT (s)	**Velocity Calculated value** V (m/s)	**Absolute systematic standard uncertainty** b_V (m/s)	**Absolute random standard uncertainty** s_V (m/s)	**Combined Standard uncertainty of the result** u_V (m/s)	**Expanded uncertainty of the result** $U_{V,95}$ (m/s)
0.00002272	0.0002	0.777	0.01142	0.01154	0.01624	0.0325

3.3 Taylor Bubble Shape

The bubble shape was measured using image processing techniques on the images acquired by the PIV system. Shape measurements are important during the PIV image analysis especially around the nose region. The measurements were used as a digital mask during the PIV analysis to better resolve the flow close to the bubble interface. The processing of the PIV images to obtain shape is described in this section.

3.3.1 Preliminary Processing

Digital image processing was used to measure the location of the gas-liquid interface. Matrox Inspector® is a hardware-independent application designed for image capture, storage, and processing applications. The following digital image processing operations are performed on the PIV images using Matrox Inspector®:

- ***Median filter***: This is to eliminate some of the noise created by the seeding particles in the background.
- ***Opening and closing***: This is done to remove large seed particle images from the image
- ***Threshold***: Thresholding remaps pixels in an image to a new range of values. The most common thresholding operation is binarizing which maps all pixels below a certain value to zero and all those above to the maximum value. It is used to identify the bubble.
- ***Erosion***: Removes layers from objects, peeling extraneous pixels and removing small particles from the image. Inspector®'s predefined erosion operation replaces each pixel with the minimum value (if operating on bright objects) in its 3×3 neighborhood or with the maximum value (if operating in dark objects).
- ***Edge detection***: In general, edges can be distinguished by a sharp change in intensity between two adjacent pixels. Inspector® provides a number of edge detection operations. The prewitt operation was used to detect the bubble interface in this work.

- ***Thinning***: The thinning operation peels layers from an object. This operation is similar to the erosion operation except, if it is continuously, iterated it will not convert the entire image to the background intensity.

After these operations were performed some noise still remains inside and outside of the bubble. This noise needed to be filled manually. Figure 3-9 illustrates the image processing steps. Removing the noise is essential for correctly extracting the position of the interface.

3.3.2 Bubble Shape Measurements

Once the preliminary processing is performed, the bubble shape measurements are extracted by markers on the gas-liquid interface using Inspector®'s edge detection features. Inspector® can find a predominate edge with sub-pixel accuracy in a given image based on certain specific characteristics.

The process of positioning the markers on the interface begins by specifying a search box. The search box controls the area to be searched. The orientation of the search box ensures the proper search direction and box must include a portion of the edge. The edge must enter and leave by opposite sides of the search box. For this work, the search box was 1 pixel high and the search direction was 270^{o} for the right side and 90^{o} for the left side of the bubble.

Inspector®'s scripting feature automated all of these operations. The scripts were recorded by performing operations manually with Inspector®'s recorder activated. These scripts were edited to add looping and comments. The interface position measurements were written to a text file.

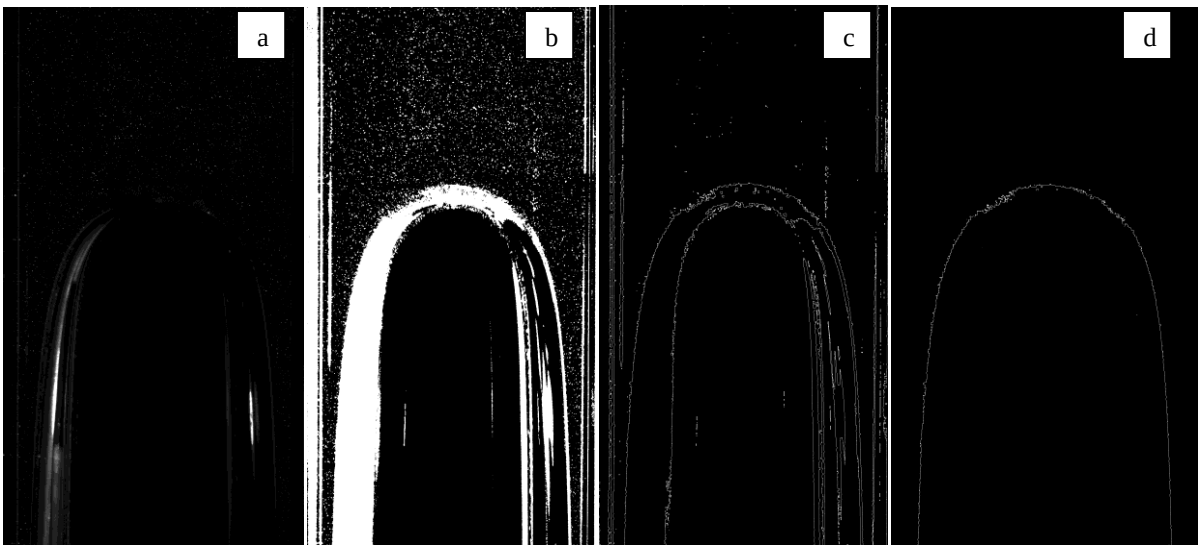

Figure 3-9: Sequence of image processing operations used to determine Taylor bubble shape (a) Median filter process, closing and opening operations (b) Threshold process (c) Erosion, edge detection and thinning processes (d) Contours of the bubble

3.4 Run Matrix

To achieve the objectives of this work, the experimental parameters shown in Table 3-2 are selected to cover wide ranges of operating conditions (fluid properties and liquid flow rates) and for all possible flow regimes (in the background liquids and in the near wake bubble region). The wake classifications are based on the work of Campos and Guedues de Carvalho (1988) for stagnant cases and Pinto *et al*. (1998) for flowing cases.

In Table 3-2, N is a dimensionless inverse viscosity number (equation 2.11), Re_L is Reynolds number based on superficial liquid velocity, Re_R is Reynolds number based on the relative velocity, Re_{TB} is Reynolds number based on the Taylor bubble velocity, U_L is the mean

superficial liquid velocity, U_{TB} is the Taylor bubble rise velocity, μ is the liquid dynamic viscosity and ρ is the liquid density.

Table 3-2: List of experimental parameters for Taylor bubble velocity field measurements

Glycerol weight (%)	**μ (N.s/m^2)**	**ρ (kg/m^3)**	***N*** **(-)**	U_L **(m/s)**	Re_L **(-)**	U_{TB} **(m/s)**	Re_{TB} **(-)**	Re_R **(-)**	**Wake pattern**
77	0.0430	1,200	352	0	0	0.174	120	120	laminar
				0.377	260	0.878	620	360	transition
45	0.00500	1,120	2,850	0	0	0.174	1,000	1,000	turbulent
				0.253	1,500	0.661	3,800	2,300	turbulent
				0.684	3,900	0.979	5,700	1,800	turbulent
0	0.00100	1,000	12,600	0	0	0.173	4,400	4,400	turbulent
				0.362	9,200	0.613	15,400	6,200	turbulent
				0.541	13,600	0.820	20,700	7,100	turbulent
				0.706	17,800	1.020	25,800	8,000	turbulent

3.5 Experimental Procedure

The experimental apparatus and the PIV system just described were used to produce Taylor bubbles and measure their terminal velocity, bubble shape, and the liquid velocity field around them. Figure 3-1 shows the overall experimental apparatus. The first step in the experimental procedure was to seed the fluid with the appropriate amount of the seed particles, start the pump, adjust the pump speed and measure the flow rate. With the room dark, the laser sheet was aligned to include the axis of the tube. The camera was manually focused on the particles in the light sheet. Next, the desired volume of air was injected (see Section 3.1.1) and the bubble rose in the stagnant liquid or flowing liquid. Then, the images

were captured as described in Section 3.2.4. This concluded an experimental run. This was repeated many times (80 ~ 800) depending upon the conditions.

3.6 The Mass Balance

In order to check the validity of the PIV velocity measurements, a mass balance on the liquid was performed. Figure 3-10 illustrates the control volume used to check the mass balance. The control volume in this figure is moving with the bubble. Conservation of mass for a control volume is given by

$$\frac{\mathrm{d}}{\mathrm{d}t}\iiint \rho \mathrm{d}\forall + \iint \rho \overrightarrow{V}.\hat{\mathrm{n}}\mathrm{d}A = 0 \qquad 3.12$$

where ρ is the liquid density, $\vec{V}$ is the liquid velocity, and $\hat{n}$ is a unit normal vector on the control surface facing outwards. Since the control volume moves at the same speed as the bubble, the flow is steady and equation 3.12 can be written as

$$\iint \rho \overrightarrow{V}.\hat{n}\mathrm{d}A = 0. \qquad 3.13$$

Therefore, the mass flow into the control volume ahead of the bubble must be balanced by the mass flow out of the bottom of the control volume. The top of the control volume is placed well ahead of the bubble where a uniform velocity of U_{TB} (in the stagnant case) exists. The bottom of the control volume can be placed at any axial location in order to perform a mass balance check on the velocity measurements at that location.

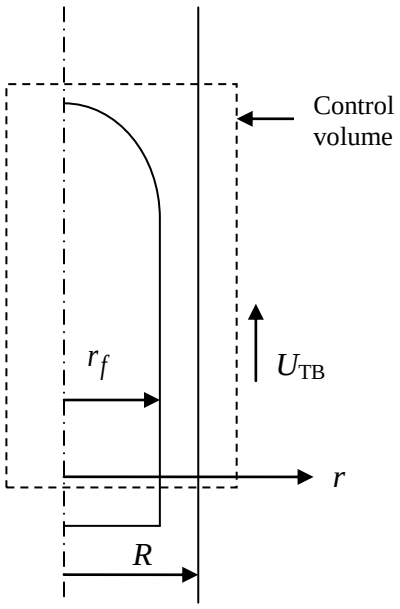

Figure 3-10: Sketch of the control volume used to check the mass balance around a rising Taylor bubble

The mass balance around the bubble then becomes

$$\rho U_{\mathrm{TB}} \pi R^2 - \int_{r_f}^{R} 2\pi\rho(V_{\mathrm{z}} - U_{\mathrm{TB}}) r \mathrm{d}r = 0, \qquad 3.14$$

or

$$U_{\mathrm{TB}} = -\frac{1}{R^2}\int_{r_f}^{R} 2(V_{\mathrm{z}} - U_{\mathrm{TB}}) r \mathrm{d}r. \qquad 3.15$$

where V_{z} is the axial velocity determined from the PIV measurements.

To overcome the lack of measurements close to the wall, a curve (polynomial 2nd order equation) was fitted to the near-wall region based on the available data and the assumption that the walls move downward with a velocity equal to the terminal velocity of the bubble (no slip condition). The validity of the radial profiles of axial velocity (V_{Z}) for the PIV measurements can be checked by comparing the value of U_{TB} given by equation 3.15 to the value from the phase transition detectors. When considering axial locations ahead of the bubble, the rise velocity calculated from equation 3.15 was within 1% of the velocity

measured with the phase transition detectors. For profiles in the falling film near the nose, it was within 4%. The difference becomes more significant (18%) in the thin falling film and this is because a large portion of the profile is not available due to distortion.

3.7 Averaging Data

In order to characterize the turbulent velocity field in the Taylor bubble wake, ensemble averages of the velocity fields in this region were calculated. However, in contrast to the nose, the shape of the bottom surface of a Taylor bubble is unstable for most of the conditions studied in this thesis. Therefore, the shape of the bubble bottom is different from image to image. To overcome the problem of a fluctuating bottom location, the location of the interface at the tube centreline was determined using the Inspector® image processing software. The image processing steps to locate the bubble bottom are similar to the ones used to measure the shape of the bubble in the nose and the film region (Section 3.3). After the PIV image analysis and the post processing calculations were performed, the velocity field data were shifted axially based on the bubble bottom location for each bubble to make $Z = 0$ correspond to the bubble bottom for all images. Then an ensemble average of the shifted velocity field was calculated. This shifting and averaging is used to calculate the mean flow field in all cases (stagnant and flowing liquids) presented in this thesis. Figure 3-10 shows the comparison between the shifted and non-shifted averages of 503 PIV images for the axial velocity at the centreline of the tube in the wake of a Taylor bubble rising in stagnant water. It is clear from Figure 3-11 that the velocity at the bubble bottom for the shifted velocity field is very close to the bubble rise velocity (U_{TB} = 0.173 m/s). However, for the non-shifted case, the velocity at the bubble bottom is much smaller than the bubble rise velocity. Figure 3-12

shows the comparison for the axial V_{rms} at the tube centre as a function of the distance behind the bubble and it shows that the shifting has corrected the scattering in the values of axial turbulent fluctuations in the non-shifted average.

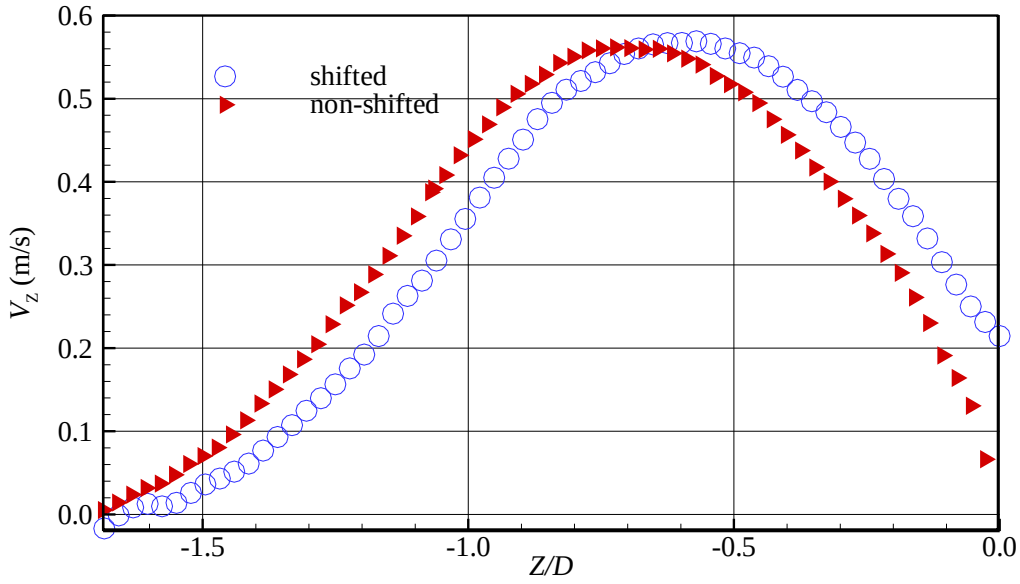

Figure 3-11: The mean axial velocity at the centerline of the tube as a function of the distance from the bubble tail for both shifted and non-shifted images.

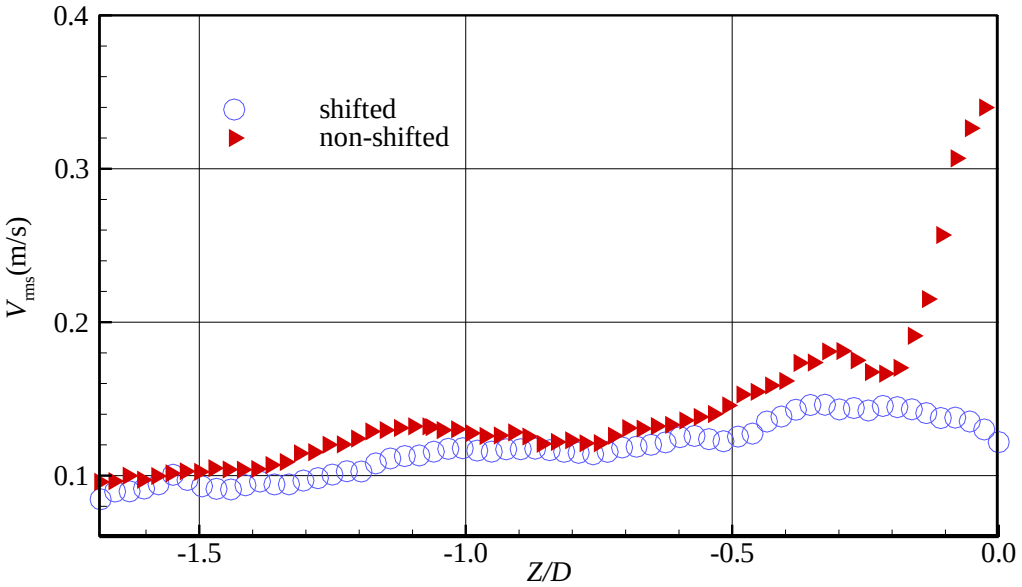

Figure 3-12: The axial turbulent intensity at the centerline of the tube as a function of the distance from the bubble tail for both shifted and non-shifted images.

4 Taylor Bubbles Rising in Stagnant Liquids: Results and Discussion

4.1 Introduction

In the next two chapters, the velocity field around Taylor bubbles rising in stagnant and upward flowing liquids is discussed. A detailed description of the liquid velocity measurements near the nose, in the film, and in the wake of Taylor bubbles is provided.

The velocity field is presented in the form of velocity vectors for the liquid around the bubble. In these plots, the vector length is proportional to the magnitude of the velocity. The root of the vector is placed at the location where the measurement is made. The spatial resolution of the velocity measurements is 0.0135D in the radial direction and 0.0270D in the axial direction. Figure 4-1 shows the coordinate system for the measurements. Axial positions (z) are positive above the nose and negative below the nose. In the wake, axial positions (Z) are measured from the bottom of the bubble. The frame of reference for these measurements is as seen by a fixed observer unless otherwise noted.

Table 4-1 shows the liquid viscosity (μ), measured bubble velocity (U_{TB}) and the dimensionless numbers (Re_{TB}, Eo, N) values produced from the tube diameter and the liquid properties. The measured rise velocity of the Taylor bubbles is constant for all three cases in Table 4-1. The behavior of the bubble in the so called inertia-controlled regime occurs when $Eo > 70$ and $N > 550$ (White and Beardmore, 1962) and $E_O > 100$ and $N > 350$ (Wills, 1969).

The conditions in Table 4-1 place the bubble behavior in the inertia-controlled regime. For the inertia-controlled regime, the Froude number (Fr) is constant at 0.345 and the rise velocity (U_{TB}) of the Taylor bubble can be calculated from

$$Fr = \frac{U_{TB}}{\sqrt{gD}} = 0.345. \quad 4.1$$

where D is the tube diameter and g is the acceleration due to gravity.

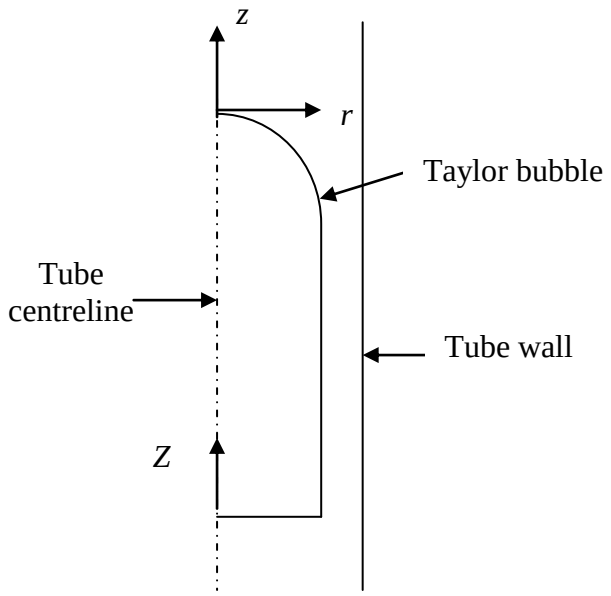

Figure 4-1: Coordinate system for the velocity measurements presented in this thesis

Table 4-1: Experimental conditions for the study of Taylor bubbles rising in stagnant liquids

Case number	μ(Pa·s)	U_{TB}(m/s)	Re_{TB}	*Eo*	*N*
Case 1	0.00100	0.173	4400	87.0	12,600
Case 2	0.00500	0.174	1000	110	2,850
Case 3	0.0430	0.175	120	114	352

Based on equation 4.1 the bubble rise velocity should be 0.172 m/s. The terminal velocity of the bubble measured using the phase transition detectors varied from 0.173 to 0.175 m/s for the three cases (refer to Appendix A). The maximum difference between the measured and the calculated rise velocity of the bubble was 1%.

4.2 The Velocity Field near the Nose and in the Film

Since the velocity fields above the noses are identical for the three liquid viscosities, the data presented in this section are for the Taylor bubble rising in stagnant water only (Case 1). The velocity vectors around the nose and in the film for this case are shown in Figure 4-2. This plot is an ensemble average of ten instantaneous velocity fields. The left side of the axis of symmetry shows all of the measurements while the right side shows only every fourth axial location to make the velocity field clearer. The velocity field in the nose region certainly shows the general characteristics expected in the flow. The rising bubble displaces the liquid ahead of it. The fluid at the centre of the tube moves upward while the fluid close to the wall moves downward. The fluid midway between the tube wall and the tube centre has a strong radial velocity toward the tube wall as the fluid moves away from the rising bubble. Near the nose of the bubble, the axial velocity of the fluid is approximately equal to the terminal velocity of the bubble and the direction is upward. The axial component of the velocity reduces quite rapidly ahead of the bubble.

Figure 4-3 shows the axial velocity on the tube axis as a function of the distance ahead of the bubble for the three stagnant cases. The effect of the viscosity on the velocity field in this region is essentially negligible under these conditions (inertia-controlled regime). This may

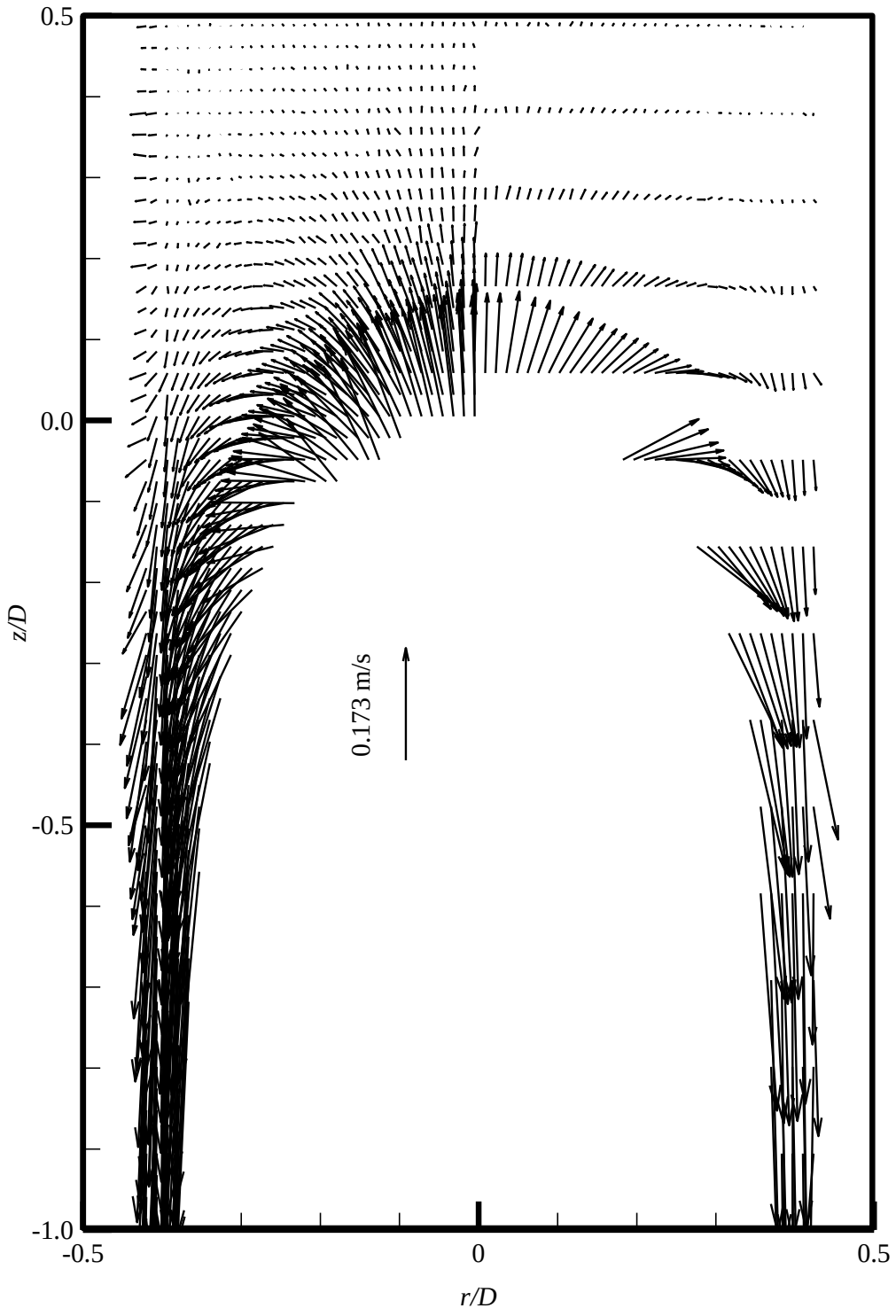

Figure 4-2: PIV measurements of the velocity field near the nose of a Taylor bubble rising in stagnant water (Case 1: Re_{TB} = 4,400, N = 12,600)

be due to the fact that the bubble rise velocity is constant and the shapes of the noses are very similar for the three cases. This is in contrast with the finding of Nogueira *et al.* (2006a) who stated that the disturbance of the bubble to the liquid is felt further for a liquid with low viscosity. This contrast may be due to the wide range of viscosities they used. At z/D=0.2, the axial velocity has reduced to 23% of the bubble velocity. At z/D = 0.28, it has reduced to 10% of bubble velocity and at z/D = 0.5 is reduced to 3% of the terminal velocity. This is in agreement with the findings of van Hout *et al.* (2002) for a Reynolds number of 4,350. Nogueira *et al.* (2003) found that, for a bubble rising in a viscous liquid (Re_{TB} = 70), the liquid velocity ahead of the bubble drops to 5% of bubble velocity at z/D = 0.24 and to 1% at z/D = 0.36. Bugg and Saad (2002) found that for Re_{TB} = 27 that at z/D=0.33 the velocity dropped to 5% of the bubble velocity. Polonsky *et al.* (1999a) refers to the onset of reverse flow at about z/D=0.66 for a bubble rising in water (Re_{TB} = 4,350).

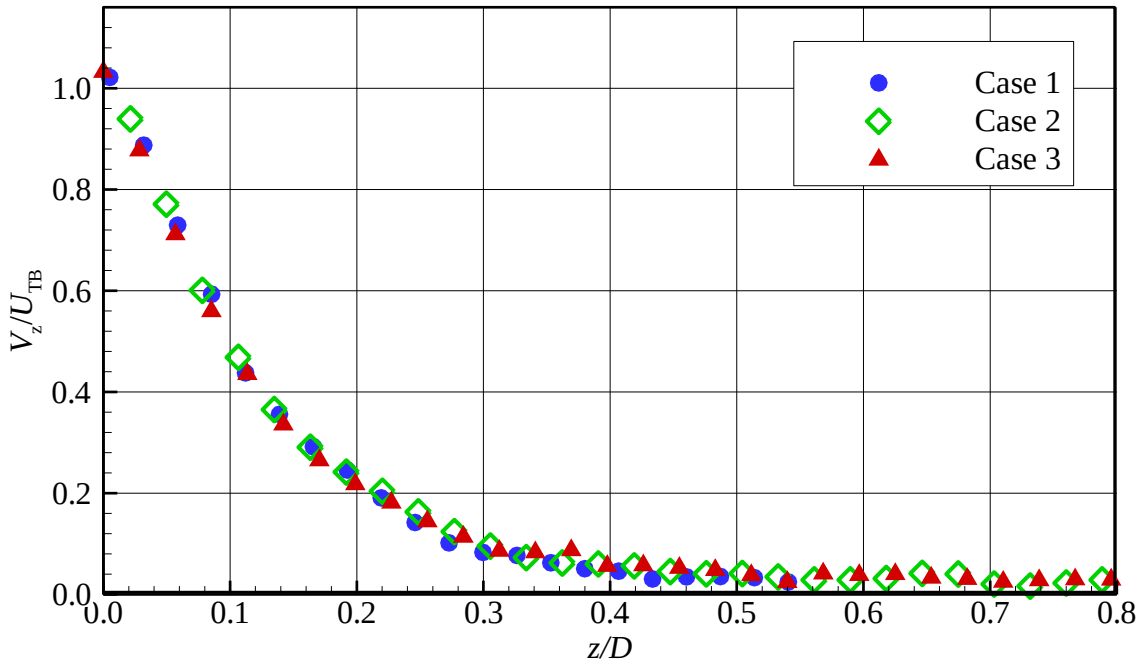

Figure 4-3: Axial velocity measurements along the tube axis above the nose of Taylor bubbles rising in stagnant liquids.

Figure 4-4 shows radial profiles of axial velocity at several axial locations above the nose. It is clear that the velocity profiles exhibit axial symmetry. It is interesting that there is only a moderate variation in the radial location of the flow reversal which is located at $0.25D < r < 0.30D$. Figure 4-5 shows radial profiles of radial velocity at the same locations. It shows that the maximum radial velocity is located between $0.1 < r/D < 0.2$ for all axial locations.

Figure 4-6 shows radial profiles of axial velocity at several axial locations in the film of a Taylor bubble rising in water. At z/D = -0.1, -0.2 and -0.4 the axial velocity profile is initially somewhat flat in the middle as the liquid flows downward. The liquid is essentially channeled by the interface and the tube walls. The velocity then increases with decreasing film thickness. At z/D = -0.7, the flat shape of the velocity profile has started to diminish and it is clear that axial velocity accelerates rapidly as the film thickness decreases. This is expected from a simple mass balance. At z/D = -0.9, the maximum axial velocity equals three times the rise velocity of the bubble. Note that the missing experimental data close to the wall are due to the optical distortions that occur there. Although not shown, the axial velocity must go to zero at the tube wall. The axial velocity increases until the film becomes fully developed. The velocity profile in the film exhibits zero shear stress (zero velocity gradient) at the bubble interface. Nogueira *et al.* (2006a) showed experimentally that the distance from the nose to achieve a fully developed film for a bubble rising in a stagnant liquid is $2.2D$.

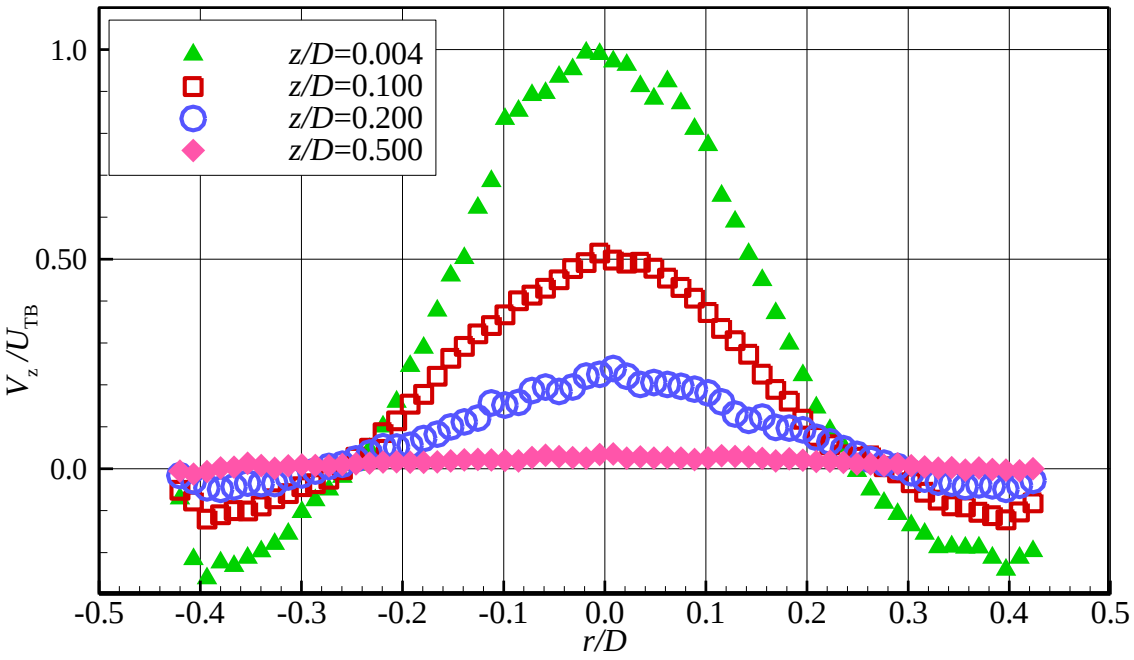

Figure 4-4: Radial profiles of axial velocity at four axial positions above the nose of a Taylor bubble rising in stagnant water (Case 1: Re_{TB} = 4,400, N = 12,600)

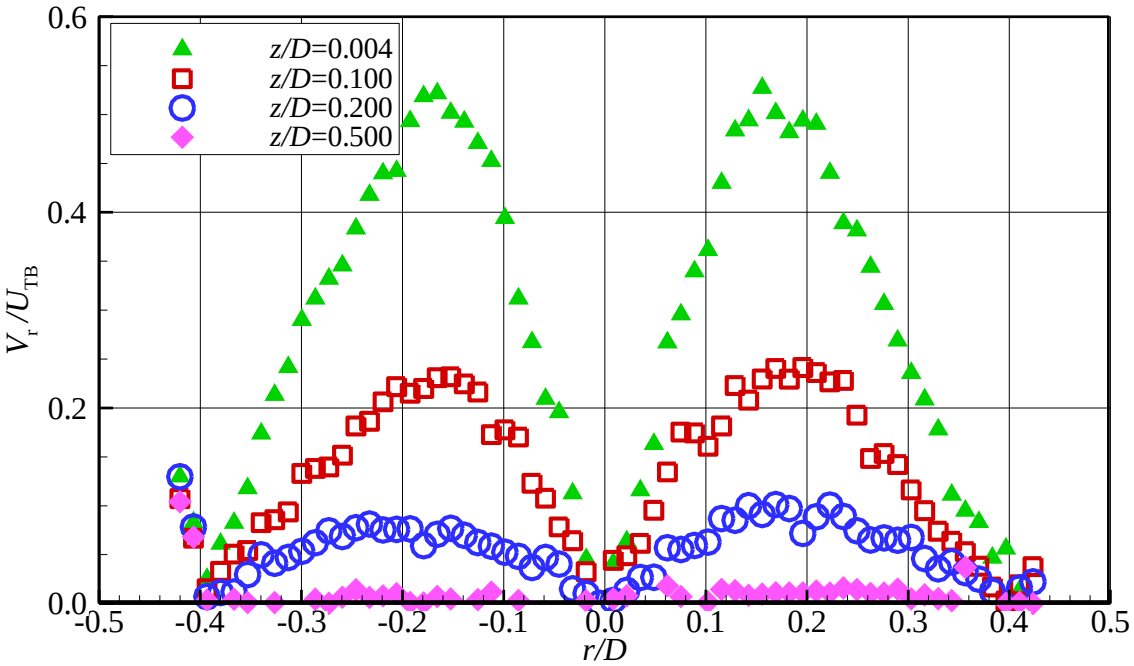

Figure 4-5**:** Radial profiles of radial velocity at four axial positions above the nose of a Taylor bubble rising in stagnant water (Case 1: Re_{TB} = 4,400, N = 12,600)

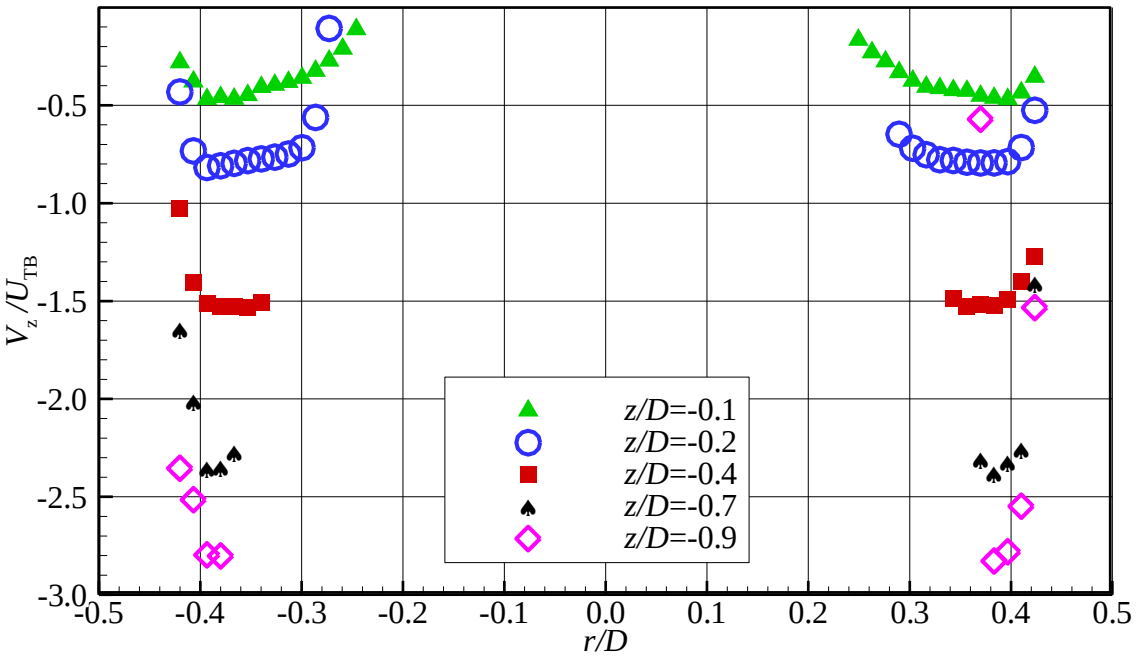

Figure 4-6: Radial profiles of axial velocity at four axial positions below the nose of a Taylor bubble rising in stagnant water (Case 1: Re_{TB} = 4,400, N = 12,600)

4.3 Wakes of Taylor Bubbles Rising in Stagnant Liquids

4.3.1 Introduction

Slug flow development is governed by Taylor bubbles interaction. In general, the trailing bubble is affected by the velocity field in the liquid ahead of it. The wake of the leading bubble strongly affects the shape and the velocity of the trailing bubble. Therefore, a detailed understanding of the hydrodynamics of Taylor bubble wakes is very important to the task of modeling slug flow. Measurements of the velocity field in the wake of a single Taylor bubble rising in stagnant liquid were performed for the three cases described in Table 4-1. Since the tube diameter is constant and the density is slightly changing the only variable in these cases is viscosity.

Before discussing the velocity field in the wake, the shape of the bubble bottom will be considered since this shape has a strong influence on the wake structure. Figure 4-7 shows examples of the bottom of Taylor bubbles rising in different stagnant liquids (see Appendix B). These images were extracted from PIV images and enhanced using Matrox Inspector® image processing software. In these images, the bottom part of the bubble, part of the near wake, and the falling film region can be seen clearly. The bright dots in the images are the PIV seeding particles. Figure 4-7(a) shows the highly irregular instantaneous shape of the Taylor bubble bottom when rising in stagnant water (Case 1). For these conditions, the shape of the bubble bottom is different from image to image. Figure 4-7(b) shows the flat instantaneous bottom of a Taylor bubble rising in liquid of a higher viscosity (Case 2) where the bottom edge of the bubble is much more rounded. For case 2, the instantaneous images are different and the bottom surface is fluctuating, however, the oscillation of the bubble bottom in this case is much weaker than in case 1. The bottom is not always axisymmetric around the tube axis but the edges are always rounded as in Figure 4-7(b). Figure 4-7(c) shows the concave shape of the bubble bottom rising in viscous liquid (Case 3). This shape is steady and the bottom edges are sharp. The shape of the bubble bottom certainly affects the way in which the falling film interacts with the liquid in the wake. This will be discussed further in the context of the velocity field measurements in the next section.

4.3.2 Mean Flow Field in the Wake

The mean velocity field is calculated by averaging 500 instantaneous fields in case 1, averaging 200 instantaneous fields in case 2, and presenting only 1 instantaneous field in case 3. The averaging was performed after the velocity fields were shifted relative to the bubble

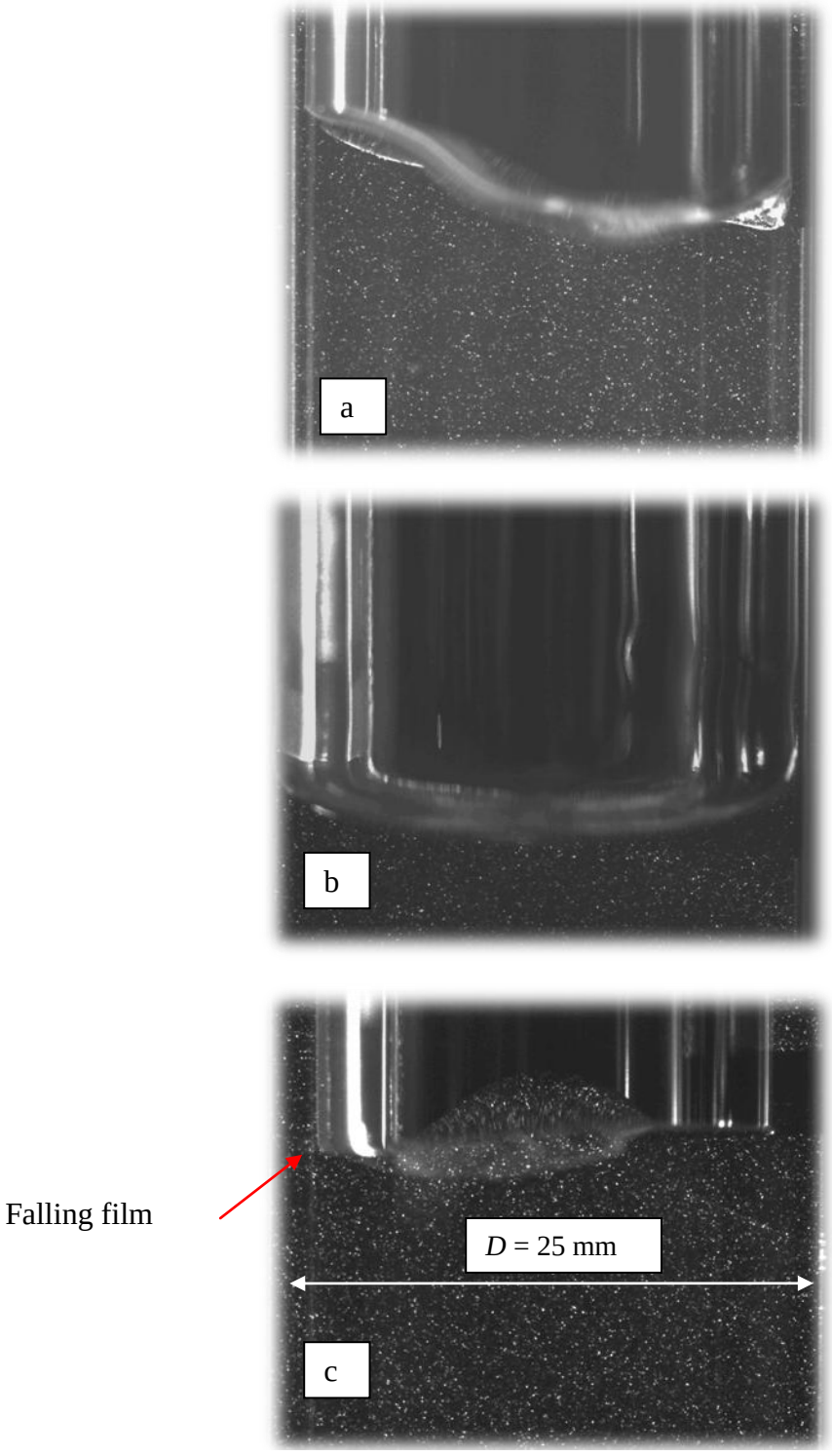

Figure 4-7: Shape of the bottom surface of Taylor bubbles rising in stagnant liquids: (a) Case 1 (Re_{TB} = 4,400, N = 12,600), (b) Case 2 (Re_{TB} = 1,000, N = 2,850) (c) Case 3 (Re_{TB} = 20, N = 352).

bottom as described in Section 3.7. The convergence of the ensemble averaged field for case 1 was checked. The variation of the mean velocity and the turbulent intensity with the number of samples (100, 200, 300, and 400) was plotted at a point in the wake of Taylor bubble. Converged mean and turbulent intensity values were obtained with 200 images. Since the mean flow is axisymmetric around the tube centreline, the results presented in this section were obtained by averaging the left and the right halves of the velocity fields thus doubling the ensemble size. As recommended by Adrian *et al.* (2000), it is important to consider a range of reference frame velocities in order to identify the majority of the turbulent eddies embedded in a velocity field. In the near wake the bubble rise velocity is used as the reference frame velocity. Therefore, the Taylor bubble velocity is subtracted from the measured velocities to yield a moving frame of reference fixed to the bubble. When using a moving frame of reference, the primary vortex (immediately behind the bubble bottom surface) becomes visible.

Figure 4-8 shows velocity vectors and streamlines in the near wake of a Taylor bubble rising in stagnant water (Case 1). At the bottom surface (Z/D = 0), the falling annular film near the tube wall penetrates into the liquid below the bubble driving a toroidal recirculation zone just behind the bubble. These wakes are classified as Type III wakes (turbulent) by Campos and Geudes de Carvalho (1988) and Pinto *et al*. (1998). The vortex core was located visually using Tecplot®360 to find where the axial and radial mean velocities are both zero. The core of the vortex is located at ~0.52D from the bubble bottom and about 0.28D from the tube centreline. These parameters are within the range given by Shemer *et al*. (2007). A stagnation point is located along the tube centreline. In a frame of reference moving with bubble

velocity, this stagnation point is located ~1.23*D* below the bubble. This agrees well with Sotiriadis and Thorpe (2005) for a bluff body and a ventilated cavity (created by continuously feeding air through a sparger into a down-flowing liquid) in a vertical tube of 10.5 cm diameter. They located the stagnation point at 1.3*D* below the bubble.

Figure 4-9 shows velocity vectors and streamlines in a frame of reference moving at the bubble velocity in the near wake of the bubble in stagnant liquid (Case 2). According to the classification of Campos and Geudes de Carvalho (1988) and Pinto *et al*. (1998) under these conditions, the flow in the wakes is also type III (turbulent). A very weak recirculation zone at the centre of the tube immediately underneath the bubble can be seen in Figure 4-9. Due to the very low velocities in this recirculation zone, it will be called the quiet zone in this thesis. Figure 4-7(b) shows that the bottom of the bubble is flat with a rounded corner and this may cause the existence of this quiet zone. This zone was also observed by Coppus *et al.* (1977) in the wake of spherical-cap bubbles. These bubbles were held stationary by down-flowing liquid in a tunnel (water/glycerol solutions). This zone was observed only in turbulent wake cases. In Figure 4-9, the core of the primary zone is located at ~ 0.68*D* from the bubble bottom and about 0.29*D* from the tube centreline. The axial position of the core centre is located further below the bubble bottom in this case than in the previous case. This may be due the existence of the quiet zone in this case. In this frame of reference, the first stagnation point is located along the tube centreline at the end of the quiet zone at Z = -0.25*D* and a second stagnation point is clearly located on the centreline at the end of the primary recirculation zone at Z=-1.2*D*.

For case 3 (viscosity is much higher), according to the classification of Campos and Geudes de Carvalho (1988) and Pinto *et al*. (1998), the wake is a type I laminar wake. Figure 4-10 shows instantaneous velocity vectors and streamlines in a frame of reference moving at the bubble velocity in the near wake of the bubble. The bubble bottom shape is stable and no oscillations occur. The falling film quickly spreads in the wake to occupy the entire tube cross section resulting in a significantly shorter primary recirculation region than in the previous cases. The core of the vortex is located at Z = -0.14D and r = 0.27D. The length of the primary recirculation zone is about 0.68D. This is more than 10% less than the length predicted by the formula of Campos and Guedes De Carvalho (1988). It is clear from the PIV images (Figure 4-4 c) that the bubble has a concave bottom in this case. Therefore, part of the recirculation region is hidden. This was noticed also by Bugg and Saad (2002) and Nogueira *et al*. (2003). The length of the recirculation zone measured here does not take into account the part of the wake inside the concave tail of the bubble. The length of this hidden part is about 0.15D. A summary of the primary vortex parameters for the three cases is given in Table 4-2.

In the three cases discussed in this chapter, the wake is the region where differences appear in the flow. In case 2, the existence of the quiet zone in the wake structure is the main difference from cases 1 and 3. One explanation for this is the rounded edges of the Taylor bubble bottom surface in case 2 as seen in Figure 4-7(b). From the PIV image, it was observed that the edge of the bottom (where the film expands into the wake) has a large radius of curvature. This may be what causes this difference. Lertnuwat and Bunyajitradulya (2007) numerically show that the primary recirculation zone (D = 100 mm, recirculation zone ends at Z= 0.95-1.2D, core vortex is located at r = 0.24-0.26D and Z = 0.25-0.30D) is sensitive to the trailing-corner radius of the Taylor bubble bottom (only in large corner radius, corner radius is10 mm).

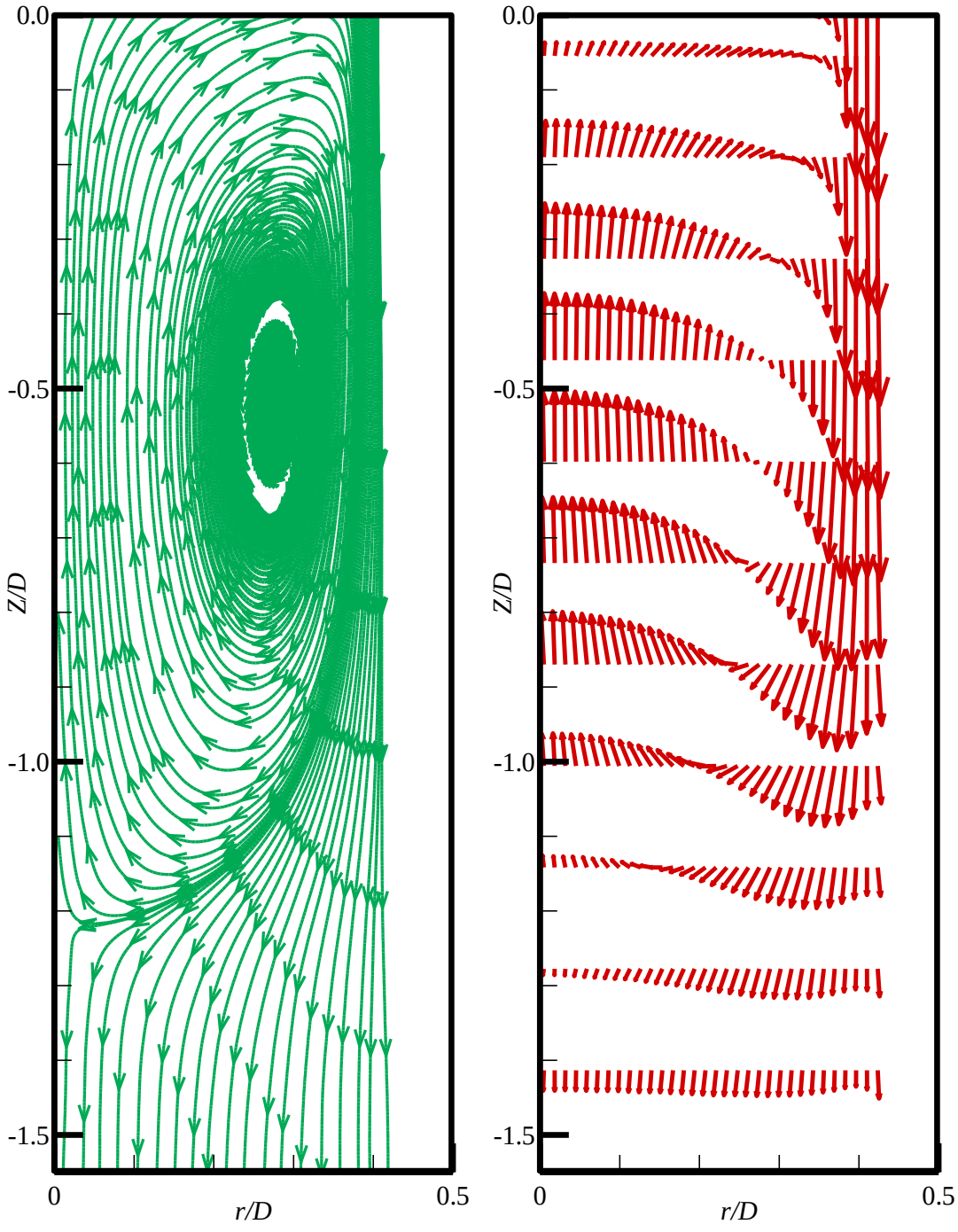

Figure 4-8: The mean velocity vectors and streamlines in the near wake of the Taylor bubble shown in a moving frame of reference (Case 1: Re_{TB} = 4,400, N = 12,600)

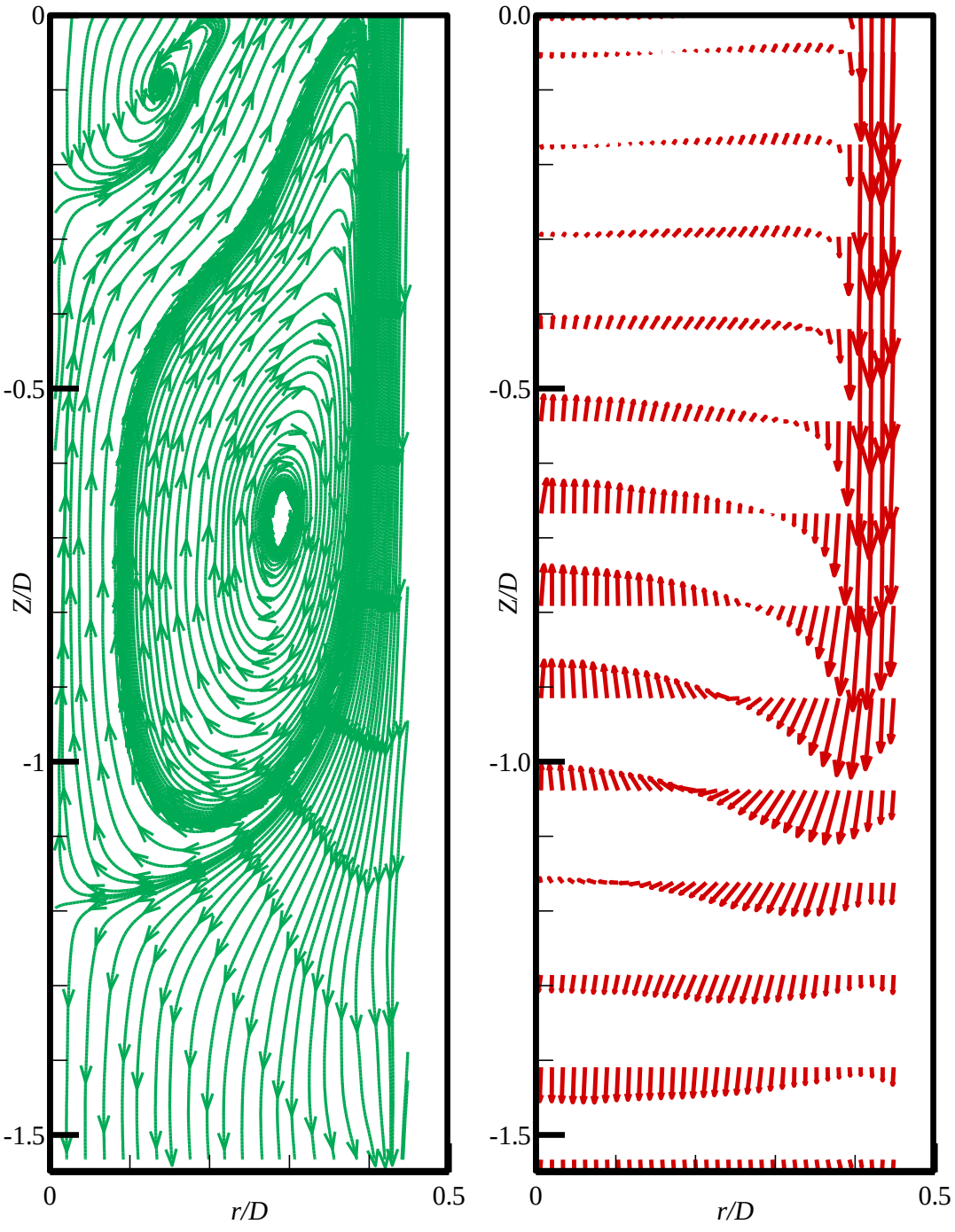

Figure 4-9: The mean velocity vectors and streamlines in the near wake of the Taylor bubble shown in a moving frame of reference (Case 2: Re_{TB} = 1,000, N = 2,850).

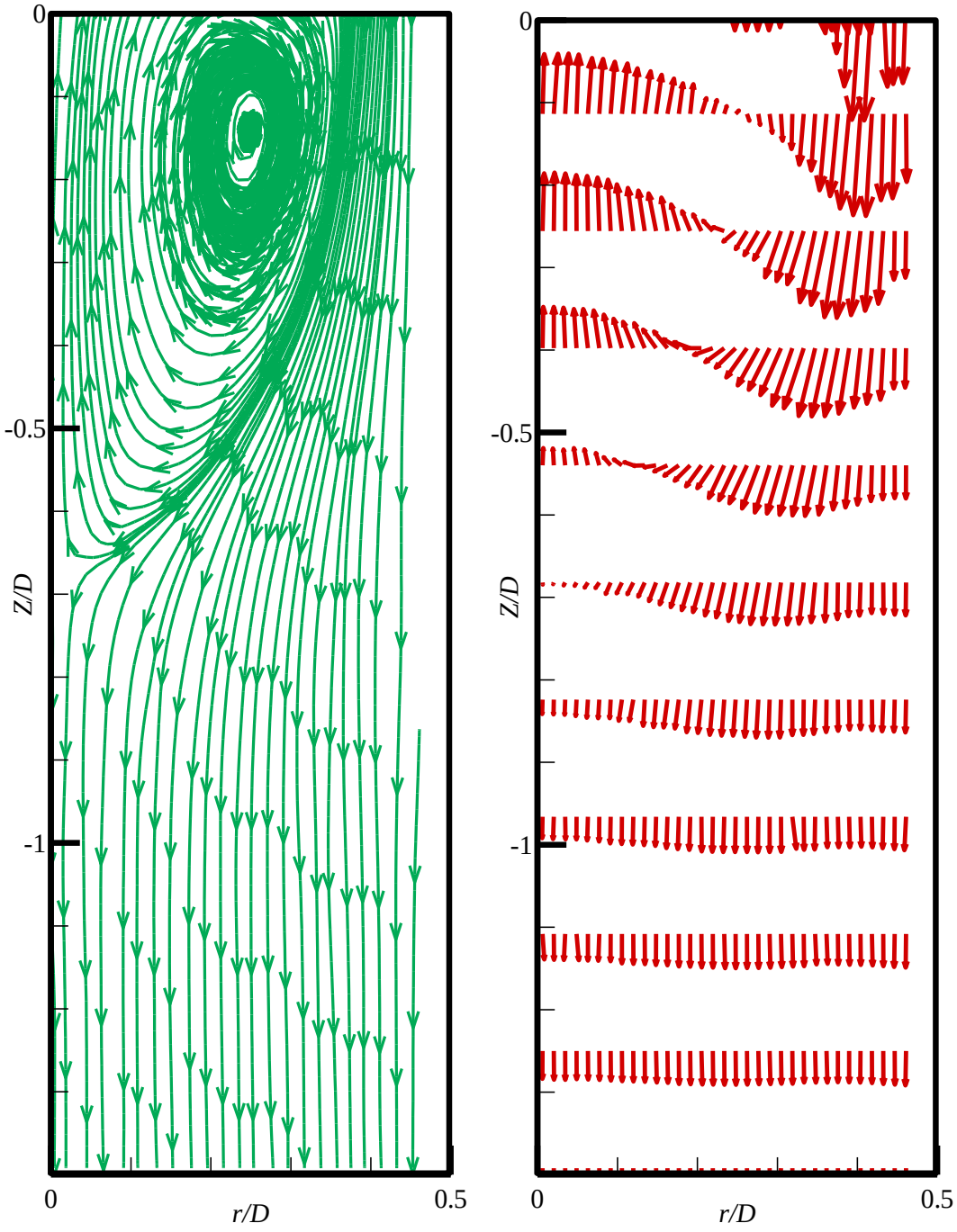

Figure 4-10: The instantaneous velocity vectors and streamlines in the near wake of the Taylor bubble shown in a moving frame of reference (Case 3: Re_{TB} = 120, N = 352)

Table 4-2: Summary of the main vortex parameters for the stagnant cases

Case #	μ (Pa·s)	Vortex core location		Wake pattern	Primary recirculation zone length
		Z/D	*r/D*		
Case 1	0.00100	-0.52	0.28	Turbulent	1.23*D*
Case 2	0.00500	-0.68	0.29	Turbulent	1.20*D*
Case 3	0.0430	-0.14	0.27	Laminar	0.68*D*

In order to quantify the size of the primary recirculation zone, the dividing streamline is introduced. The dividing streamline is defined as the streamline that ends at the stagnation point on the centerline and separates the falling film from the recirculation zone in a moving frame of reference. It is used to quantify the length of the recirculation zones. These lines are shown in Figure 4-11.

As discussed by Adrian *et al.* (2000), in order to identify the majority of the turbulent eddies embedded in a velocity field, the velocity field must be viewed in a frame of reference that moves at the same velocity as the core of the vortex. Therefore, it is important to consider range of reference frame velocities. The range of reference frame velocity that could be used is from 0 to U_{TB}. In the near wake, the bubble rise velocity was used as the reference frame velocity and it showed the vortices that were trapped (the primary vortex in Figures 4-8 to 4-10) in the near wake. In cases 1 and 2, an additional weaker vortex with an opposite sign of rotation exists after the primary vortex. In order to make this vortex more visible, the reference frame velocity must be selected to produce closed streamlines.

Figure 4-12 illustrates the effect of reference frame velocity on the visualization of this

vortex for case 2. In Figure 4-12(a), with a reference frame velocity of zero, the vortex is not well identified (the vortex core is not seen clearly). The suitable reference frame velocity is shown in Figure 4-12(b). Overestimation of the reference frame velocity again results in fewer closed streamlines as seen in Figure 4-12(c). It is clear from the figures that this vortex rotates in the opposite direction of the primary vortex.

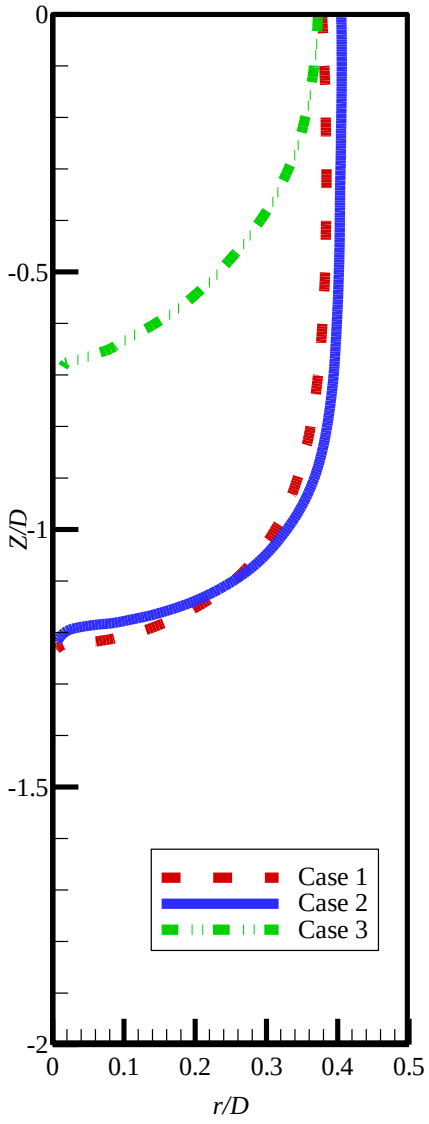

Figure 4-11: Dividing streamlines for the three cases in a moving frame of reference

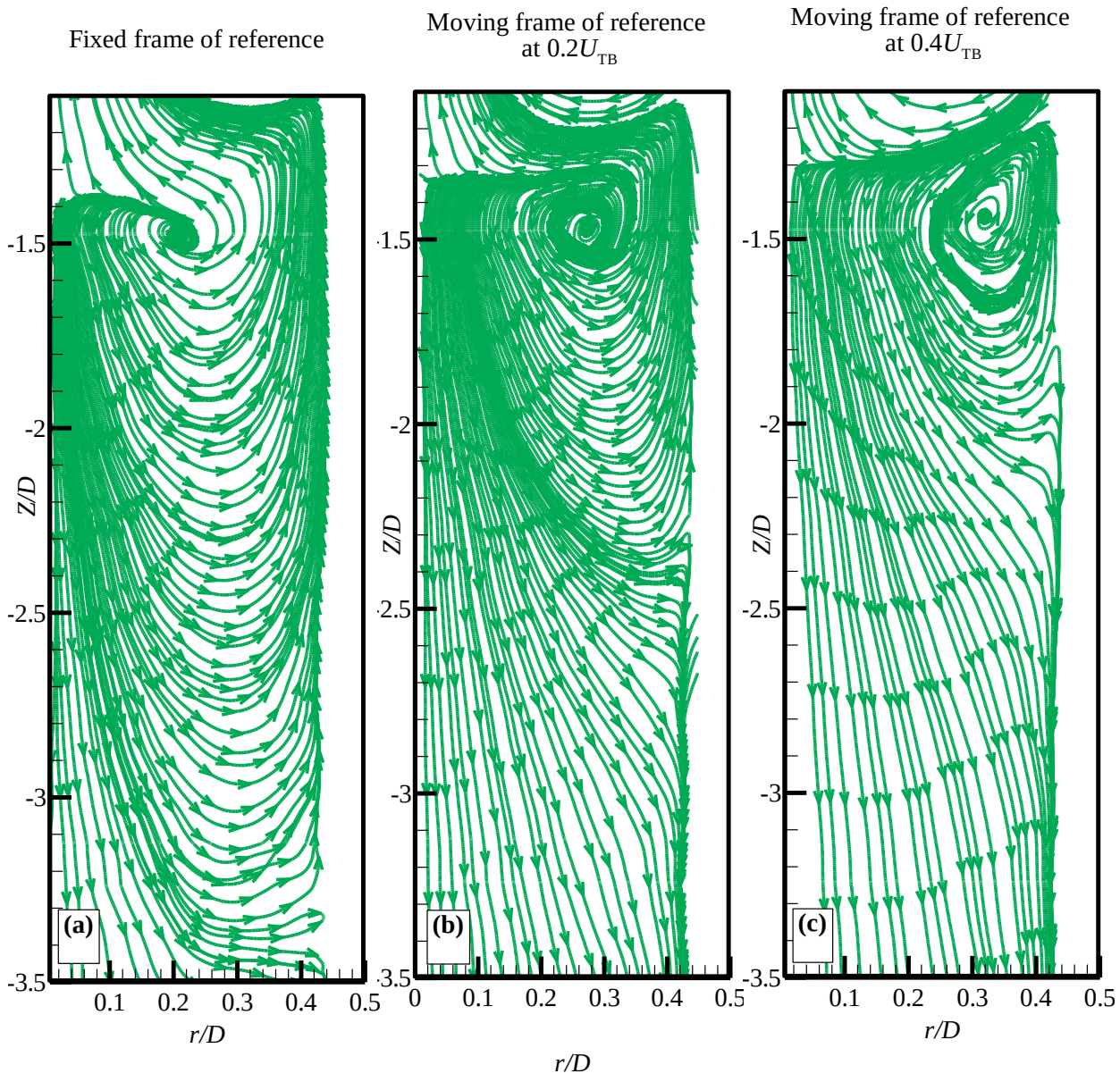

Figure 4-12: Effect of reference frame velocity on the visualization of vortices for Case 2

4.3.3 Axial Velocity Profiles

Radial profiles of the mean axial velocity at various axial locations in the wake of the bubble are presented in Figure 4-13 (Case 1). In this figure, the frame of reference is fixed relative to a stationary observer. Immediately behind the bubble (Z = -0.01D), the axial velocity profile

in the central region is approximately flat and the value of the velocity is close to the terminal velocity of the bubble. In the Z = -0.5D and Z = -1D profiles, at the centre of the tube the liquid core moves upward with a velocity larger than the terminal velocity of the bubble. This core extends from the tail to around 1.23D below the bubble's bottom surface (as seen in Figure 4-8). The falling liquid film entering the wake can be considered as an axisymmetric annular wall jet impinging on the stagnant liquid below the bubble. The velocity of the falling liquid film reduces and the film spreads in the liquid behind the bubble. The maximum downward velocity measured was $4U_{TB}$. At Z = -2D, in contrast to the previous profiles, the liquid core is moving downward at the centre of the tube with a very low velocity and close to the wall the liquid is moving upward. This is an indication of an existence of another vortex with an opposite sense of direction to the main vortex. Note that because these bubbles are rising in a stagnant liquid, each of these profiles should yield zero mass flow rate when integrated across the tube cross section.

Radial profiles of the axial velocity at various axial locations in the wake of the bubble (Case 2) are presented in Figure 4-14. Immediately behind the bubble (Z = -0.01D), the axial velocity profile shows that the liquid velocity near the tube centre is very close to the terminal velocity of the bubble. At Z = -0.4D, the axial velocity profile near the tube axis (r/D < 0.30) is flat and the value of the velocity is higher than the terminal velocity of the bubble. At Z = -0.8D, near the centre of the tube, the liquid core moves upward with a velocity larger than the terminal velocity of the bubble (see also Figure 4-9). The maximum value of the axial upward velocity equals $2.3U_{TB}$. This core extends from the tail to around 1.2D below the bubble tail. The falling film width increases with increasing distance from the

bubble bottom. The maximum downward velocity is around four times the bubble rise velocity. The downward velocity decreases as the falling film spreads in the stagnant liquid.

Radial profiles of the axial velocity at various axial locations in the near wake of the bubble (Case 3) are presented in Figure 4-15. Behind the bubble (Z = -0.01D), the axial velocity profile shows that the liquid velocity around the tube centre is much higher than the terminal velocity of the bubble. This is resulting from the concave shape of the bubble bottom surface. The maximum value of the axial upward velocity is 2.8U_{TB}. The maximum downward velocity is around twice the bubble rise velocity.

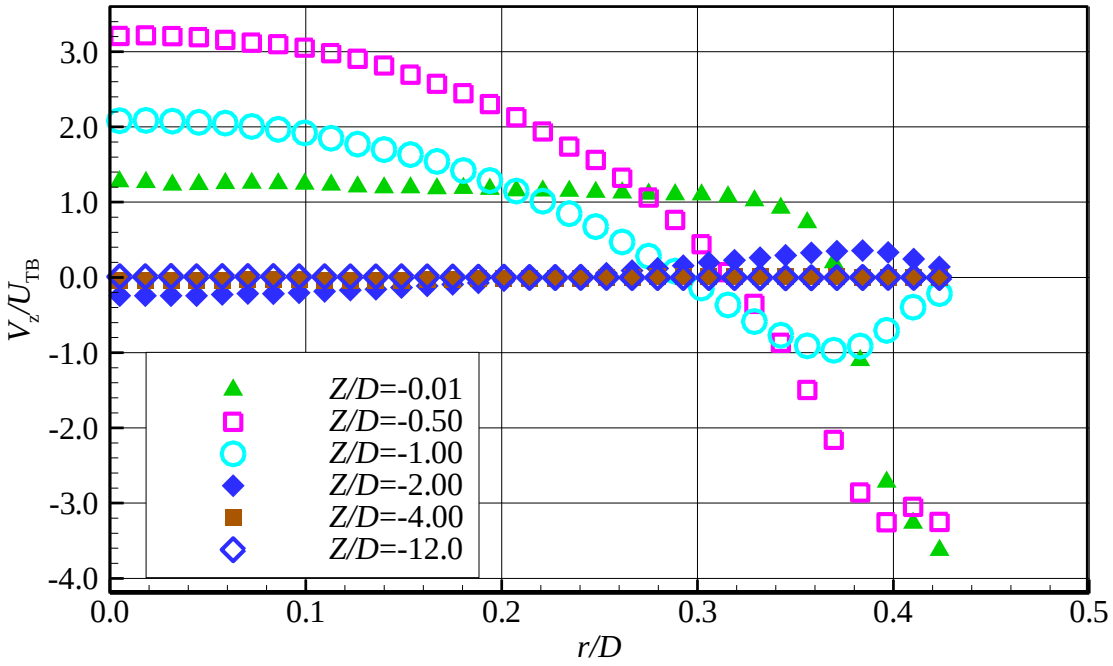

Figure 4-13: Radial profiles of axial velocity at various axial positions in the wake of a Taylor bubble rising in stagnant water (Case 1: Re_{TB} = 4,400, N = 12,600)

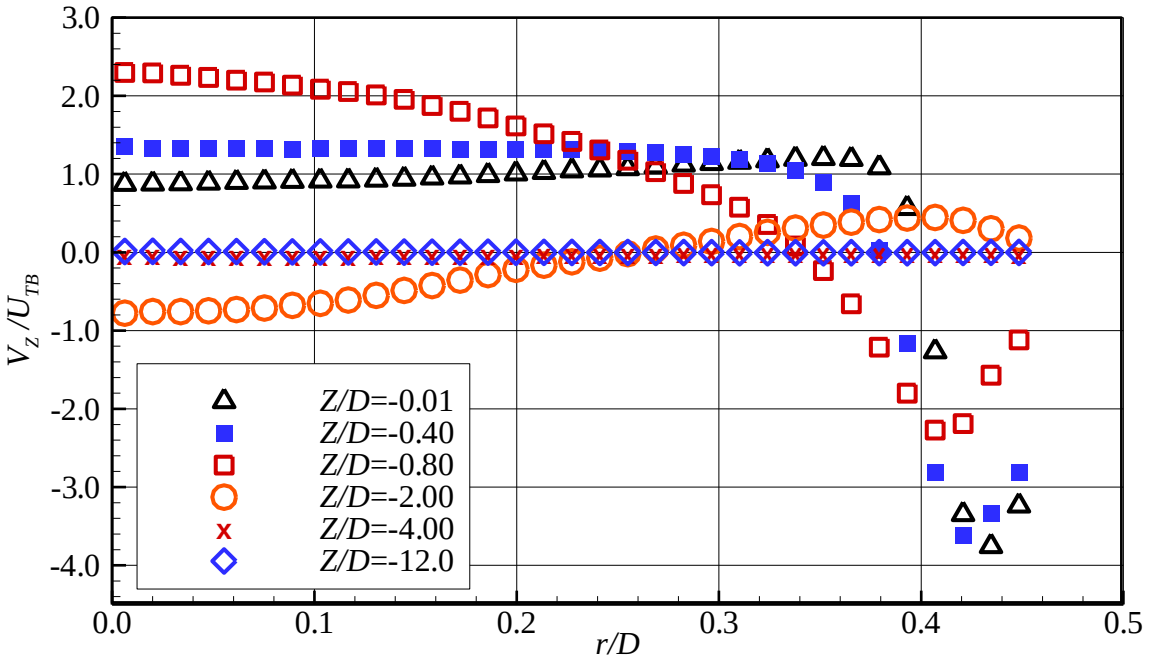

Figure 4-14: Radial profiles of axial velocity at various axial positions in the wake of a Taylor bubble (Case 2: Re_{TB} = 1,000, N = 2,850)

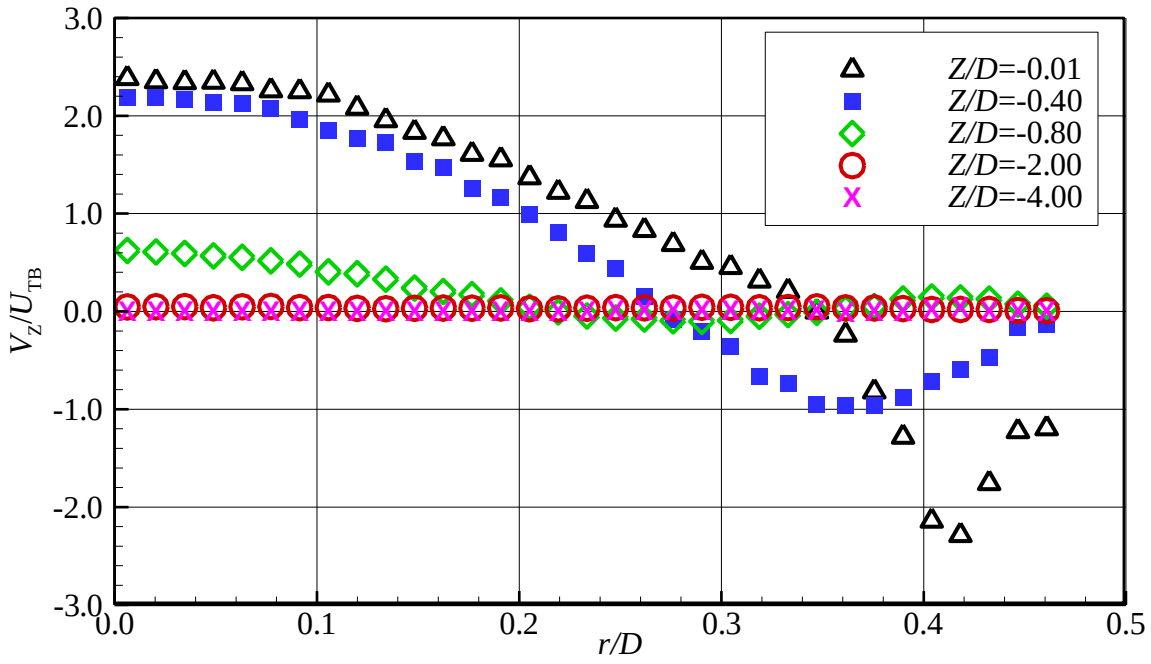

Figure 4-15: Radial profiles of axial velocity at various axial positions in the wake of a Taylor bubble (Case 3: Re_{TB} = 120, N = 352)

Since the scaling velocity for the three cases is the same (U_{TB}), the velocity profiles will now be compared in the same figure. In Figure 4-16, radial profiles of axial velocity were selected at three axial locations for the three cases. These locations were (1) near the bubble bottom, (2) at the core of the first large vortex and (3) at the stagnation point on the centreline. At the bottom surface of the bubble (lines), the shape of the velocity profiles is very similar for Case 1 and Case 2. However, around the tube centreline, the upward axial velocity is slightly higher than the bubble velocity in Case 1 and it is slightly lower than the bubble velocity in Case 2. In Case 3, the velocity ($r/D < 0.2$) is much higher than the bubble rise velocity. At the vortex core (open symbols), the downward velocity (close to the tube wall) decreases with increasing liquid viscosity. In other words, the highest downward velocity is in Case 1. For the upward velocity (around the tube centreline), the highest upward velocity is in Case 1 and the lowest in Case 2. This may be due to the quiet zone in Case 2. At the stagnation point (solid symbols), the three profiles almost collapse. The velocity at the centreline is at the bubble rise velocity, and it goes to zero at the tube wall.

Figure 4-17 shows the axial velocity on the tube centreline as a function of the distance from the bubble bottom surface in a fixed frame of reference. For Case 1, the axial velocity at the tube axis initially increases from a value close to the Taylor bubble rise velocity ($1.2U_{TB}$) to reach a maximum value ($3.25U_{TB}$) at a distance of around Z=-0.6D. It then decreases rapidly and equals the rise velocity of the bubble around Z =-1.23D and becomes zero at Z=-1.7D. It becomes negative (-0.32U_{TB} at Z=-2.3D) and eventually returns to zero at around Z=-4.7D. This change in sign is strong evidence of the existence of a sequence of vortices with

opposite senses of rotation. This observation was also reported by van Hout *et al*. (2002) and Dejesus *et al.* (1995). An example of this is clearly demonstrated in Figure 4-12 for Case 2.

In Figure 4-17 Case 2, the axial velocity on the tube axis initially increase from a value of slightly less ($0.9U_{TB}$) than the Taylor bubble rise velocity to reach a maximum value ($2.3U_{TB}$) near $Z = 0.8D$. It then decreases rapidly and equals the rise velocity of the bubble $Z= -1.2D$ and becomes zero at $Z = -1.4D$. In this case, the maximum upward axial velocity magnitude is lower than that of Case 1 and Case 3. The magnitude seems to be reduced by the presence of the quiet zone. It becomes negative ($-0.82U_{TB}$ at $Z =-1.8D$) and eventually returns to zero at around $Z = -4.6D$. This change in sign confirms the existence of a sequence of vortices with opposite senses of rotation as in Case 1. Again, an example of this is clearly demonstrated in Figure 4-12 for Case 2. However, the downward velocity in the second vortex is stronger for this Case 2 than in Case 1.

For Case 3 in Figure 4-17, due to the concave bottom of the bubble, the axial velocity at the tube centre initially is much larger ($2.35U_{TB}$) than the Taylor bubble rise velocity. Then it increases to reach a maximum value ($2.8U_{TB}$) at a distance of around $Z = -0.2D$. It then decreases quickly to U_{TB} at $Z =-0.64D$ and becomes zero around $Z = -4D$. In this case, there is no sequence of vortices as in the two previous cases.

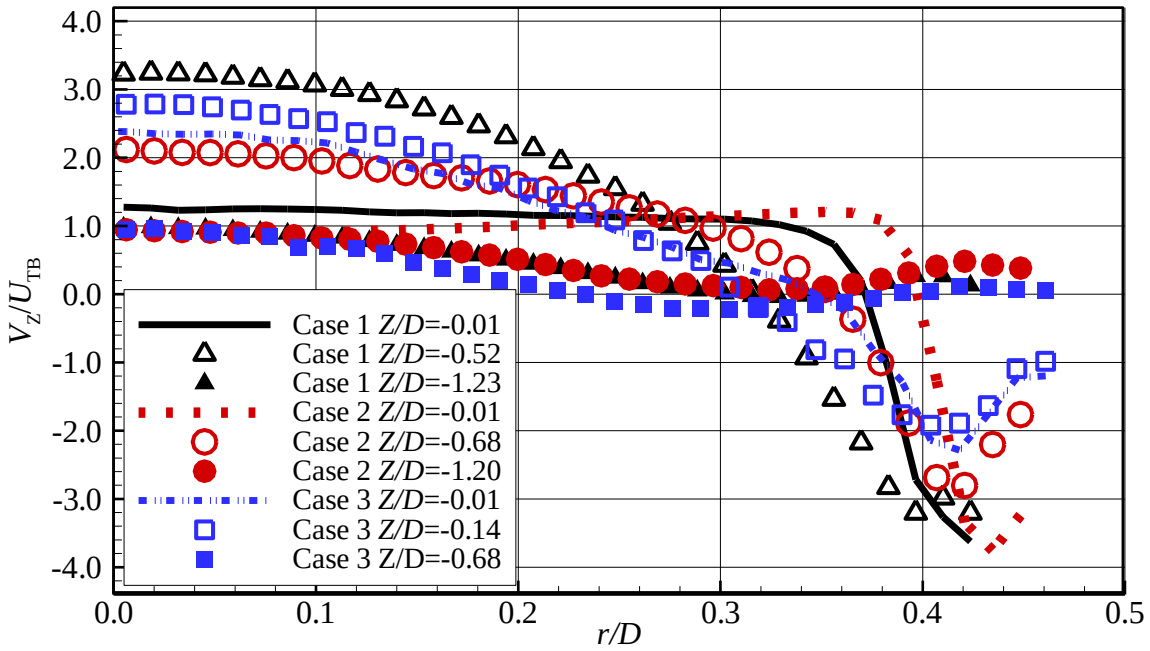

Figure 4-16: Comparison of radial profiles of axial velocity at selected axial locations in the wake of Taylor bubble rising in stagnant liquids

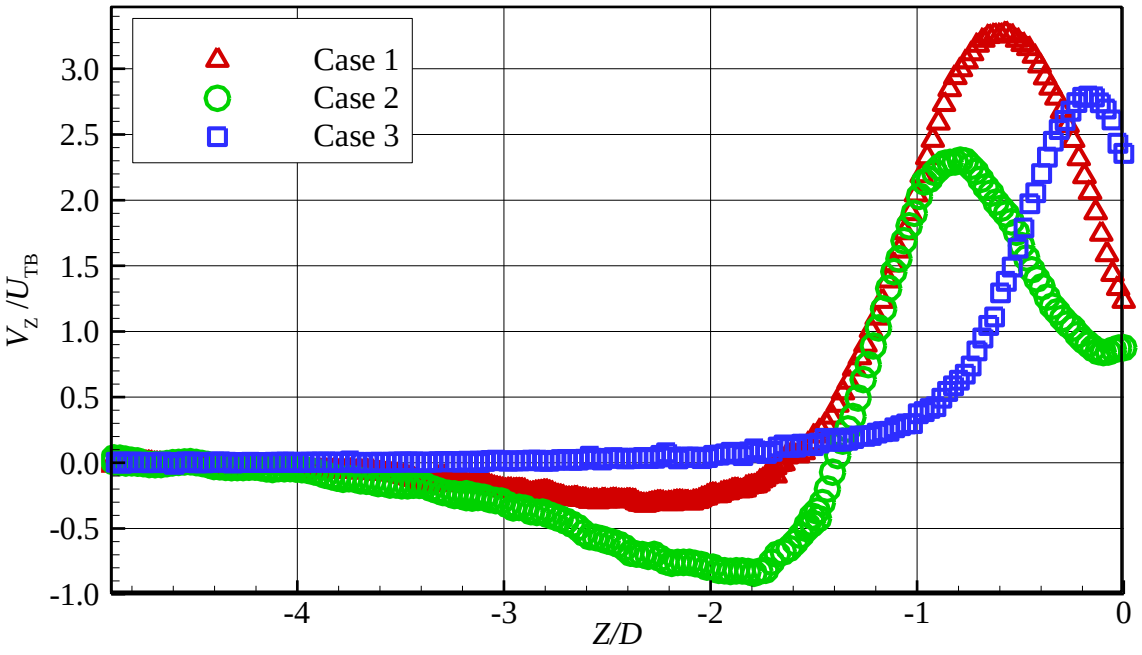

Figure 4-17: Comparison of the axial velocity at the centreline of the tube in the wake of Taylor bubbles rising in stagnant liquids

4.3.4 Radial Velocity Profiles

Radial profiles of the radial velocity at different axial locations behind the bubble for the three cases are illustrated in Figure 4-18 through Figure 4-20. The magnitude of the radial velocity is much lower than the axial velocity. The direction and behavior of the radial velocity in these figures are consistent with the vortex pattern presented in Figure 4-8 through Figure 4-10. The largest radial velocities occur midway between the wall and the tube centreline. The highest negative value (towards the centreline) of the velocity is located at near Z=-1D for Cases 1 and 2. It is near Z=-0.4D for Case 3. The highest positive value is located at about Z=-0.01D *f*or Cases 1 and 3 and it is located at about Z = -0.4D for case 2. For case 2, the highest positive value is also seen at Z = -2D which is an indication of the existence of another vortex in the wake. The radial velocity becomes very small and the radial velocity essentially vanishes at Z=-4D for Cases 1 and 2 and at Z=-1D for Case 3.

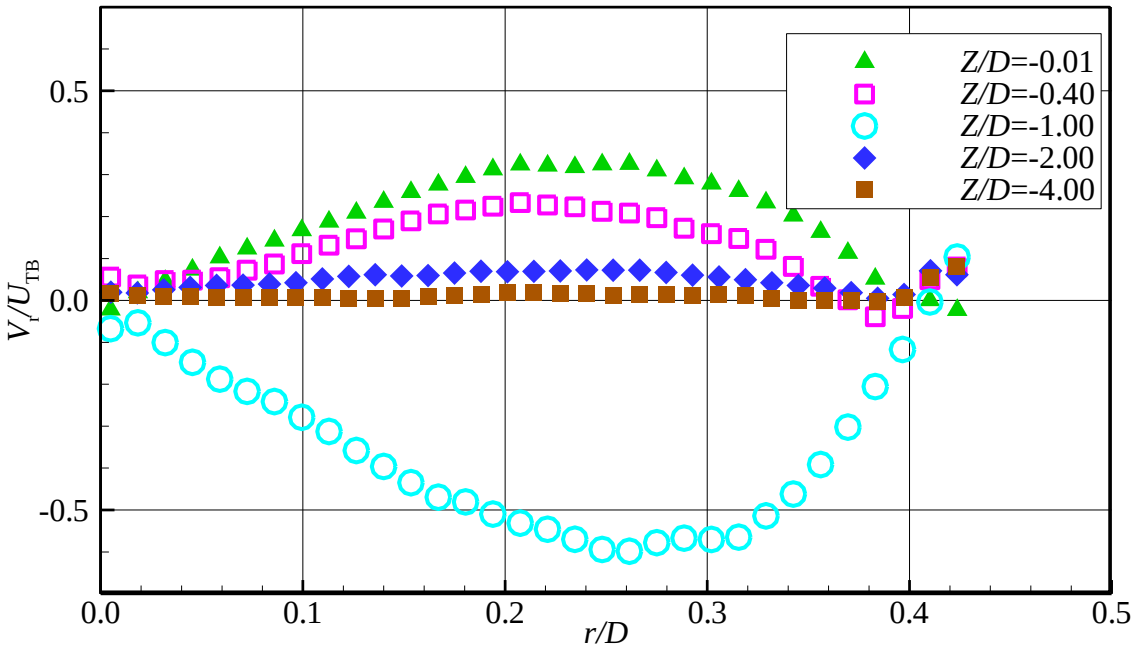

Figure 4-18: Radial profiles of radial velocity at various axial positions in the wake of a Taylor bubble rising in stagnant water (Case 1: Re_{TB} = 4,400, N = 12,600).

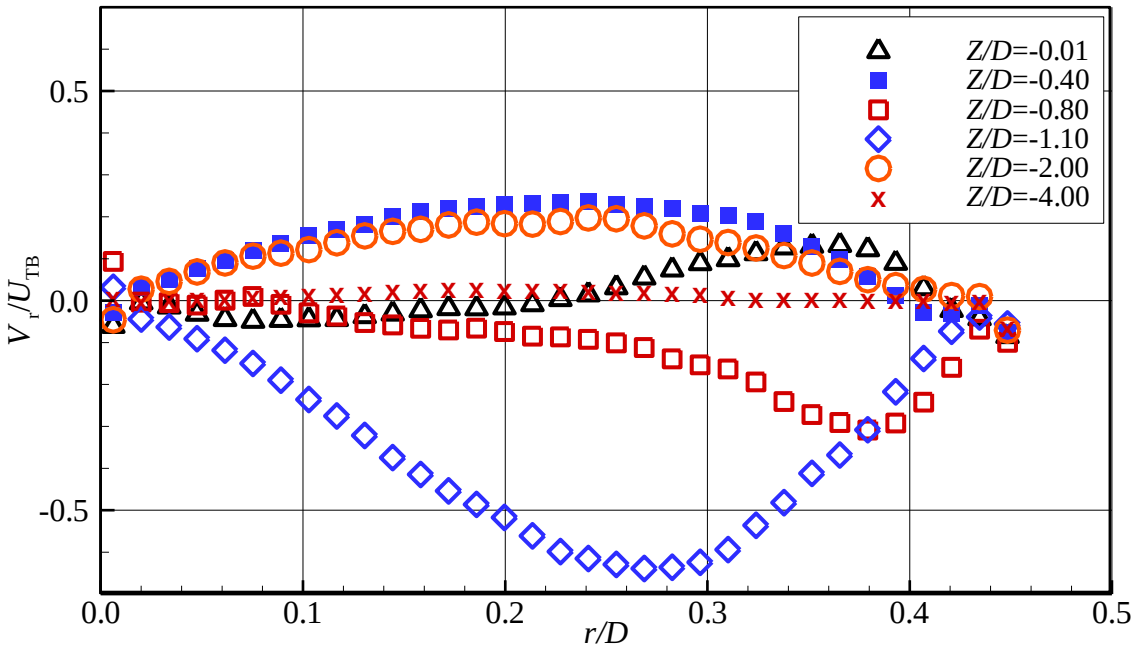

Figure 4-19: Radial profiles of radial velocity at various axial positions in the wake of a Taylor bubble (Case 2: Re_{TB} = 1,000, N = 2,850).

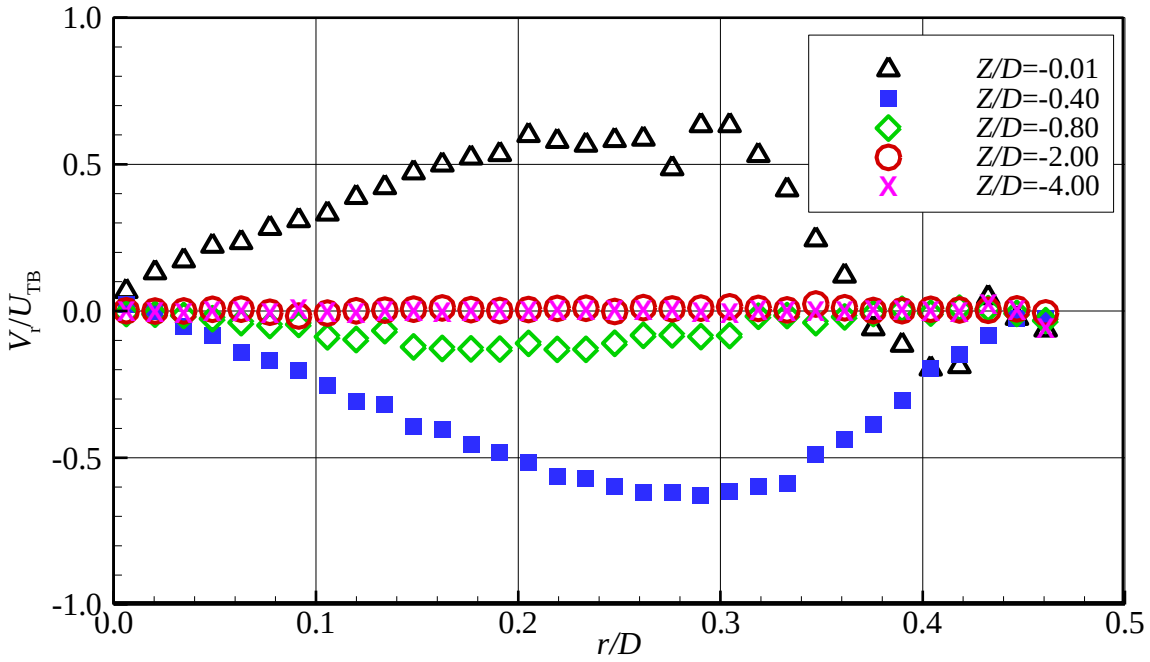

Figure 4-20: Radial profiles of radial velocity at various axial positions in the wake of a Taylor bubble (Case 3: Re_{TB} = 120, N = 352).

A comparison of radial velocity profiles for the three cases at three axial locations is shown in Figure 4-21. These locations were (1) near the bubble bottom, (2) at the core of the first large vortex and (3) at the stagnation point on the centreline. For the three cases, the radial velocity profiles at the stagnation points (solid symbols) are very similar. For all cases, the radial velocity is zero at the tube centerline and has negative values close to the tube wall. The positive values of the radial velocity are not always observed at the bubble bottom (lines) as expected where the counter-rotating toroidal vortex is observed (as in Case 1). However, the existence of the quiet zone in Case 2 and the concave shape of the bubble bottom in Case 3 affect the radial velocity at the bottom. At the bubble bottom (lines), the highest positive value is in case 3. This is because the measurement is actually located far for the liquid gas interface (concave). In Case 2 (Z=0.01D), the radial velocity value is very low and this again may be due to the quiet zone. Case 1 (Z=0.01D), the positive value of the radial velocity is located at the bubble bottom as expected.

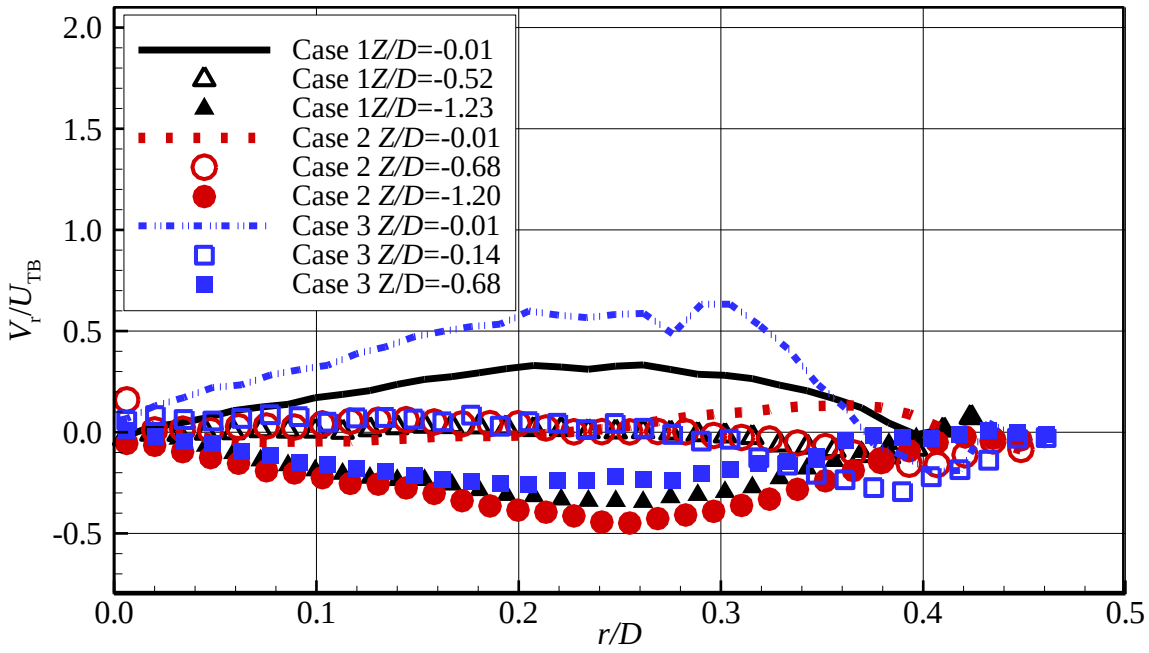

Figure 4-21: Comparison of radial profiles of radial velocity at selected axial locations in the wake of Taylor bubble rising in stagnant liquids

4.3.5 Axial Velocity Fluctuations

Axial velocity fluctuations (Case 1) are illustrated in Figure 4-22. These data confirm that the flow in the wake is turbulent. The maximum value of the fluctuation occurs in the strong shear layer where the falling film interacts with the recirculation zone. Due to spreading of the annular jet, the peak of the fluctuations close to the wall tends to flatten as the distance increases from the bubble bottom. The large fluctuations are immediately behind the bubble (*Z/D*= -0.01). It is interesting to note that the radial profiles of the fluctuations near the bubble bottom (*Z/D*= -0.01) and at *Z/D*= -0.5 have two maxima peaks and two minima. The first maximum is in the shear layer and the value decreases strongly to hit the first minimum value. It increases again but not as high as the first maximum then decreases slightly to the second minimum at the tube centre. In this stagnant liquid case, the fluctuations decrease with distance away from the bubble bottom and become very small by around *Z/D* = -12. The axial turbulent fluctuations on the tube centreline at *Z/D* = -0.01, *Z/D* = -0.5 and *Z/D* = -1 are equal. However, further behind the bubble the axial turbulent fluctuations decay with increasing distance from the bubble tail.

Axial velocity fluctuations for Case 2 are illustrated in Figure 4-23. As in the previous case, the fluctuations are higher in the near wake (*Z/D* = -0.01, *Z/D* = -0.4 and *Z/D* = -0.8) than those in the far wake (*Z/D* = -4 and *Z/D* = -12). The axial fluctuation decays with increasing distance from the bubble bottom. The maximum value of the fluctuation is attained in the region of the mixing layer between the falling film and the upward velocities at the core of the tube.

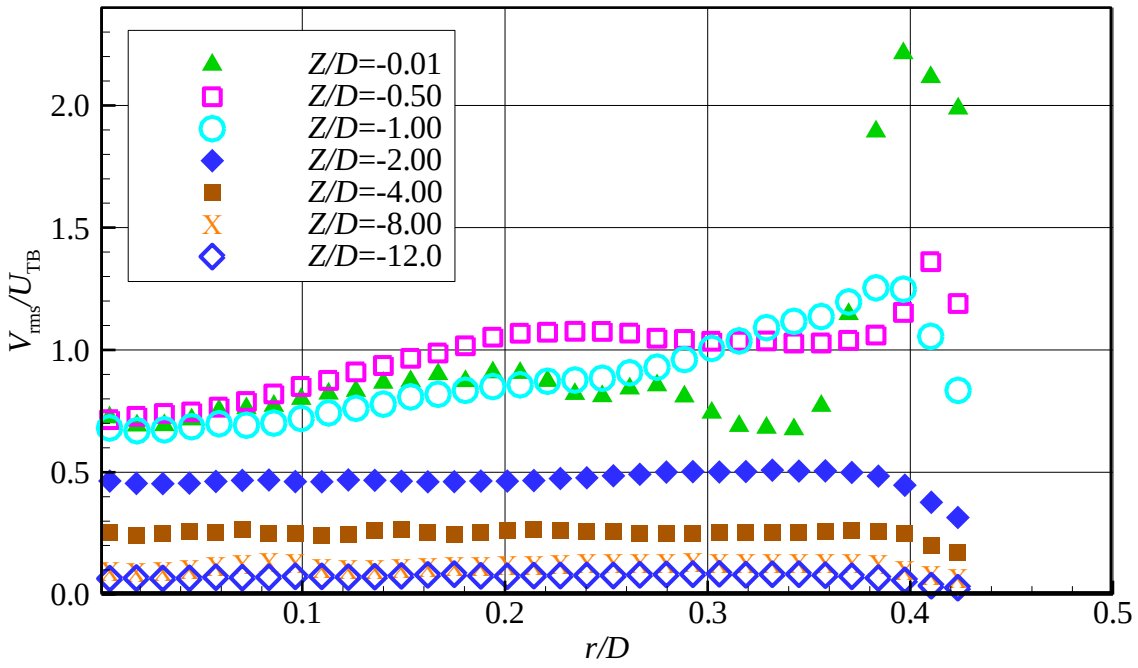

Figure 4-22: Radial profiles of axial turbulence intensity at various axial positions in the wake of a Taylor bubble rising in stagnant water (Case 1: Re_{TB} = 4,400, N = 12,600)

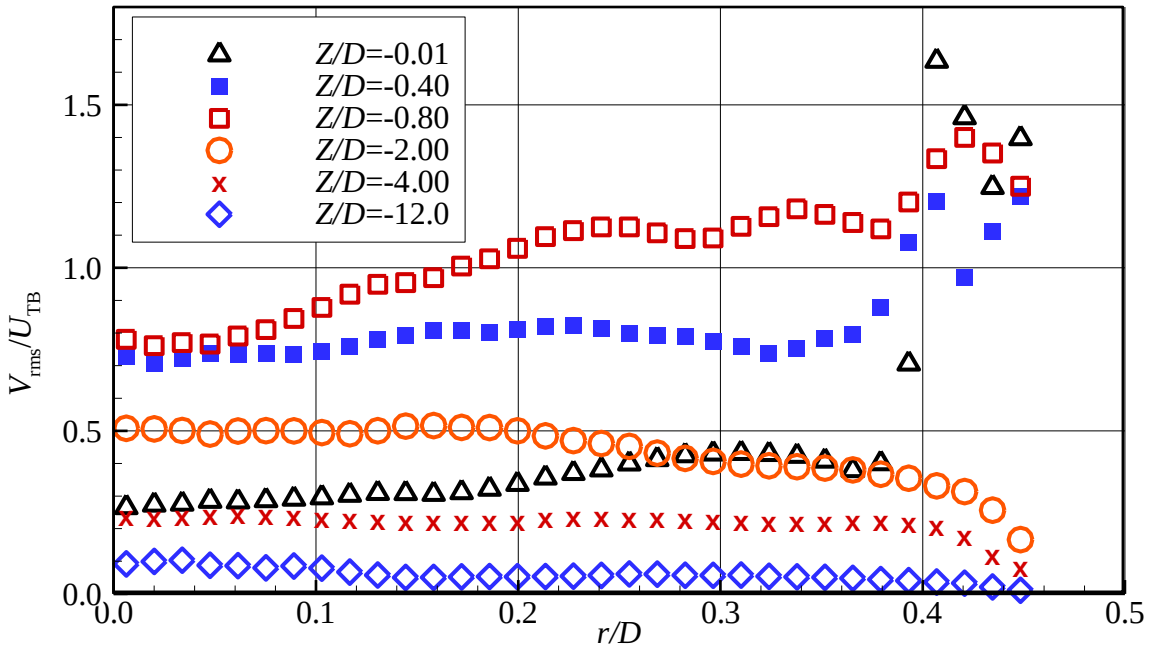

Figure 4-23: Radial profiles of axial turbulence intensity at various axial positions in the wake of a Taylor bubble (Case 2: Re_{TB} = 1,000, N = 2,850).

For Case 3, the wake is laminar therefore it is not presented in this section. The distributions of axial velocity fluctuations profiles at selected axial locations for the two turbulent cases are shown in Figure 4-24. These locations were near the bubble bottom, at the core of the first large vortex and at the stagnation point on the centerline. The values of the fluctuations in Case 2 are smaller than Case 1. The double peaks of the fluctuations in the radial profiles noticed in Case 1 do not exist in Case 2. This reflects the vigorous oscillation of the bubble bottom in Case 1.

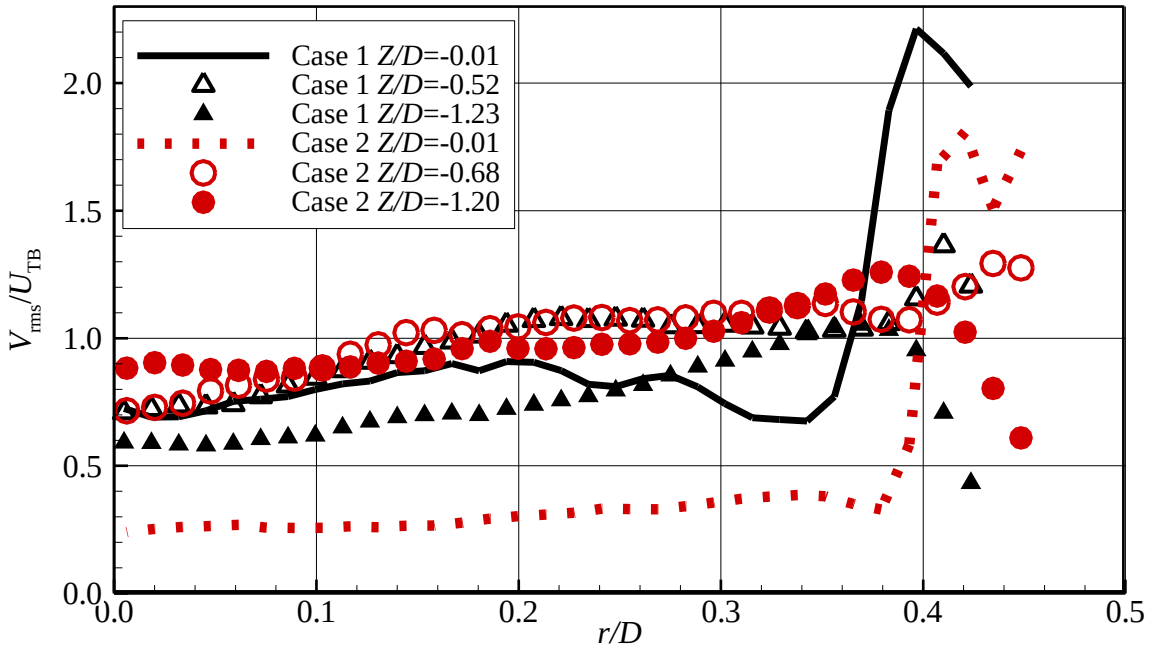

Figure 4-24: Comparison of radial profiles of axial fluctuations at selected axial locations in the wake of Taylor bubble rising in stagnant liquids

5. Taylor Bubbles Rising in Upward Flowing Liquids

Slug flow is often encountered in flowing two-phase, gas-liquid systems. Therefore, in this chapter the measurement of velocity fields in the wake region of single Taylor bubbles is extended to upward flowing liquids. The measurements are performed for different liquid viscosities and at different liquid mass flow rates yielding both laminar and turbulent flow (using liquid superficial velocity). A detailed description of the liquid velocity field in the wake of Taylor bubbles rising in different liquids at different liquid flow rates is provided.

5.1 Wakes of Taylor Bubbles Rising in Upward Flowing Water

5.1.1 Introduction

Table 5-1 shows the three experimental conditions studied for Taylor bubbles rising in upward flowing water. In this table, μ is the liquid viscosity; U_{TB} is the measured bubble velocity, U_L is the mean superficial velocity of the liquid, U_{cl} is the maximum superficial velocity of the liquid, Re_{TB} is the Reynolds number of the bubble($\frac{U_{TB}\rho D}{\mu}$), Re_L is the Reynolds number of the liquid ($\frac{U_L\rho D}{\mu}$) and Re_R is the Reynolds number of the liquid relative to the bubble($\frac{(U_{TB}-U_L)\rho D}{\mu}$).

Table 5-1: Experimental conditions for Taylor bubbles in flowing water

Case #	μ (Pa·s)	U_{TB} (m/s)	Re_{TB} (-)	U_L (m/s)	U_{cl} (m/s)	U_{cl}/U_{TB} (-)	Re_L (-)	Re_R (-)
Case 4	0.00100	0.613	15,400	0.362	0.434	0.708	9,200	6,200
Case 5	0.00100	0.820	20,700	0.541	0.649	0.791	13,600	7,100
Case 6	0.00100	1.020	25,800	0.706	0.847	0.832	17,800	8,000

Before discussing the velocity field, the shape of the bubble bottom will be considered since it can have a strong influence on the velocity field in the near wake. Figure 5-1 shows examples of the bottom surface of Taylor bubbles rising in upward flowing water. These images show the highly irregular instantaneous shape of Taylor bubbles under these conditions (refer to Appendix B for more images). The number of small bubbles shed from the bottom surface of the Taylor bubbles increases with increasing liquid flow rate.

5.1.2 Mean Flow Field in the Near Wake

Since the mean flow is axisymmetric around the tube centreline, the ensemble size was doubled by including both the left and the right halves of the velocity fields in the averaging process. This produced an ensemble size which ranged from 400 to 600. The averaging is performed after the velocity fields are shifted relative the bubble bottom as described in Section 3.7. In the near wake, the bubble rise velocity is used as the reference frame velocity (refer to Section 4.3.2).

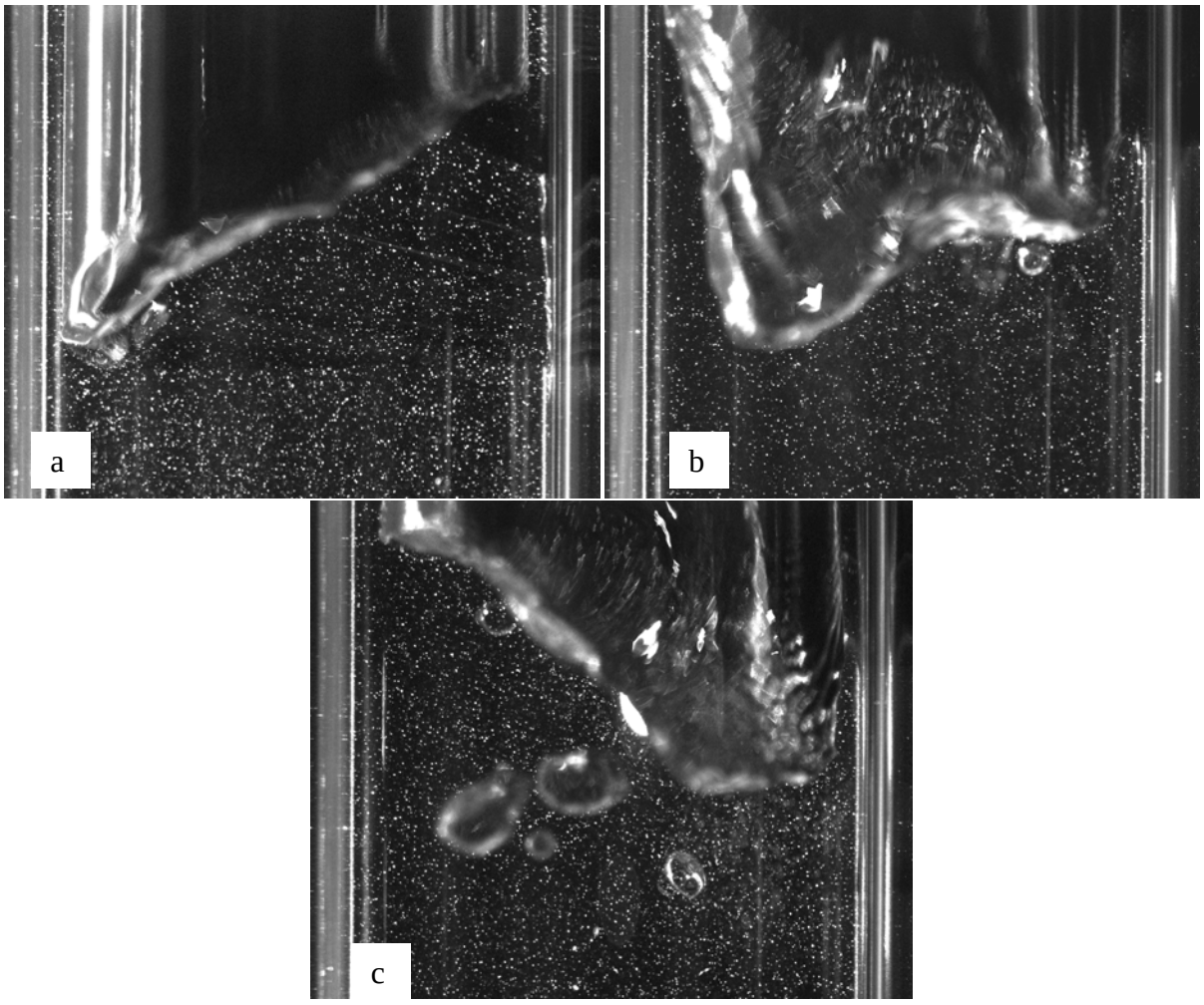

Figure 5-1: Images of the bottom surfaces of Taylor bubbles rising in upward flowing water under the following conditions: (a) Case 4 (Re_{TB} = 15,400, Re_L = 9,200) (b) Case 5 (Re_{TB} = 20,700, Re_L = 13,600) (c): Case 6 (Re_{TB} = 25,800, Re_L = 17,800).

Figures 5-2, 5-3 and 5-4 show velocity vectors and streamlines in a frame of reference moving at the bubble velocity in the near wake of the bubble rising in turbulent upward flowing water (Cases 4, 5 and 6). The mean flow structure in these cases is similar to that of a Taylor bubble rising in stagnant water (Case 1). When the liquid enters the space beneath the bubble a toroidal vortex is formed in the middle of the tube. In this region, the liquid velocity

is downward in the near-wall region and upward along the tube centreline. It can be seen from these figures that the thickness of the falling film increases with increasing axial distance below the bubble and eventually occupies the entire tube cross-section. These wakes are classified as Type III wakes (turbulent) by Campos and Geudes de Carvalho (1988) and Pinto *et al*. (1998).

The vortex centre location was located visually using Tecplot®360 by determining where the axial and radial mean velocities are both zero. The radial location of the vortex centre does not change with increasing liquid flow rate. However, for the flowing liquid the axial location of the vortex core has shifted very slightly toward the bubble's bottom. This can be seen in Table 5-2.

In this frame of reference, a stagnation point occurs on the tube centerline below the bubble which defines the length of the primary recirculation zone. The general observation is that the length of the primary recirculation zone increases with increasing liquid flow rate except for Case 6 where the length of the recirculation zone is essentially unchanged compared to Case 5. A summary of the primary recirculation zone parameters for Cases 4, 5 and 6 is given in Table 5-2.

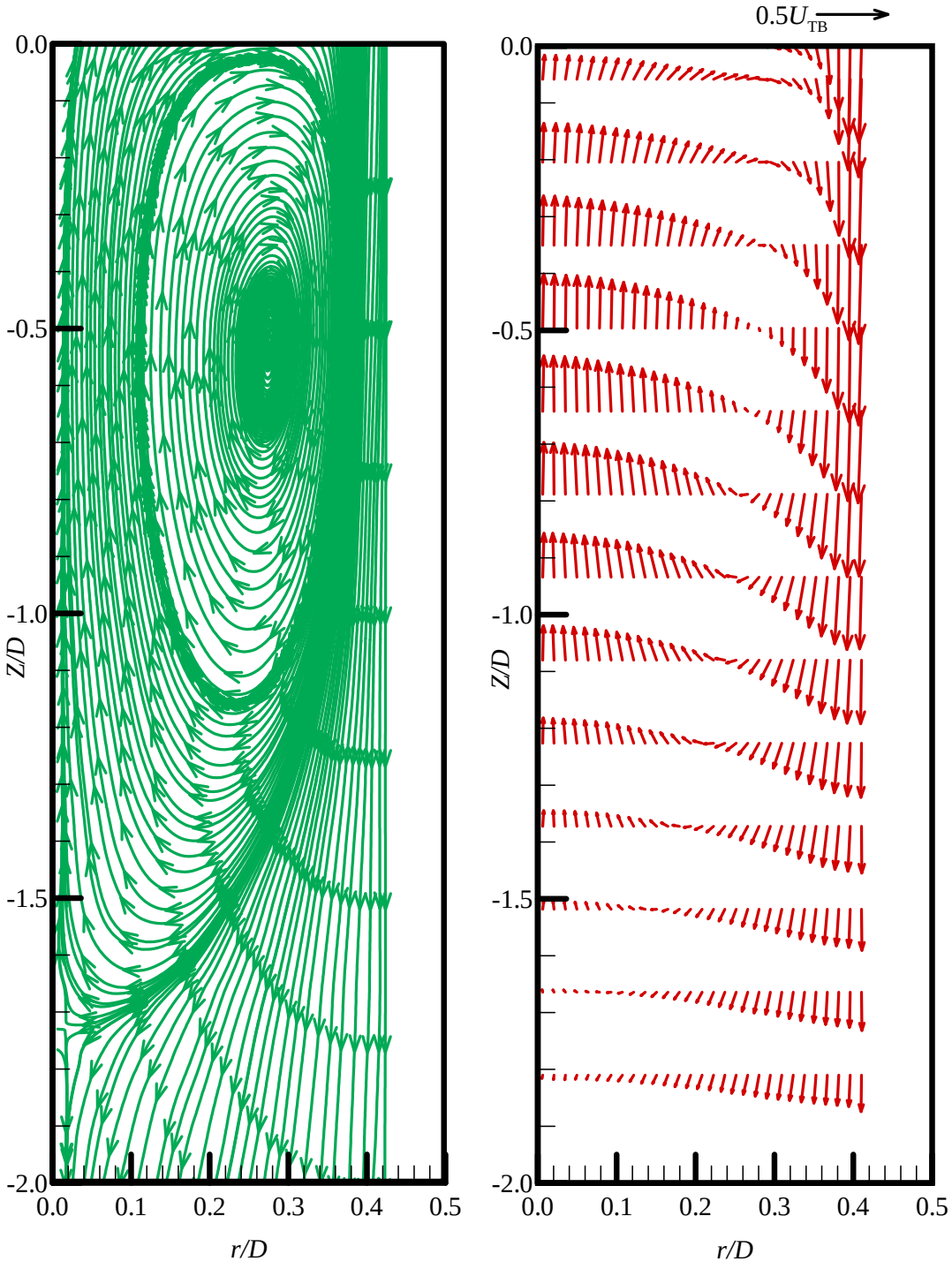

Figure 5-2: The mean velocity vectors and streamlines in the near wake of the Taylor bubble shown in a moving frame of reference (Case 4: Re_{TB} = 15,400, Re_L = 9,200).

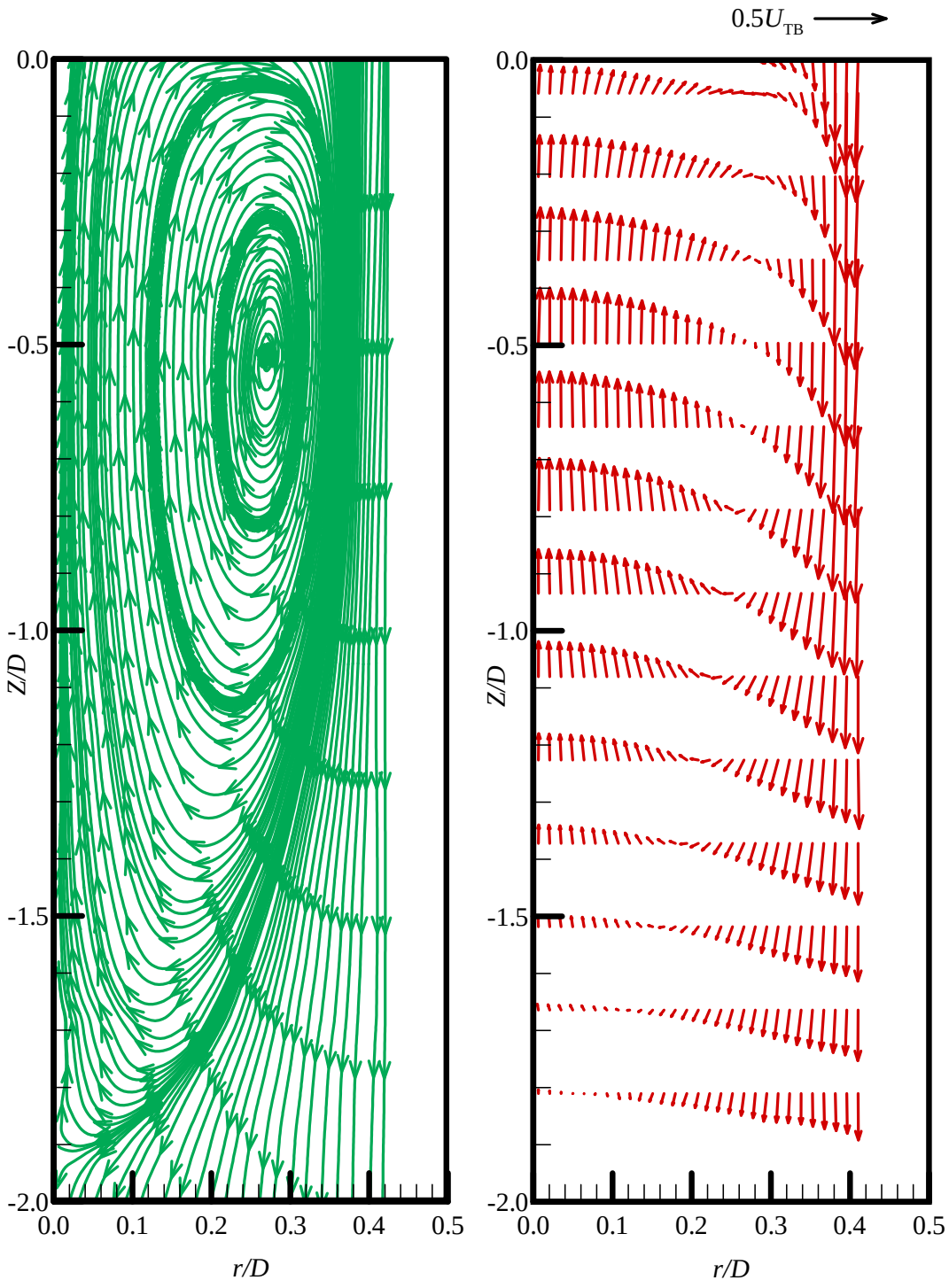

Figure 5-3: The mean velocity vectors and streamlines in the near wake of the Taylor bubble shown in a moving frame of reference (Case 5: Re_{TB} = 20,700, Re_{L} = 13,600).

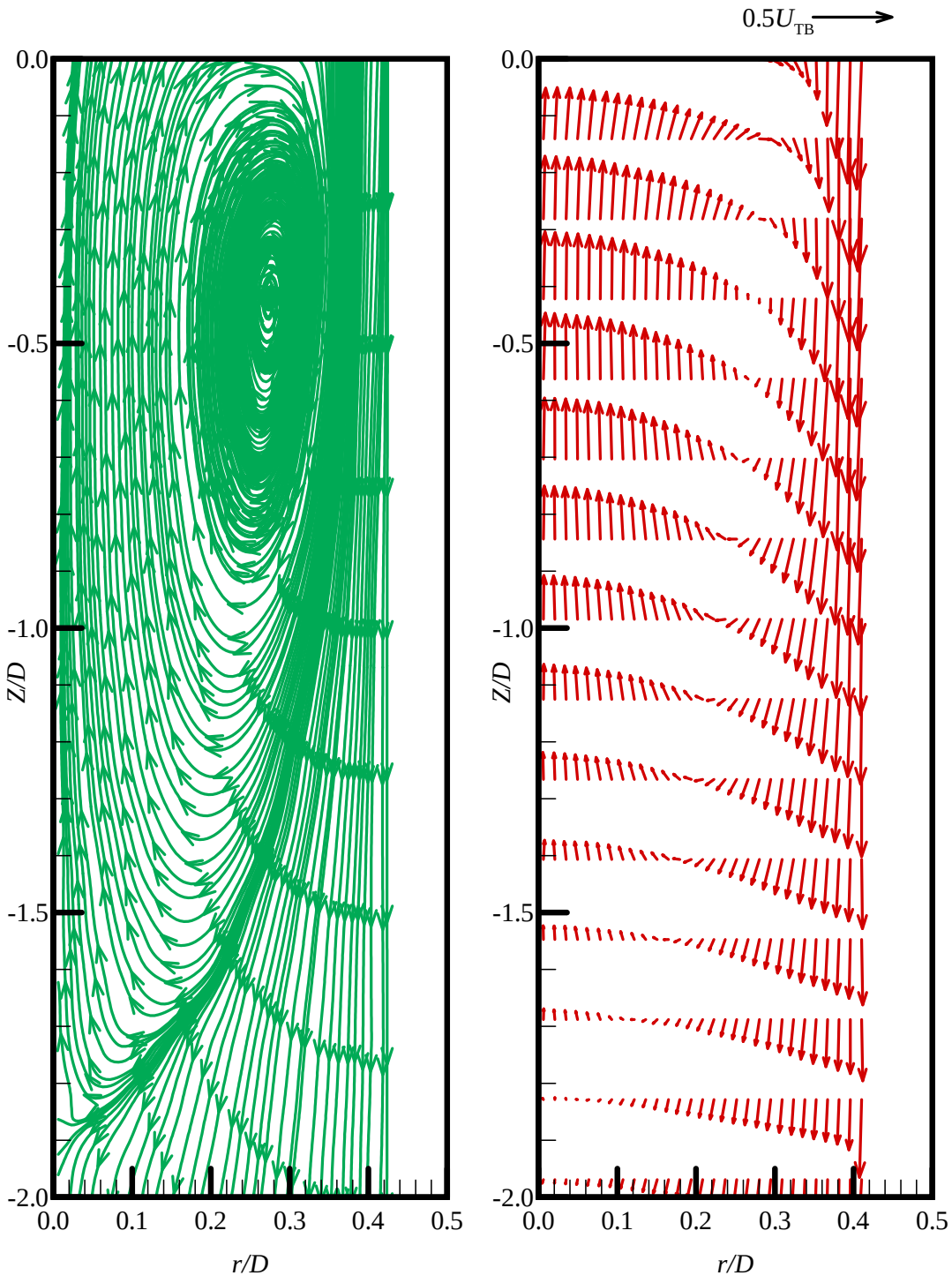

Figure 5-4**:** The mean velocity vectors and streamlines in the near wake of the Taylor bubble shown in a moving frame of reference (Case 6: Re_{TB} = 25,800, Re_L = 17,800).

Table 5-2: Summary of the primary recirculation zone parameters for Cases 4, 5 and 6

Case #	μ (Pa·s)	Re_L (-)	Vortex core location		Wake pattern	Primary recirculation zone length
			Z/D	*r/D*		
Case 4	0.00100	9,185	-0.55	0.27	Turbulent	1.73*D*
Case 5		13,595	-0.52	0.27		1.92*D*
Case 6		17,792	-0.42	0.27		1.90*D*

5.1.3 Axial Velocity Profiles

Figure 5-5 shows the mean axial velocity on the centreline of the pipe as a function of the distance behind the bubble for the three cases of Taylor bubbles rising in upward flowing water. These conditions represent a turbulent background flow (Re_L =9,200, 13,600 and 17,800). As mentioned before, the rise velocity of the Taylor bubbles is used as the scaling velocity in the wake. For all cases, in Figure 5-5, at $Z/D = 0$ the mean axial velocity is higher than the bubble rise velocity (from 1.2 to $1.27U_{TB}$). Then it increases to a maximum (from 1.58 to $1.9U_{TB}$) around $Z/D = -0.5$ to $Z/D = -0.6$ and in all three cases, the axial velocity relative to the Taylor bubble velocity decreases as the flow rate increases. The velocity then decreases to the Taylor bubble velocity at $Z/D = -1.73$ to -1.92 and continues to decrease to the lowest value at around $Z/D = -4$. The velocity then starts to increase to re-establish fully-developed turbulent flow in a pipe around $Z/D = -10$. In Figure 5-5, the values of the centerline velocity for fully-developed turbulent flow for the three cases are shown as horizontal lines. In all three cases, this decrease and increase of the velocity in the region between $-2 < Z/D < -6$ implies that an additional weaker vortex with an opposite sense of rotation exists behind the main primary recirculation zone.

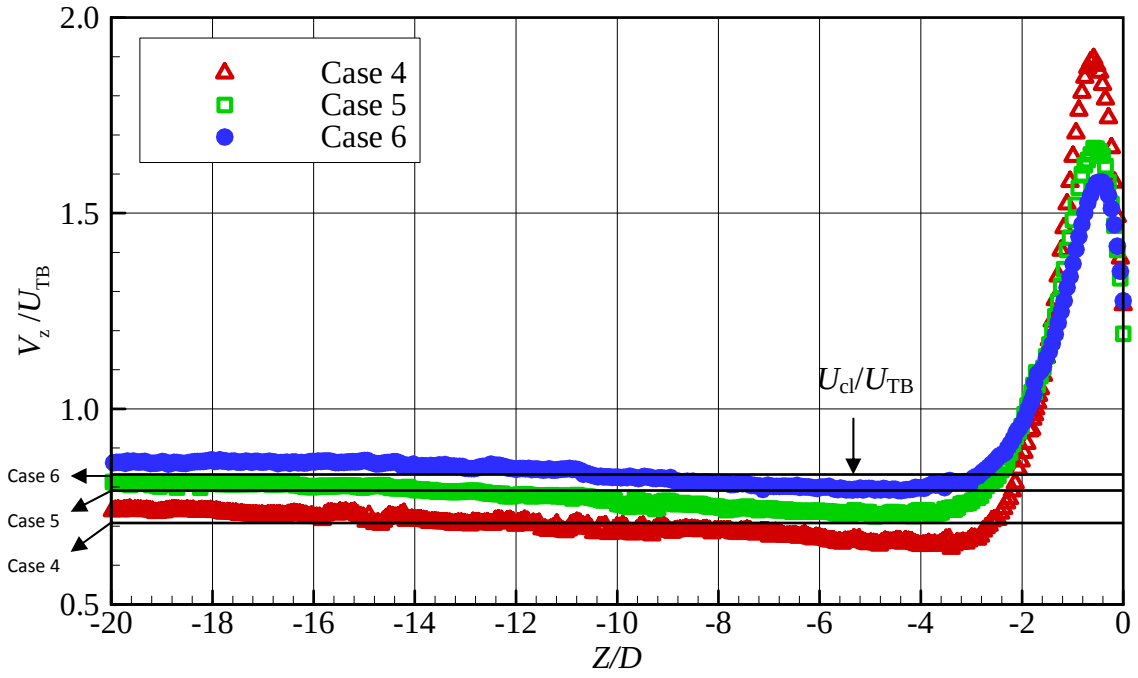

Figure 5-5: Comparison of the axial velocity at the centreline of the tube in the wake of Taylor bubbles rising in upward moving water shown in a fixed frame of reference (Cases 4, 5 and 6)

Radial profiles of the axial velocity at various locations in the wake of the bubbles rising in upward flowing water in a fixed frame of reference are presented in Figures 5-6 to 5-8. These axial locations are selected at the bubble bottom Z = -0.01D, through the preliminary recirculation zone centre, at Z = -1D, at the stagnation point on the centreline, Z= -4D and Z=-12D. In these figures, immediately behind the bubble (Z = -0.01D) the magnitude of the axial velocity in the central region of the tube is higher than the terminal velocity of the bubble. In the primary recirculation zone, at the centre of the tube the liquid moves upward with a velocity larger than the terminal velocity of the bubble. A wall jet with downward velocities is clearly seen in these figures. The velocity of the wall jet reduces and the jet spreads in the liquid behind the bubble. In a stationary frame of reference and upward flowing liquid, negative axial velocities are an effect of the bubble passing and are produced

by the falling film overcoming the upward velocity of the flow. In the velocity profiles for Case 4 (Figure 5-6), the maximum downward velocity was $0.6U_{TB}$ and the maximum upward velocity was $1.9U_{TB}$. In the velocity profiles for Case 5 (Figure 5-7), the maximum downward velocity was $0.3U_{TB}$ and the maximum upward velocity was $1.67U_{TB}$. In the velocity profiles for Case 6 (Figure 5-8), the maximum downward velocity was $0.2U_{TB}$ and the maximum upward velocity was $1.58U_{TB}$. In general, the maximum upward velocity relative to the Taylor bubble velocity decreases as the flow rate of the upward flowing liquid increases. The solid lines in these figures represent the upward velocity of the water flowing in the tube without the presence of Taylor bubbles. The experimental turbulent profile and the estimate provided by the power law are almost identical (within 4% in the region $r/D < 0.3$). However, notable discrepancies distinguish the two curves at $r/D > 0.4$. This may be due to the optical distortion of tube curvature. The fully-developed turbulent velocity profile of the water in the tube starts to become re-established as early as $Z/D = -4$. This is a result of the strong mixing in the turbulent background liquid flow.

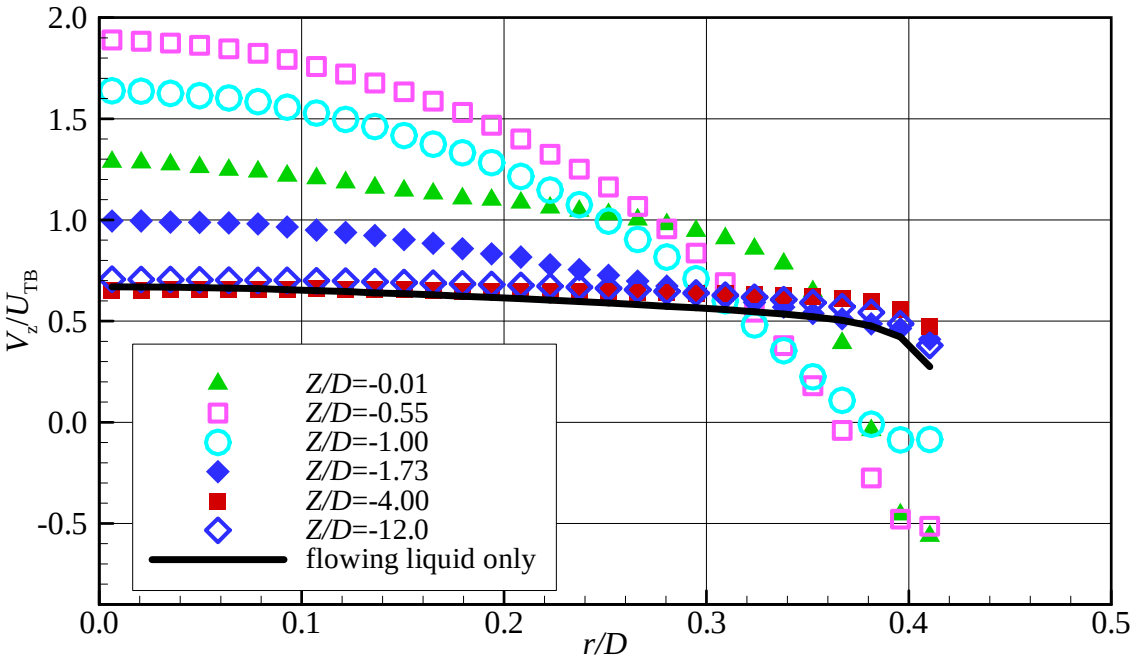

Figure 5-6: Radial profiles of axial velocity at various axial positions in the wake of a Taylor bubble rising in turbulent flowing water (Case 4: Re_{TB} = 15,400, Re_L = 9,200)

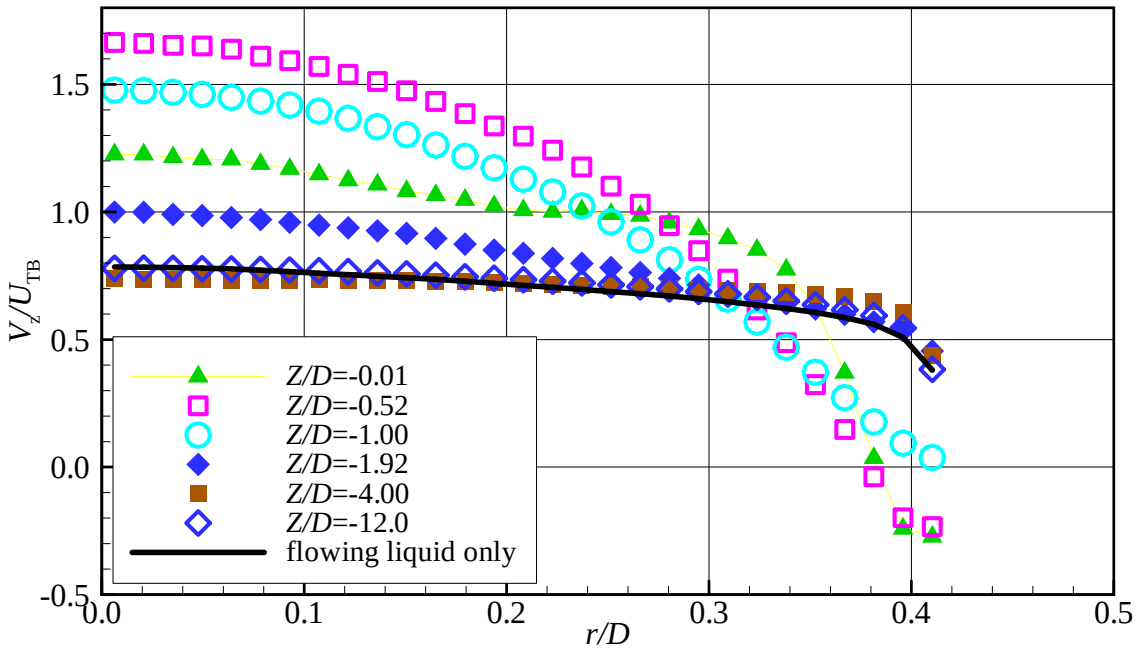

Figure 5-7: Radial profiles of axial velocity at various axial positions in the wake of a Taylor bubble rising in turbulent flowing water (Case 5: Re_{TB} = 20,700, Re_L = 13,600)

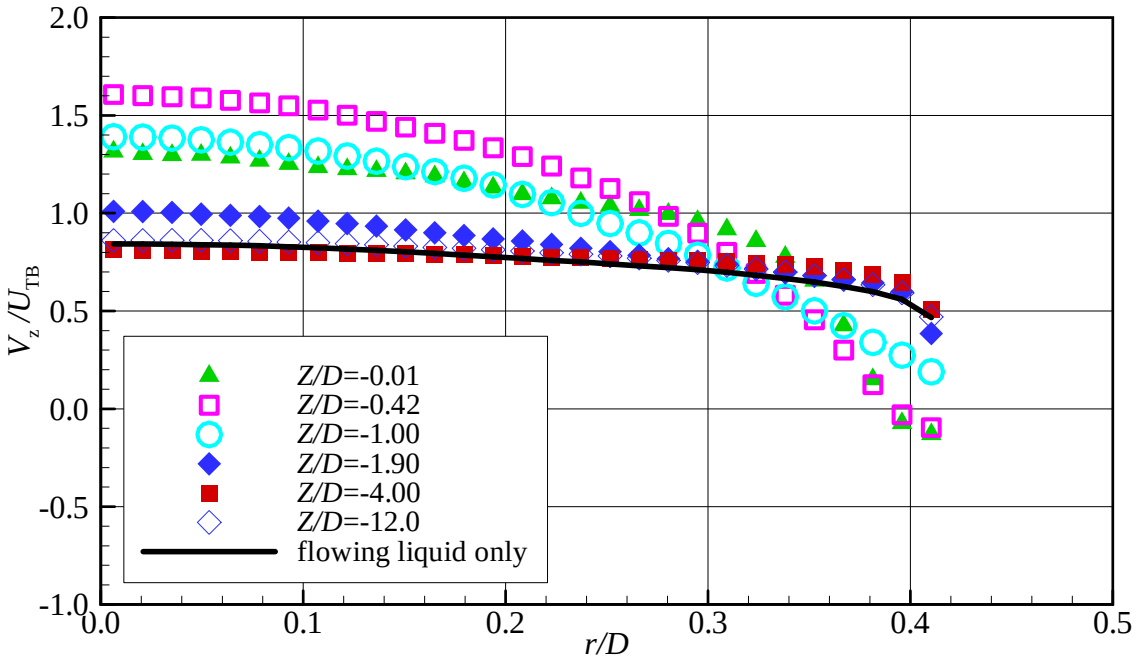

Figure 5-8: Radial profiles of axial velocity at various axial positions in the wake of a Taylor bubble rising in turbulent flowing water (Case 6: Re_{TB} = 25,800, Re_L = 17,800)

5.1.4 Radial Velocity Profiles

Radial profiles of the radial velocity at different locations behind the bubble rising in upward flowing liquid for the three cases are illustrated in Figures 5-9 to 5-11. The magnitude of the radial velocity is much lower than the axial velocity. The sign and behavior of the radial velocity in these figures are consistent with the vortex pattern presented in Figures 5-2 to 5-4. The largest radial velocities occur midway between the wall and the tube centreline. The highest negative value of the velocity (0.08-0.12U_{TB}) is located at about 1D from the bubble bottom. The highest positive value (0.09 - 0.1 U_{TB}) is located at about 0.01D from the bottom. At Z/D < -4 the radial velocity component essentially vanishes. It is clear that the upward liquid velocity has little effect on the radial velocity.

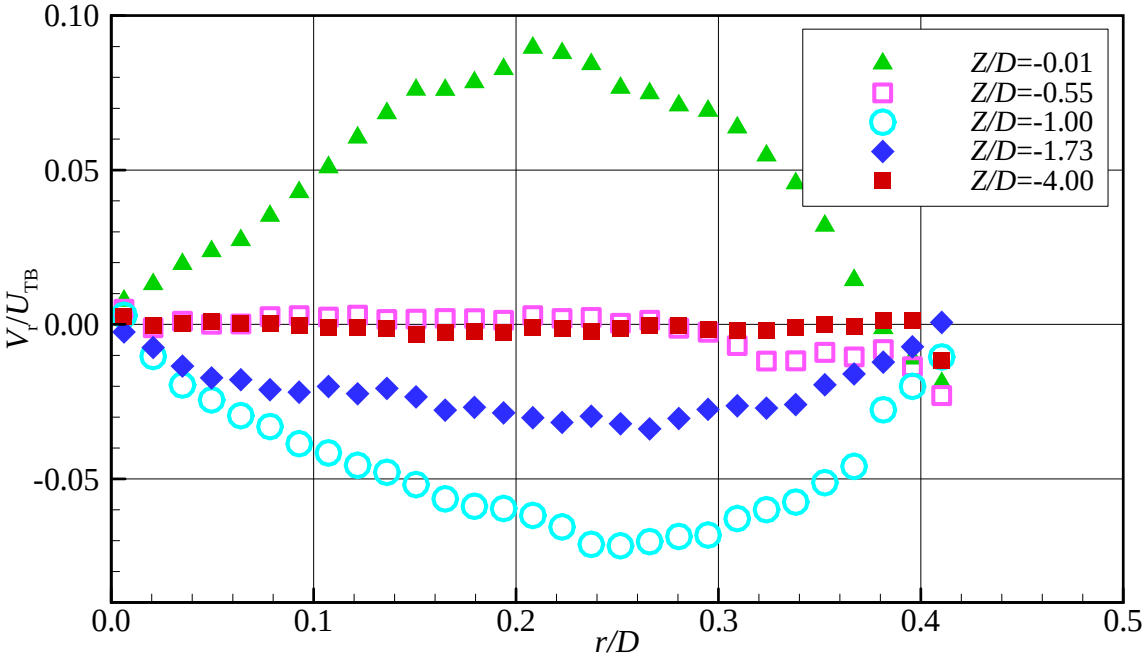

Figure 5-9: Radial profiles of radial velocity at various axial positions in the wake of a Taylor bubble rising in turbulent flowing water (Case 4: Re_{TB} = 15,400, Re_L = 9,200)

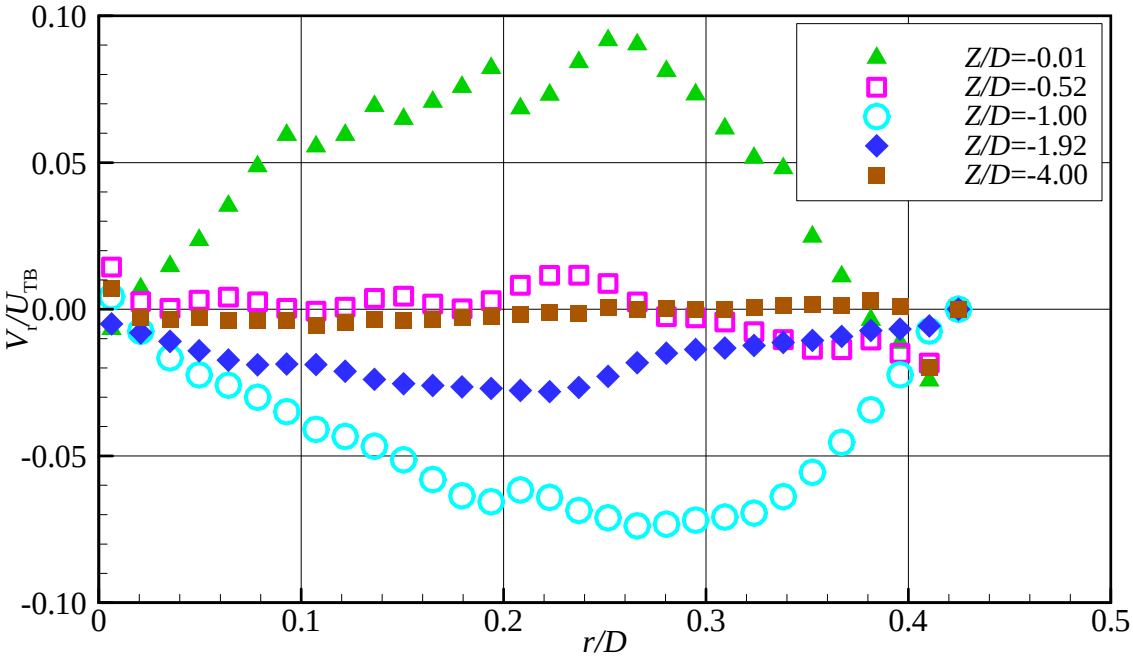

Figure 5-10: Radial profiles of radial velocity at various axial positions in the wake of a Taylor bubble rising in turbulent flowing water (Case 5: Re_{TB} = 20,700, Re_L = 13,600)

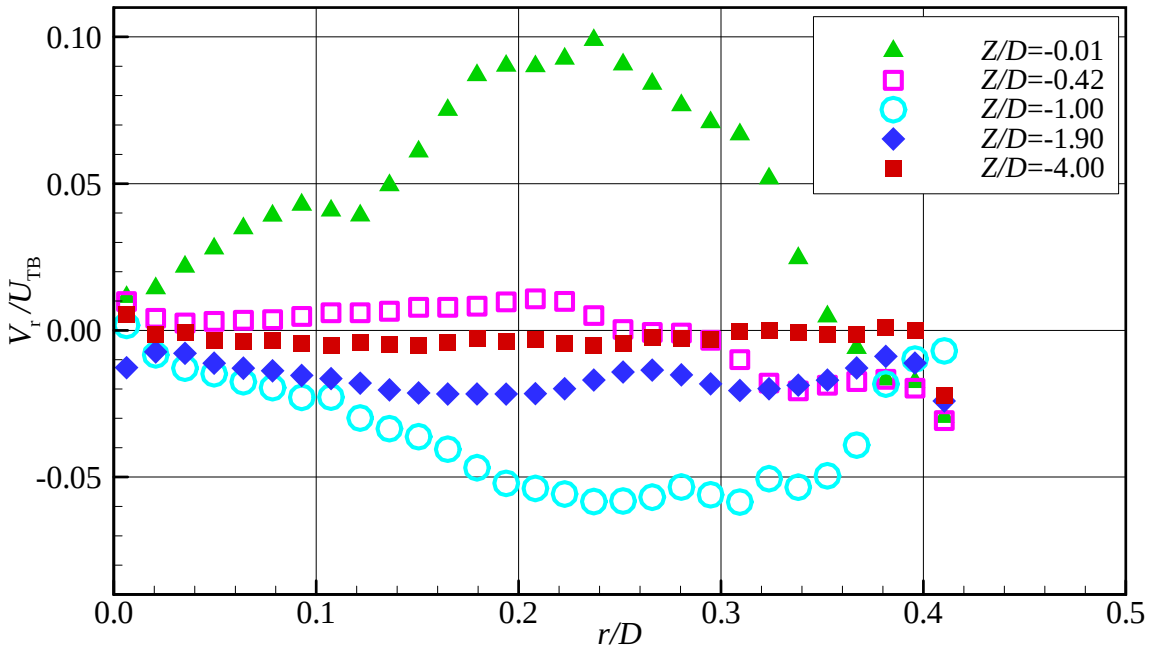

Figure 5-11: Radial profiles of radial velocity at various axial positions in the wake of a Taylor bubble rising in turbulent flowing water (Case 6: Re_{TB} = 25,800, Re_L = 17,800)

5.1.5 Axial Velocity Fluctuations Profiles

Axial velocity fluctuations for the three cases are illustrated in Figures 5-12 to 5-14. For all three cases, the highest fluctuations are located immediately behind the bubble and in the near wake region (*Z/D* = -0.01 to *Z/D* = -2). Due to spreading of the annular jet, the maximum value of the fluctuations is attained in the region where the annular jet enters the wake at around *r/D* = 0.38. The peak of the fluctuations close to the wall flattens as the distance increases from the bubble bottom. For the three cases, the radial profiles of axial velocity fluctuations match the fully-developed turbulent flowing water (solid lines in the figures) in the tube at *Z/D* = -12. Solid lines are taken from the experimental measurements of the water flowing without a Taylor bubble present in the flow. The turbulence intensity, relative to the bubble velocity, decreases as the flow rate increases.

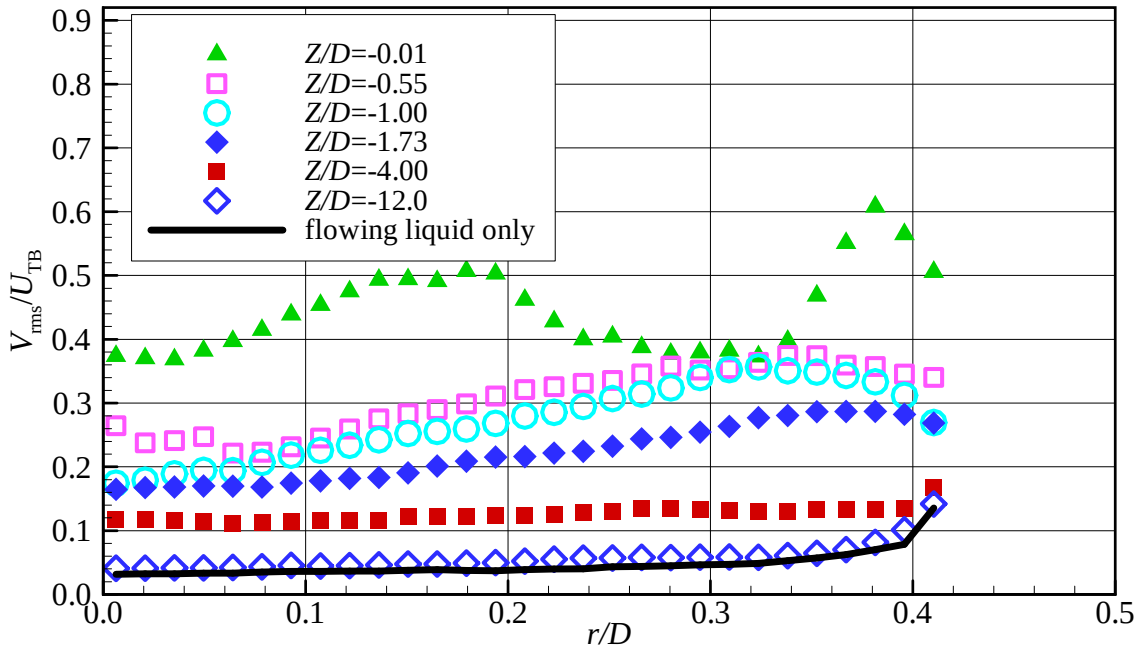

Figure 5-12: Radial profiles of axial turbulence intensity at various axial positions in the wake of a Taylor bubble rising in turbulent flowing water (Case 4: Re_{TB} = 15,400, Re_L = 9,200)

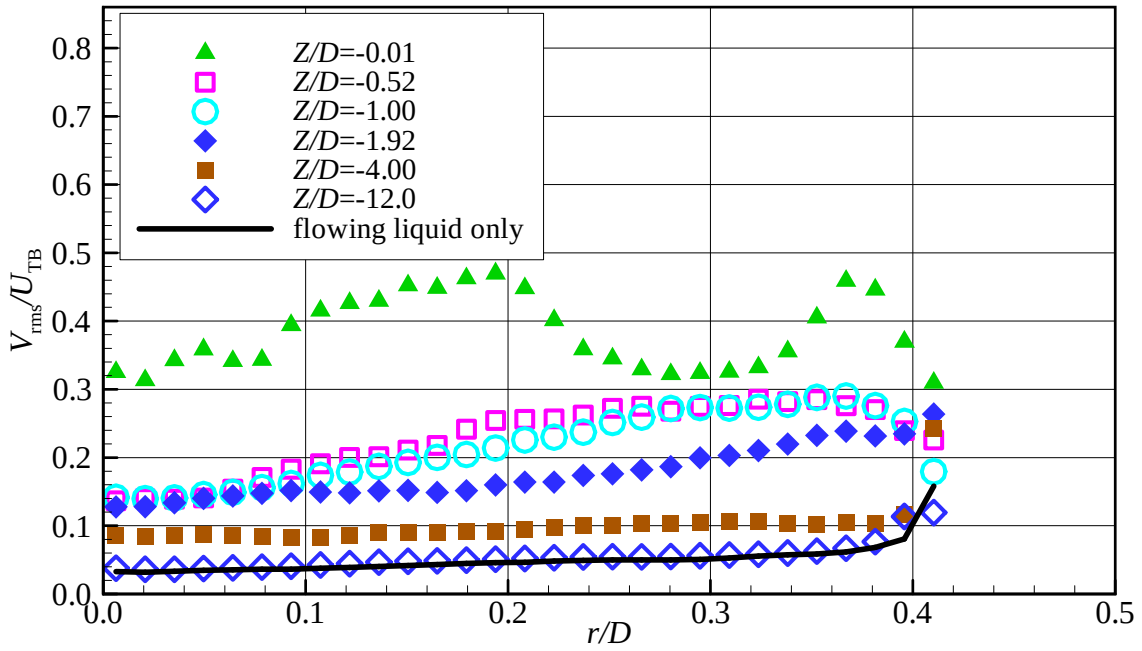

Figure 5-13: Radial profiles of axial turbulence intensity at various axial positions in the wake of a Taylor bubble rising in turbulent flowing water Case 5: Re_{TB} = 20,700, Re_L = 13,600)

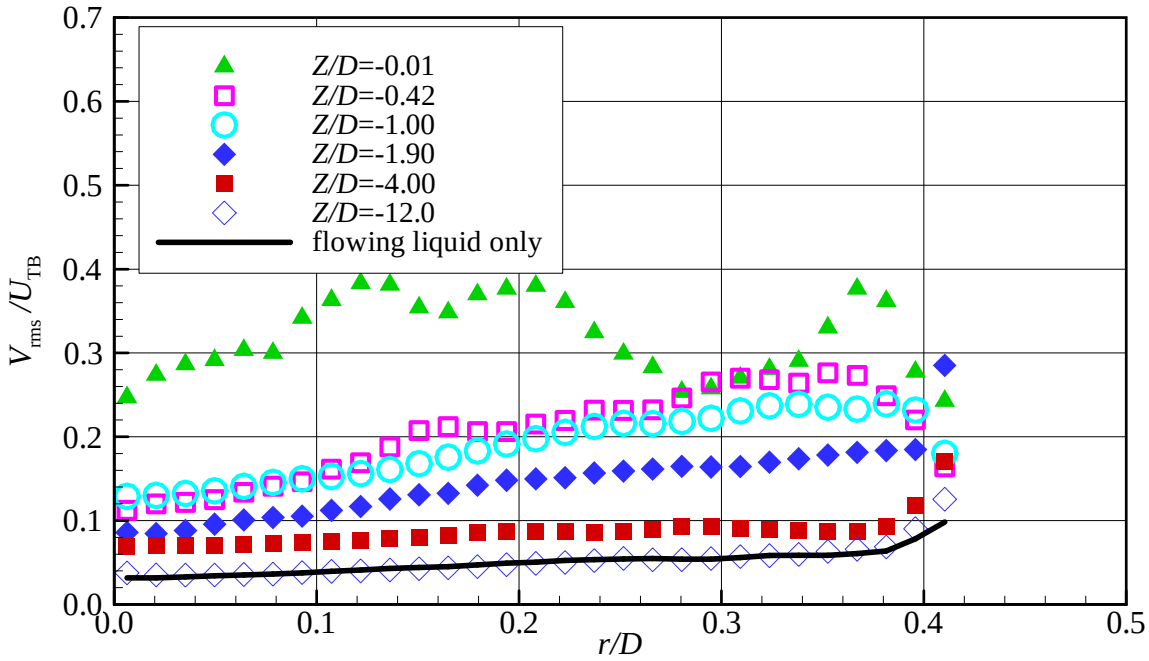

Figure 5-14: Radial profiles of axial turbulence intensity at various axial positions in the wake of a Taylor bubble rising in turbulent flowing water (Case 6: Re_{TB} = 25,800, Re_L = 17,800)

5.2 Wakes of Taylor Bubbles Rising in an Upward Flowing Mixture of Water and Glycerol (μ = 0.00500 Pa·S)

5.2.1 Introduction

Table 5-3 shows the two experimental conditions studied for Taylor bubbles rising in a mixture of water and glycerol. The liquid flow is laminar in Case 7 and turbulent in Case 8. Even though the background flows are in different regimes, the wake regime in the two cases is the same. This will be discussed further in the following sections.

Table 5-3: Experimental conditions for Taylor bubbles rising in a flowing water-glycerol mixture (μ = 0.0050 Pa·s)

Case #	μ (Pa·s)	U_{TB} (m/s)	Re_{TB} (-)	U_L (m/s)	U_{cl} (m/s)	U_{cl}/U_{TB} (-)	Re_L (-)	Re_R (-)
Case 7	0.00500	0.661	3,800	0.253	0.506	0.765	1,500	2,300
Case 8	0.00500	0.979	5,700	0.684	0.820	0.837	3,900	1,800

It was observed that the nose is axisymmetric for both the stagnant and laminar cases (Case 2 and Case 7). However, for turbulent upward flowing liquid (Case 8), the instantaneous shape of the bubble nose becomes asymmetric. This asymmetry is not biased toward one side of the tube and the mean shape is axisymmetric. This will be discussed further in Section 5.6.

Figure 5-15 shows examples of the bottom surface of Taylor bubbles rising in this upward flowing water-glycerol mixture (refer to Appendix B for more images). In both cases, the images show the irregular instantaneous shape of the Taylor bubbles. This is in contrast to the bottom shape of a bubble rising in the same mixture under stagnant conditions (Case 2) where the bottom edge of the bubble is much more rounded and the oscillation of the bubble bottom is much weaker. The number of small bubbles being shed from the bottom of the Taylor bubbles increases with increasing liquid flow rate.

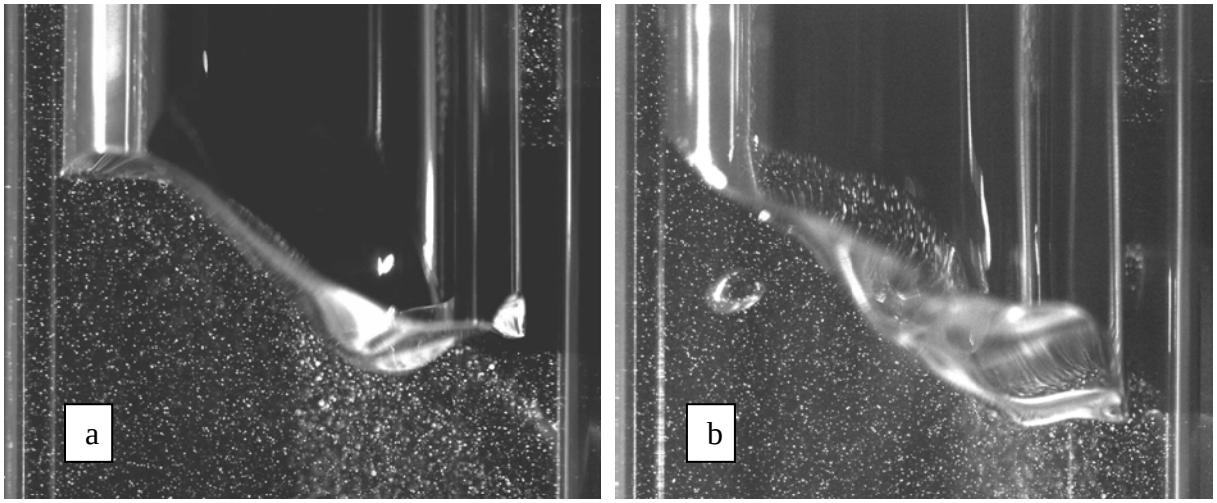

Figure 5-15: Bottom surfaces of Taylor bubbles rising in an upward flowing mixture of water and glycerol: (a) Case 7 (Re_{TB} = 3,800 & Re_L= 1,500) (b) Case 8 (Re_{TB} = 5,700 & Re_L =3,900)

5.2.2 Mean Flow Field in the Near Wake.

The velocity field results presented for these cases were obtained from averaging the left and the right halves of the velocity field thus doubling the ensemble size to 400. Figures 5-16 and 5-17 show velocity vectors and streamlines in a frame of reference moving at the bubble velocity in the near wake of a bubble rising in a laminar upward flowing liquid (Case 7) and a turbulent upward flowing liquid (Case 8). The mean flow structure in these cases is similar to that of the cases previously discussed in this chapter. A summary of the main vortex characteristics is given in Table 5-4. The flow in the wake is turbulent in both cases and the wake is classified as Type III according to Campos and Geudes de Carvalho (1988) and Pinto *et al*. (1998). The quiet zone region is not seen in Figure 5-16 as it was in Case 2 (stagnant liquid). This may due to the fact that the oscillation of the tail has increased compared to the stagnant case.

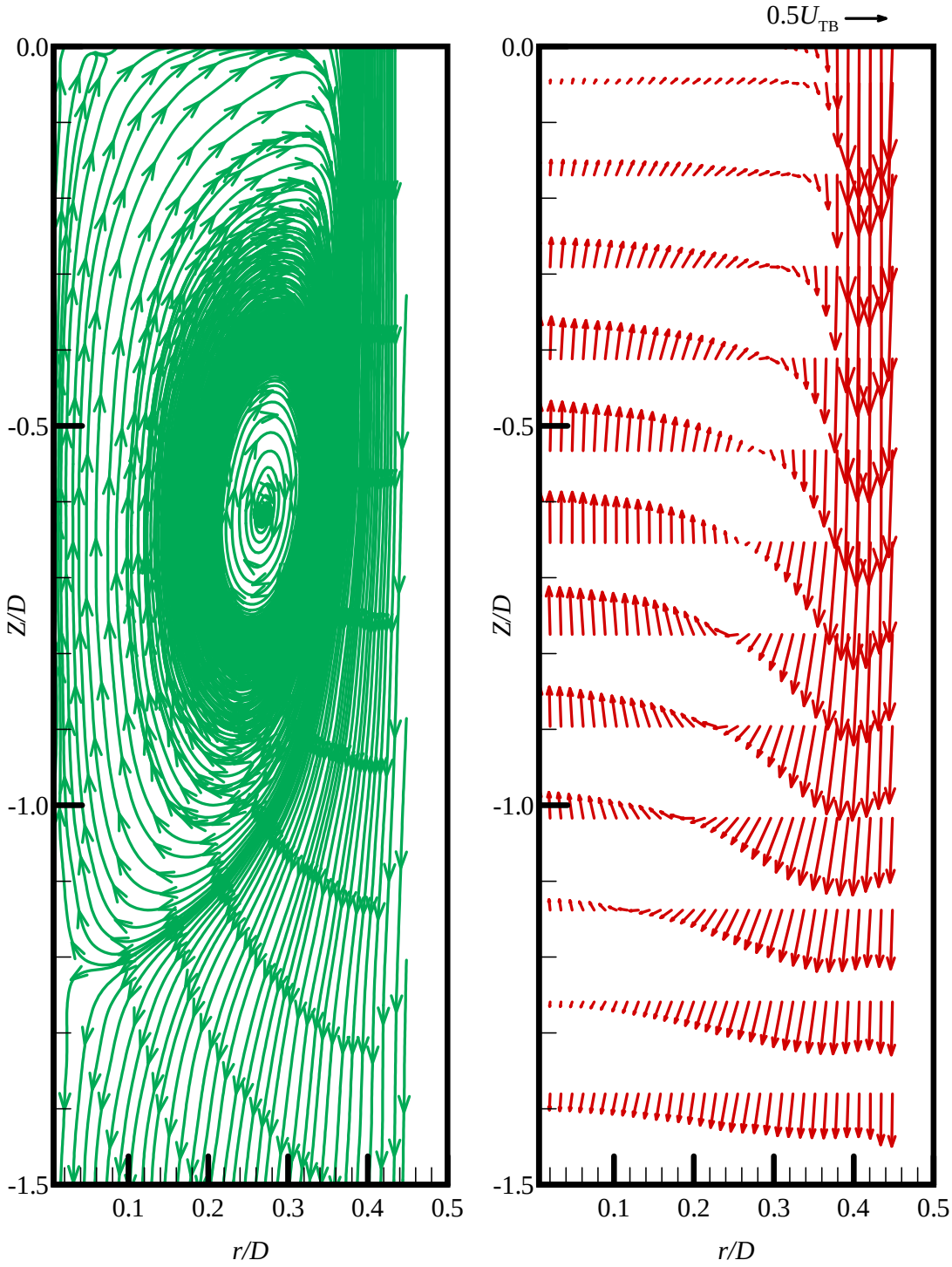

Figure 5-16: Mean velocity vectors and streamlines in the near wake of the Taylor bubble shown in a moving frame of reference (Case 7: Re_{TB} = 3,800, Re_L = 1,500)

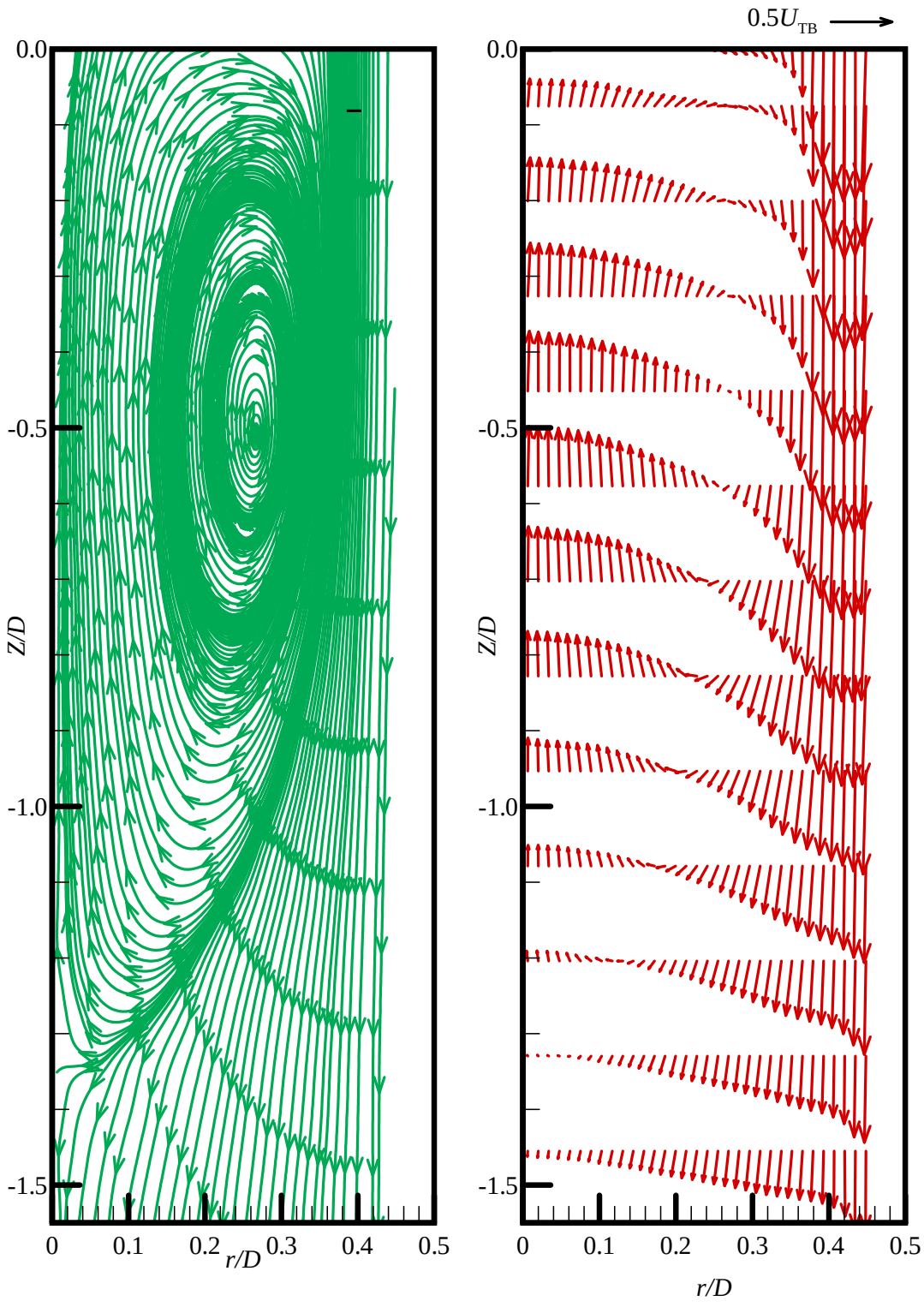

Figure 5-17: Mean velocity vectors and streamlines in the near wake of the Taylor bubble shown in a moving frame of reference (Case 8: Re_{TB} = 5,700, Re_L = 3,900)

Table 5-4: Summary of the primary recirculation zone parameters for Cases 7 and 8

Case #	μ (Pa·s)	Re_L (-)	Vortex core location		Wake pattern	Primary recirculation zone length
			Z/D	*r/D*		
Case 7	0.00500	1,500	-0.62	0.27	Turbulent	1.22*D*
Case 8		3,900	-0.51	0.27		1.34*D*

5.2.3 Axial Velocity Profiles

Figure 5-18 illustrates the axial velocity at the tube centreline as a function of distance from the bubble bottom. For Case 7, the mean axial velocity increases from the bubble rise velocity at the tail to reach the maximum at *Z/D* = -0.6. The maximum upward velocity is around 1.7 times the Taylor bubble rise velocity. Then the velocity decreases to the Taylor bubble velocity at *Z/D*= -1.22 and continues to decrease until *Z/D*= -2.6 (V_Z= 0.37U_{TB}). Then it starts to increase slowly to establish fully-developed laminar flow. According to Table 5-2, the value of V_Z/U_{TB} is 0.765 for a fully-developed laminar flow. This value is not achieved even at the end of the measurements domain. For Case 8, the mean axial velocity gradually increases from 1.2U_{TB} at the tail to reach the maximum of 1.5U_{TB} at *Z/D* = -0.5. It then decreases to the Taylor bubble velocity at *Z/D* = -1.34 and continues to decrease slowly until *Z/D* = -3 (V_Z= 0.72U_{TB}). Then it starts to increase to establish the fully-developed turbulent (V_Z = 0.838U_{TB}) flow in a pipe at around *Z* =-12*D*.

Figure 5-18 shows no similarity (curves do not collapse together) on the centreline velocity distribution for the two cases presented. This may be due to the scaling velocity chosen. In the near wake, using the falling film average velocity as a scaling velocity seems like a more

rational choice of scaling velocity because it directly affects the wake. However, it is very difficult to measure the falling film velocity and the film thickness with this experimental set up. Therefore, using the Taylor bubble velocity as the scaling velocity seems very natural since it is easy to measure. However, in the far wake, it may be more useful to use the liquid superficial velocity as a scaling velocity. For example, in the case of a laminar background flow, the value of the axial velocity at the centreline is $V_Z = 2U_L$. In the case of turbulent background liquid flow, the axial velocity is $V_Z = 1.2U_L$. As in the water cases, the decrease and increase of the velocity in the region between $-2 < Z/D < -6$ implies that an additional weaker vortex with an opposite sense of rotation exists behind the main primary recirculation zone.

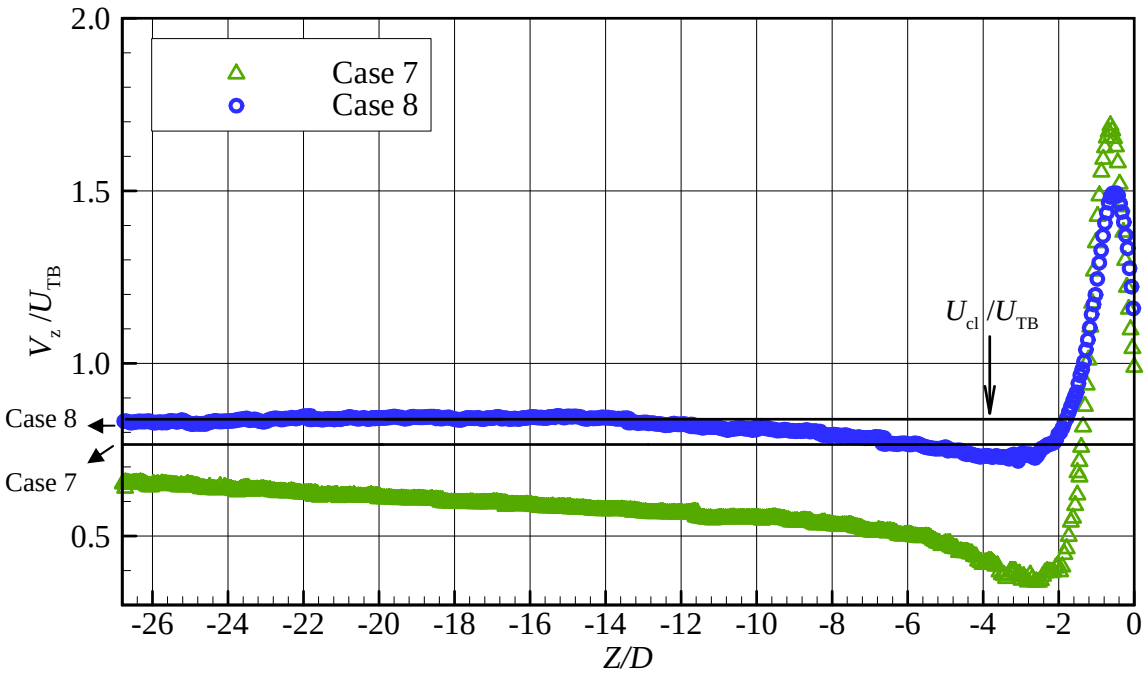

Figure 5-18: Comparison of the axial velocity at the centreline of the tube in the near wake of Taylor bubbles rising in an upward moving liquid (Case 7 and Case 8)

For Cases 7 and 8, radial profiles of the axial velocity at several locations behind the bubble are shown in Figures 5-19 and 5-20. In the near wake, each radial velocity profile has local maxima and minima. The minima is in the jet region and the maxima is at the tube centreline. For Case 7, immediately behind the bubble (Z = -0.01D), the axial velocity profile in the central region is flat and the value of the velocity equals the terminal velocity of the bubble. The maximum upward velocity is along the tube centreline at Z/D= -0.6. The maximum downward velocity is $-U_{TB}$ for Z/D= -0.01 at the entry of the film to the wake. In Case 7, both the upward velocity and the downward velocity relative to the bubble rise velocity are less than for the stagnant case (Case 2). In Figure 5-19, in the far wake (Z/D < -5) of the Taylor bubble, the fully-developed laminar velocity profile is restored very slowly (starting at around Z = -4D). At Z = -28, the difference of this velocity profile from the fully-developed parabolic shape of laminar flow indicates that the flow is not fully-developed laminar flow in the whole measurement domain. For Case 8, at Z = -0.01D, the axial velocity profile in the central region is not as flat as Case 7, and the velocity is slightly greater than the terminal velocity of the bubble. The maximum upward velocity is along the tube centreline at Z/D= -0.5. The strongest downward velocity is $-0.6U_{TB}$ at Z/D= -0.01 as expected. In the far wake of the Taylor bubble (Z/D < -5), it is clear from Figure 5-20 that the fully-developed turbulent velocity profile is restored faster than for the laminar case (Case 7). In these two cases, both the upward velocity and the jet velocity relative to the bubble rise velocity decrease with increasing liquid flow rate. This is due to the effect of the upward flowing liquid. As the upward flowing liquid velocity increases the annular film liquid velocity decreases.

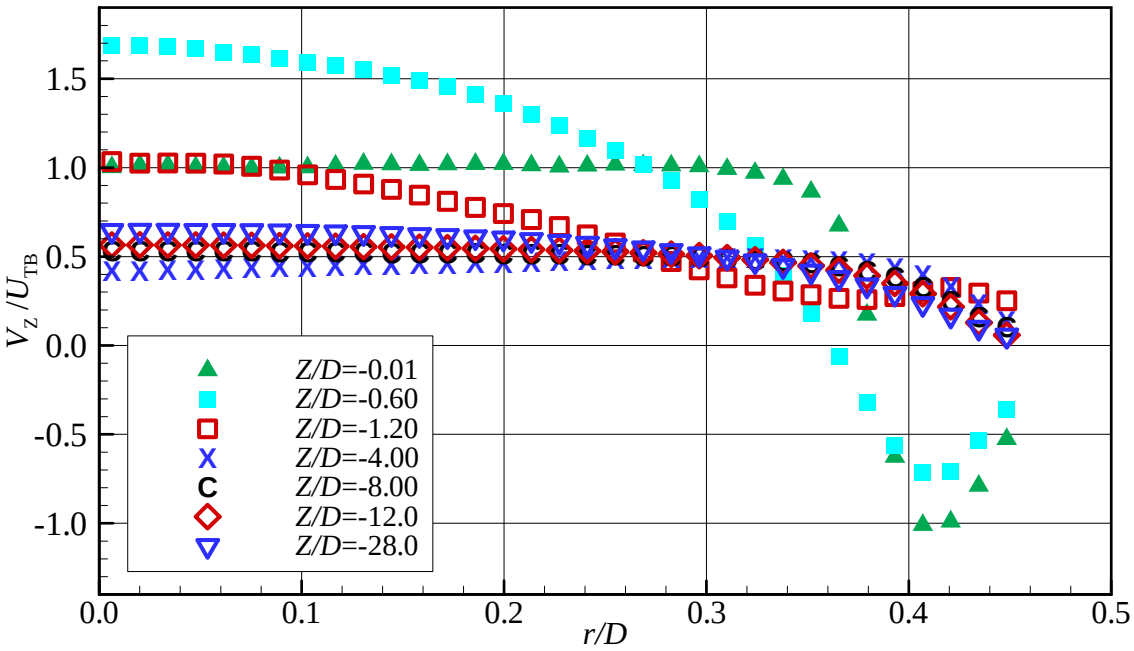

Figure 5-19: Radial profiles of axial velocity at various axial positions in the wake of a Taylor bubble rising in laminar flowing liquid (Case 7: Re_{TB} = 3,800, Re_L = 1,500)

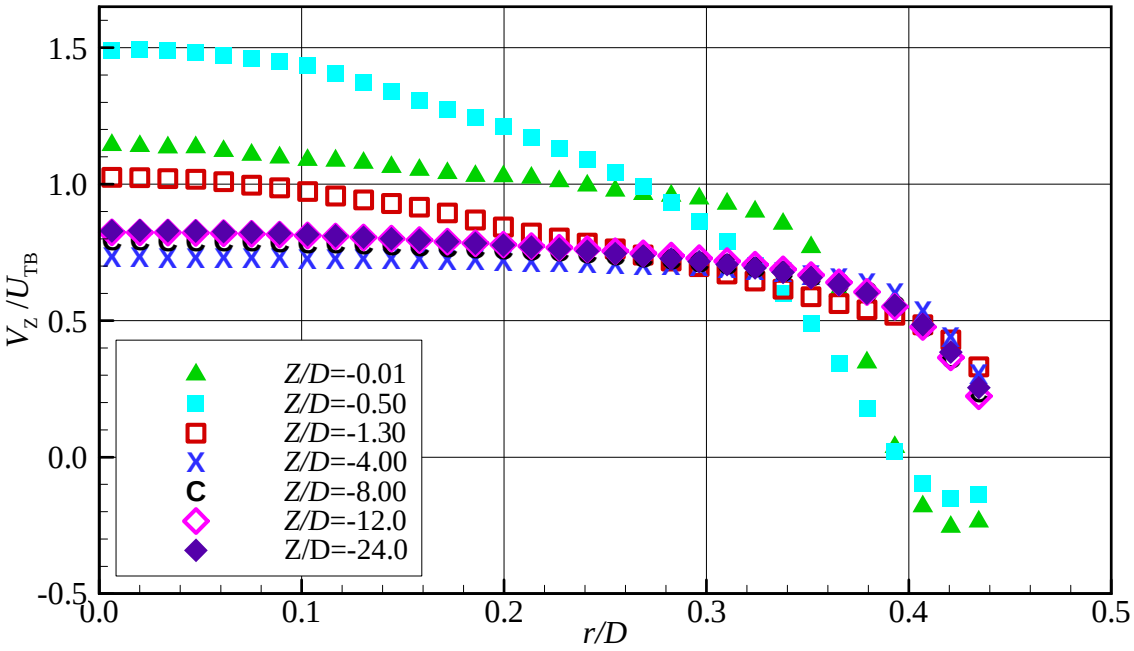

Figure 5-20: Radial profiles of axial velocity at various axial positions in the wake of a Taylor bubble rising in turbulent flowing liquid (Case 8: Re_{TB} = 5,700, Re_L = 3,900)

5.2.4 Radial Velocity Profiles

For Cases 7 and 8, radial profiles of the radial velocity at different locations behind the bubble are illustrated in Figures 5-21 and 5-22. A comparison with Figures 5-19 and 5-20 reveals that the radial velocity is much smaller than the axial velocity. The direction and the behavior of the radial velocity are similar to that of the stagnant case. However, the magnitude of the radial velocity relative to the bubble velocity is less than that of the stagnant case (Case 2). At $Z/D < -2$ the radial velocity component essentially vanishes. This is an indication that the second vortex seen in the stagnant case is much weaker in the flowing case.

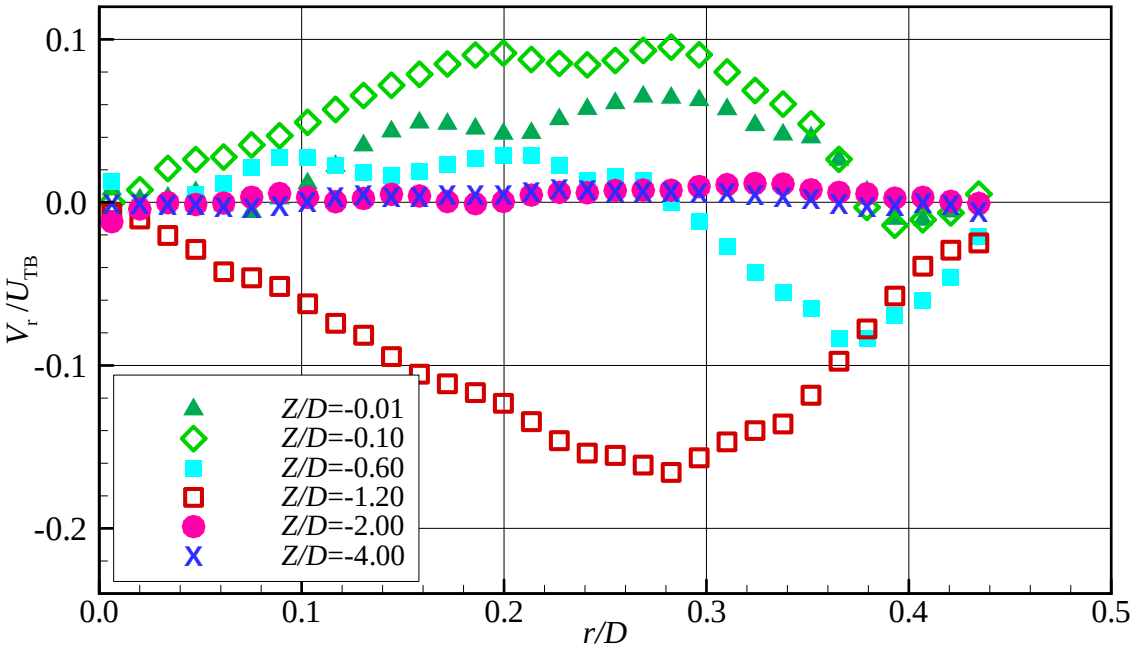

Figure 5-21: Radial profiles of radial velocity at various axial positions in the wake of a Taylor bubble rising in laminar flowing liquid (Case 7: Re_{TB} = 3,800, Re_L = 1,500)

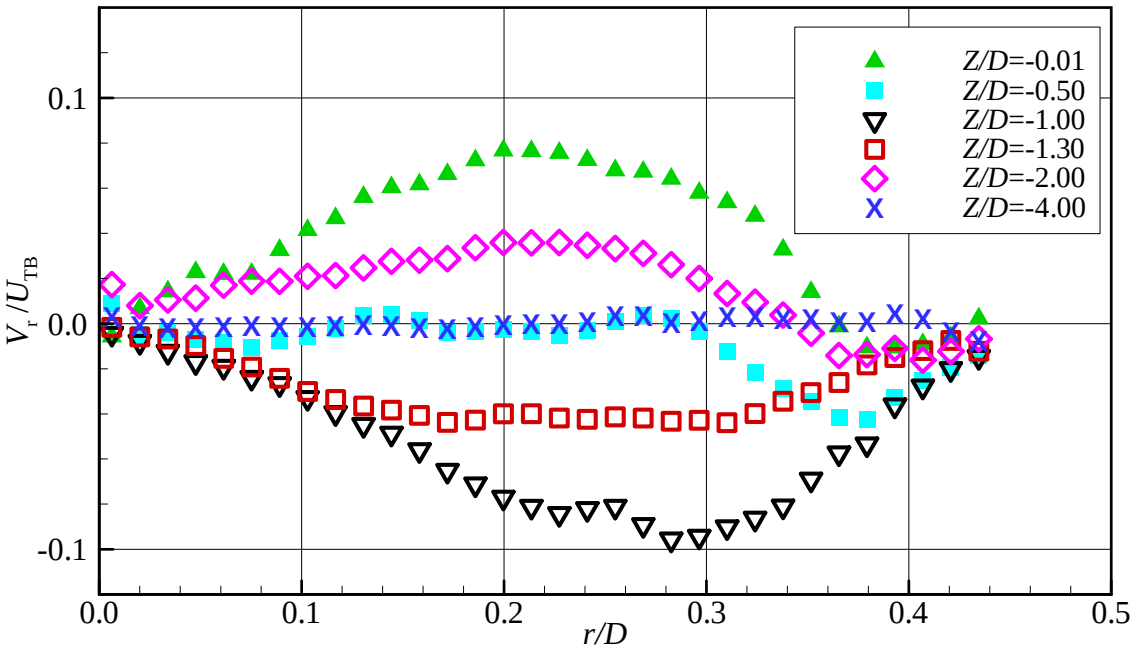

Figure 5-22: Radial profiles of radial velocity at various axial positions in the wake of a Taylor bubble rising in a turbulent flowing liquid (Case 8: Re_{TB} = 5,700, Re_L = 3,900)

5.2.5 Axial Velocity Fluctuations Profiles

Axial velocity fluctuation profiles are illustrated in Figures 5-23 and 5-24. The maximum value of the fluctuation is attained in the region where the annular jet enters the wake at around r/D = 0.38. The peak of the fluctuation close to the wall decreases as the distance increases from the bubble bottom. This is due to spreading of the annular jet. The high fluctuations immediately behind the bubble (Z/D= -0.01 to Z/D= -0.6) may be partly due to the oscillation of the bubble bottom. The fluctuations decrease with distance away from the bubble bottom. For Case 7, they decrease to $0.2U_{TB}$ at Z/D= -2 and to $0.1U_{TB}$ at Z/D= -4 and become very small around Z/D= -8. The turbulence intensity relative to the bubble velocity for this case is smaller than for the stagnant Case 2. For Case 8, they decrease to $0.2U_{TB}$ at Z/D = -1.3, to less than $0.1U_{TB}$ at Z/D = -4 and they become very small around Z/D = -8.

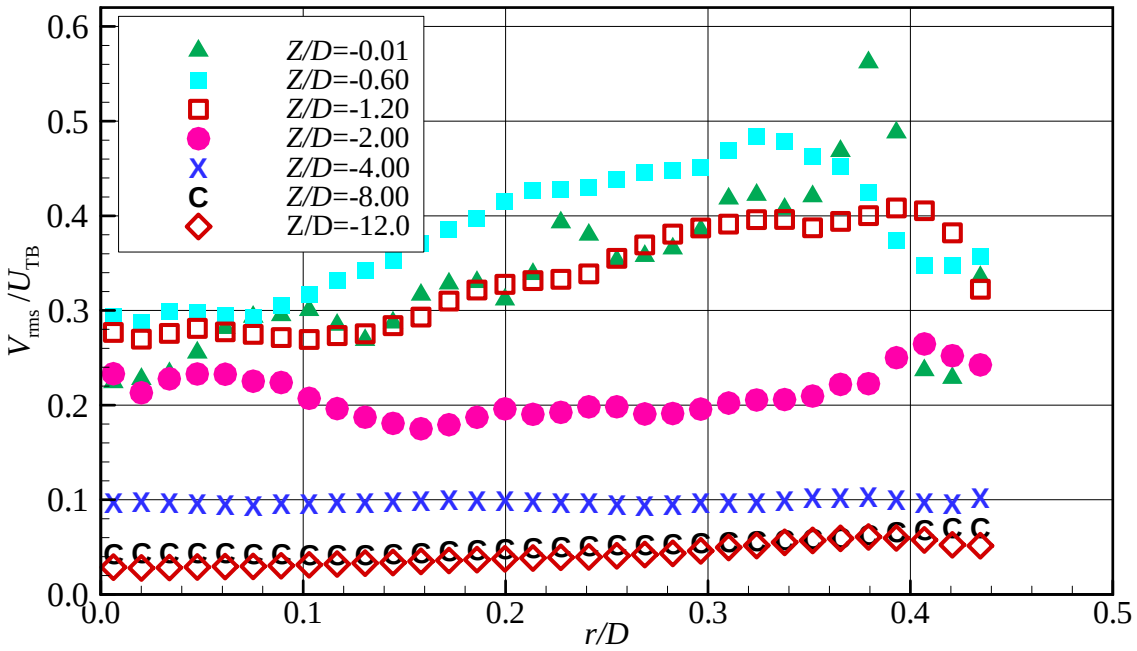

Figure 5-23: Radial profiles of axial turbulence intensity at various axial positions in the near wake of a Taylor bubble rising in laminar flowing liquid (Case 7: Re_{TB} = 3,800, Re_L = 1,500)

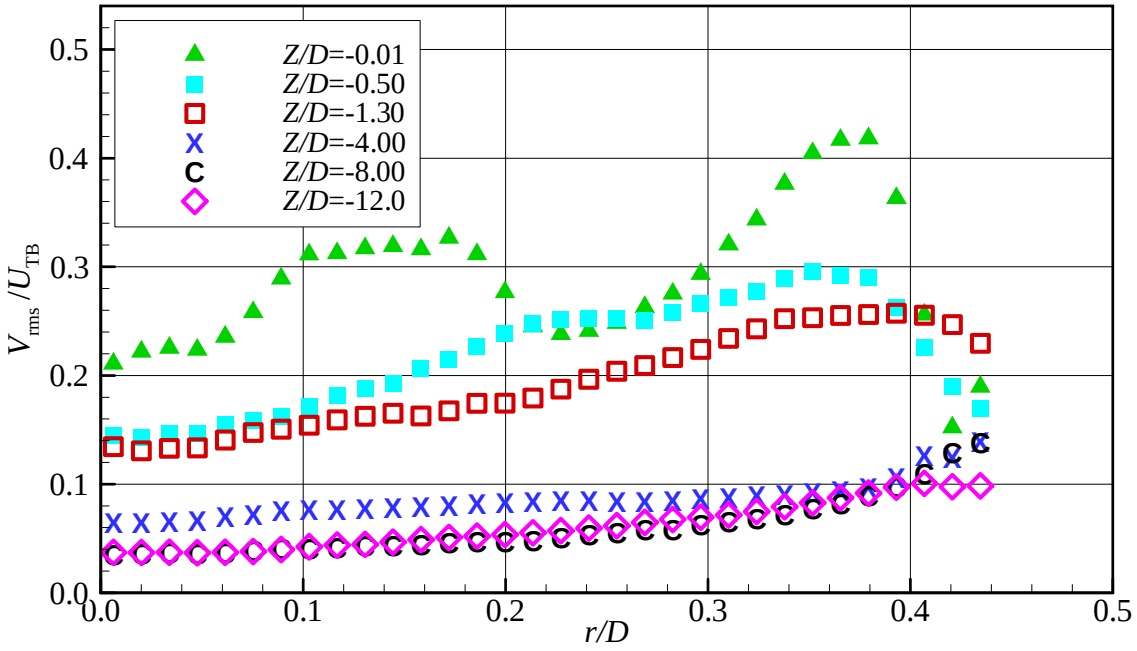

Figure 5-24: Radial profiles of axial turbulence intensity at various axial positions in the near wake of a Taylor bubble rising in turbulent flowing liquid with (Case 8: Re_{TB} = 5,700, Re_L = 3,900)

5.3 Wakes of Taylor Bubbles Rising in an Upward Moving Mixture of Water and Glycerol (μ = 0.0430 Pa·S)

5.3.1 Introduction

The experimental conditions for this case are shown in Table 5-5. Even though the bubble is rising in a laminar upward flowing liquid, the flow pattern in the wake of the Taylor bubble is transitional (Type II) according to Campos and Geudes de Carvalho (1988) and Pinto *et al*. (1998). Since the mean flow is axisymmetric around the tube centreline, the results presented for this case are obtained from averaging the left and the right halves of the velocity field thus doubling the ensemble size to 140.

Figure 5-25 shows an instantaneous image of the bubble bottom of a Taylor bubble rising under these conditions (refer to Appendix B for more images). The concave shape of the bubble bottom is maintained even though the bottom of the bubble starts to oscillate as the background liquid conditions changed from stagnant to flowing liquid. Also, very few bubbles are shed from the Taylor bubble.

Table 5-5: Experimental conditions of Taylor bubbles in a flowing water-glycerol mixture (μ=0.0430 Pa·s)

Case #	μ (Pa·s)	U_{TB} (m/s)	Re_{TB} (-)	U_L (m/s)	U_{cl} (m/s)	U_{cl}/U_{TB} (-)	Re_L (-)	Re_R (-)
Case 9	0.0430	0.878	620	0.377	0.754	0.859	260	360

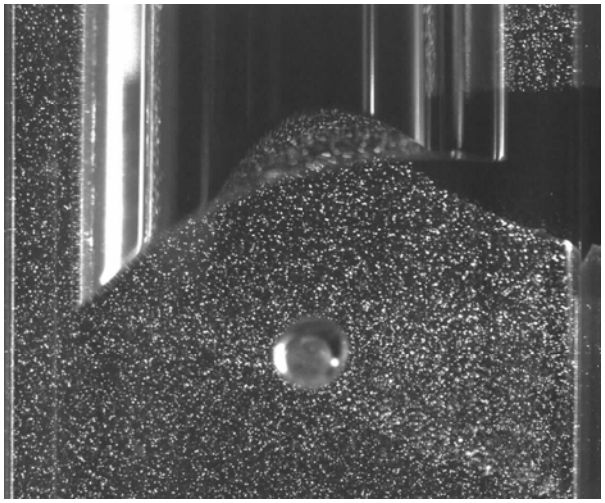

Figure 5-25: Bottom surface of a Taylor bubble rising in upward flowing mixture of water and glycerol: Case 9 (Re_{TB} = 620 & Re_{L} = 260)

5.3.2 Mean Flow Field in the Near Wake

Figure 5-26 shows the mean velocity vectors and streamlines in a frame of reference moving at the bubble velocity in the near wake of a Taylor bubble rising in a laminar upward flowing liquid (Case 9). The mean flow structure in this case is similar to the stagnant case (Case 3). The instantaneous velocity fields (not shown here) showed that the wake starts to lose the axial symmetry which had been observed in the stagnant case (Case 3). The mean velocity field is similar to the stagnant case. A summary of the primary recirculation zone parameters is given in Table 5-6. The radial location of the vortex slightly changed between the stagnant and flowing cases. This similarity is due to the confinement of the tube walls. However, for the flowing liquid the axial location of the vortex has shifted toward the bubble and the length of the recirculation region is elongated in this case. This is in contrast to the previous case (Case 7) where the flowing liquid has no effect on the length of the wake.

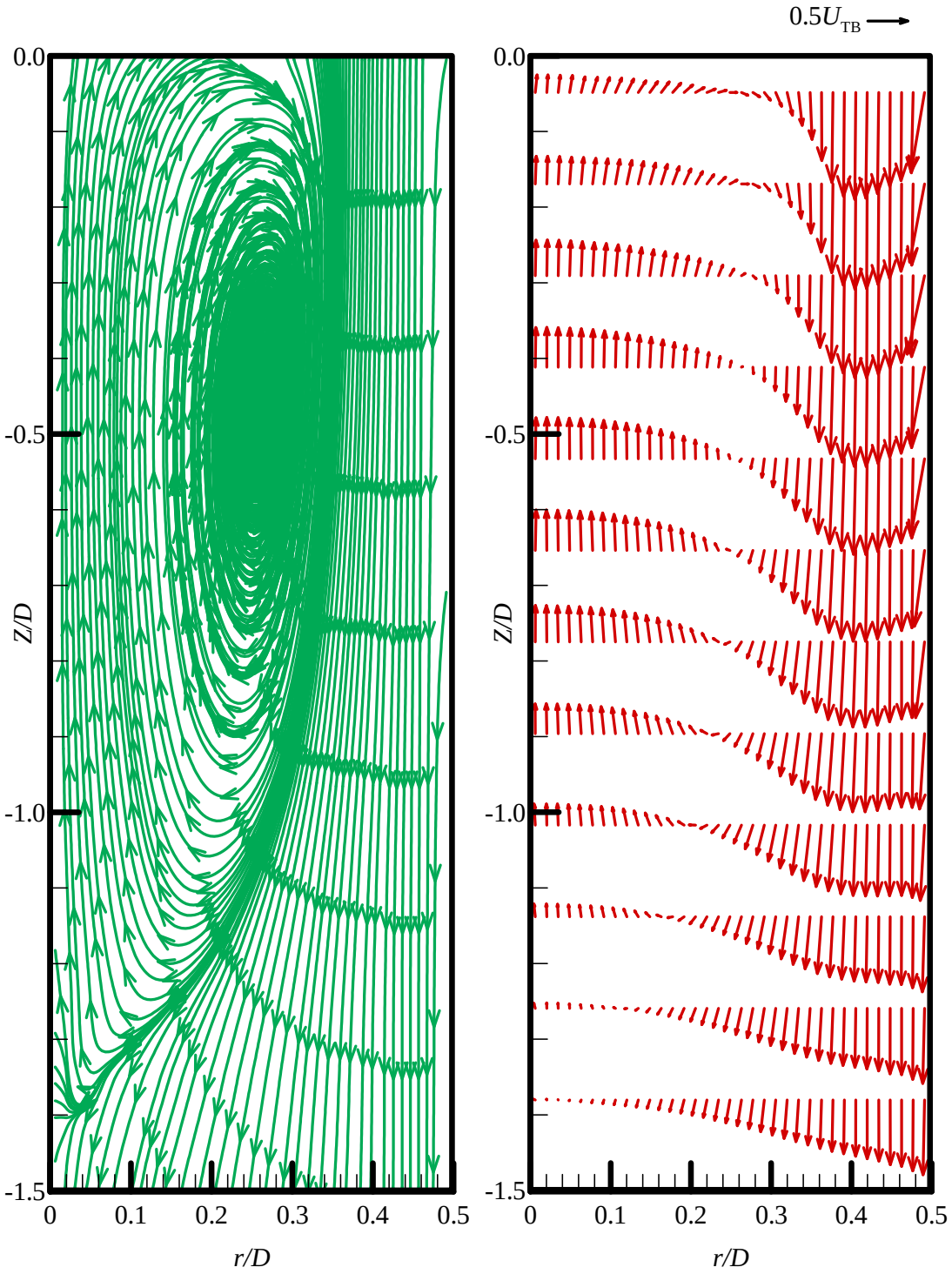

Figure 5-26: Mean velocity vectors and streamlines in the near wake of the Taylor bubble shown in a moving frame of reference (Case 9: Re_{TB} = 620, Re_L = 260).

Table 5-6: Summary of the primary recirculation zone parameters for Case 9

Case #	μ_L (Pa·s)	Re_L (-)	Vortex core location		Wake pattern	Primary recirculation zone length
			Z/D	*r/D*		
Case 9	0.0430	259	-0.46	0.26	Transitional	1.4*D*

5.3.3 Axial Velocity Profiles

Figure 5-27 shows the axial velocity at the tube centreline as a function of the distance from the bubble bottom. For this case, the mean axial velocity increases from velocity that is a little higher ($1.2U_{TB}$) than the bubble rise velocity at the bottom (this is due to the concave shape of the bubble bottom) to reach a maximum at *Z/D* = -0.6. The maximum upward velocity is around $1.55U_{TB}$. The velocity then decreases to the Taylor bubble velocity at *Z/D*= -1.4, continues to decreases ($0.65U_{TB}$) slowly until *Z/D*= -3 and then starts to increases again to establish the fully-developed laminar flow (U_{cl}/U_{TB} =-0.858) at *Z/D*= -10. It is clear that the re-establishment of fully-developed laminar flow in this case was achieved in a shorter distance than in Case 7. This may be due to the fact that the flow in the wake is transitional in this case and turbulent in Case 7.

Radial profiles of the axial velocity at selected locations in the wake of the bubble are presented in Figure 5-28. The maximum value of the axial velocity equals $1.55U_{TB}$ at *Z*=-0.5*D*. The maximum downward velocity is $-0.5U_{TB}$ at *Z*=-0.01*D*. In this case, both the reverse velocity and the jet velocity relative to the bubble rise velocity are less than the stagnant case (Case 3).

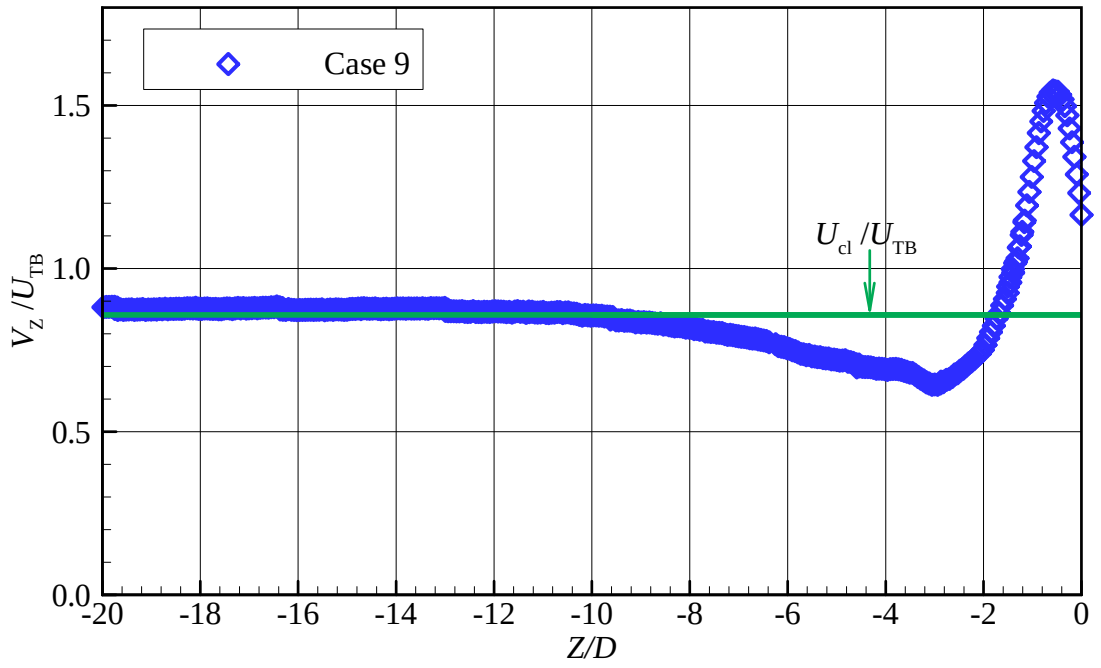

Figure 5-27: Axial velocity at the tube centreline in wake of Taylor bubble rising in upward laminar flow (Case 9: Re_{TB} = 620, Re_L = 260)

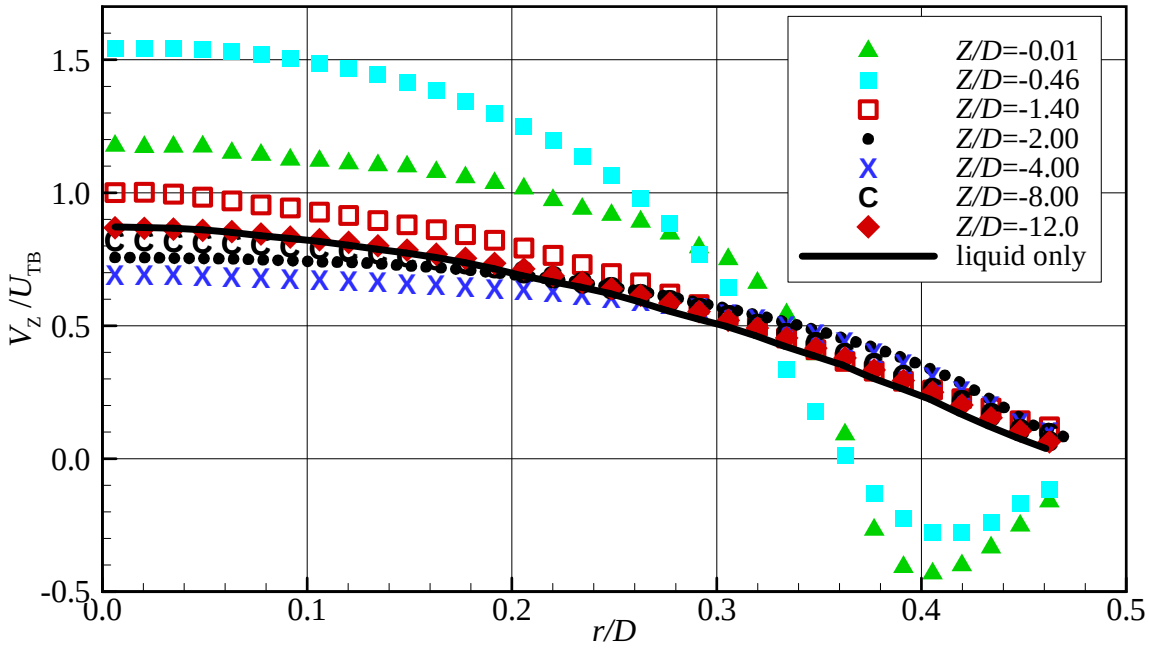

Figure 5-28: Radial profiles of axial velocity at various axial positions in the wake of a Taylor bubble rising in laminar flowing liquid (Case 9: Re_{TB} = 620, Re_L = 260)

5.3.4 Radial Velocity Profiles

Radial profiles of the radial velocity at different locations behind the bubble are illustrated in Figure 5-29. The radial velocity is much lower than the axial velocity. The direction and the behavior of the radial velocity are similar to that of the stagnant case. However, the magnitude of the radial velocity relative to the bubble velocity is less than that for the stagnant case (Case 3). At Z/D = -2 the radial velocity component essentially vanishes.

5.3.5 Axial Velocity Fluctuations

Axial velocity fluctuations are illustrated in Figure 5-30. The maximum value of the fluctuation is attained in the region where the annular jet enters the wake at around r/D = 0.30. The peak of the fluctuation close to the wall decreases quickly compare to the previous cases as the distance increases from the bubble bottom. This is due to spreading of the annular jet. The high fluctuations immediately behind the bubble (Z/D= -0.01) may be due partly to the oscillation of the bubble bottom. The fluctuations decrease with distance away from the bubble bottom. They decrease to $0.2U_{TB}$ at Z/D = -0.5 and to $0.1U_{TB}$ at Z/D= -2. Then they become very small around Z/D = -4.

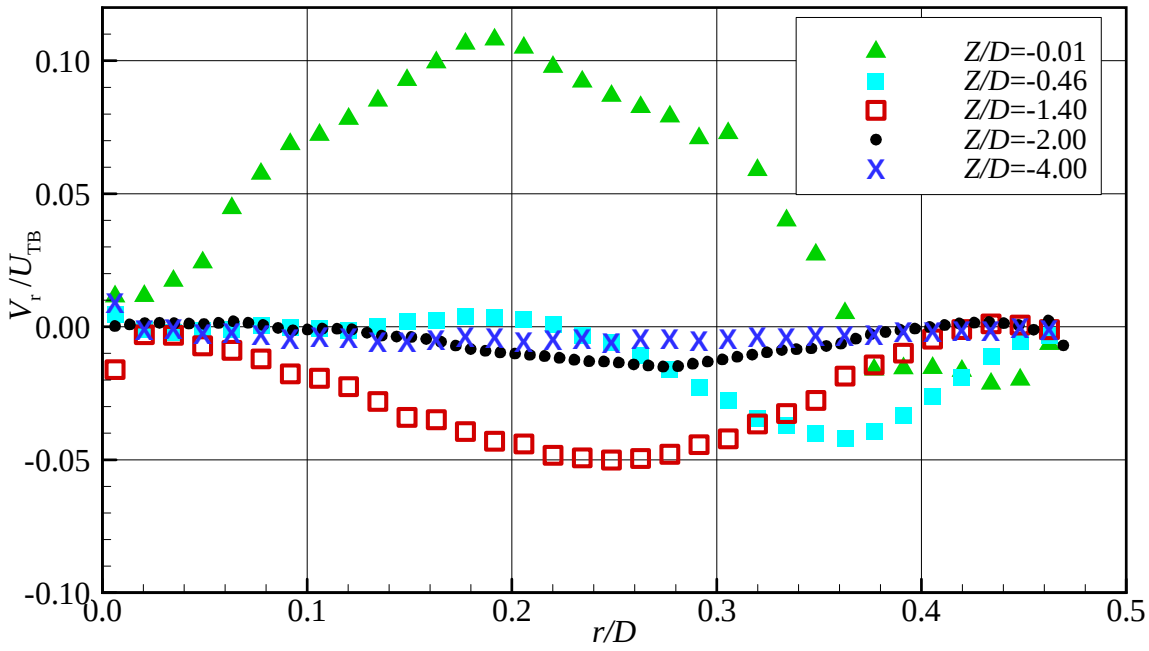

Figure 5-29: Radial profiles of radial velocity at various axial positions in the wake of a Taylor bubble rising in laminar flowing liquid (Case 9: Re_{TB} = 620, Re_L = 260)

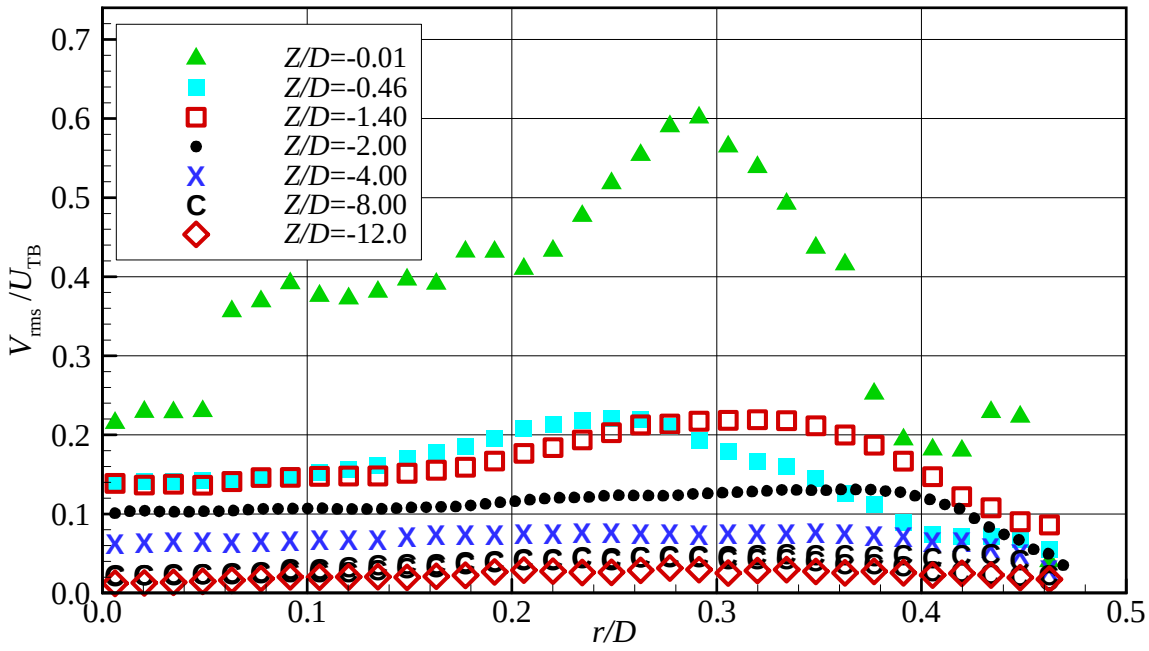

Figure 5-30: Radial profiles of axial turbulence intensity at axial positions in the wake of a Taylor bubble rising in laminar flowing liquid (Case 9: Re_{TB} = 620, Re_L = 260)

5.4 Effects of the Upward Flowing Liquid in the Near Wake of Taylor Bubbles

In order to give an overview of the recirculation zone characteristics for each case, a summary of results is given in Table 5-7. The length of the primary recirculation zone depends on both the liquid viscosity and the flow rate. For all three liquids, increasing the liquid flow rate increases the length of the recirculation zone. However, in Cases 5 and 6, the primary recirculation length stays constant even though the flow rate of the flowing liquid increases. For the intermediate viscosity cases (Cases 2, 7 and 8), the effect of increasing flow on the wake length is slight. For laminar flow (Case 7), there was no significant change in the length of the wake from that of stagnant case (Case 2). However, there was a slight increase (less than 10%) in the wake length in the case of turbulent flowing liquid (Case 8). The quiet zone (Figure 4-12), which exists in the stagnant case and constitutes part of the primary recirculation zone, does not exist in the flowing liquid cases. For the high viscosity liquid (Cases 3 and 9), the increase in the liquid flow rate increases the length of the wake drastically. For the stagnant case, the length of the wake is 0.68D and it more than doubles as the flowing liquid is introduced. This may be due to the fact that the wake structure changed from a laminar wake in Case 3 to a transitional wake in Case 9.

Even though the recirculation zone is getting larger, increasing the liquid flow rate shifts the axial location of the vortex centre toward the bubble's bottom (Table 5-7). This is clearly demonstrated in the intermediate viscosity liquid where the change in wake length is small. In the case of the stagnant liquid (Case 2), the axial location of the vortex core was located at Z=-0.68D and was pushed up toward the bubble bottom by the upward flowing liquid to Z=-

0.62*D* in Case 7 and further pushed to *Z*=-0.51*D* in Case 8. Another example of this effect is in Case 5 and Case 6. Even though the wake length stays constant in both cases as the flow rate increases, the axial location of the vortex core is shifted from *Z*=-0.52*D* in Case 5 to *Z* = -0.42*D* in Case 6. Increasing the liquid flow has a slight effect on the radial location of the core vortex (*r/D* = 0.26 ~ 0.29). This may be due to the tube wall confinement.

Table 5-7: Summary of the primary recirculation zone parameters for all cases

μ (Pa·s)	***Case #***	**Re_L (-)**	**Vortex core location**		**Wake pattern**	**Primary recirculation zone length**
			Z/D	***r/D***		
0.00100	Case 1	0	-0.52	0.28	Turbulent	1.23*D*
	Case 4	9,200	-0.55	0.27		1.73*D*
	Case 5	13,600	-0.52	0.27		1.92*D*
	Case 6	17,800	-0.42	0.27		1.90*D*
0.00500	Case 2	0	-0.68	0.29	Turbulent	1.20*D*
	Case 7	1,500	-0.62	0.27		1.22*D*
	Case 8	3,900	-0.51	0.27		1.34*D*
0.0430	Case 3	0	-0.14	0.27	Laminar	0.68*D*
	Case 9	260	-0.46	0.26	Transitional	1.40*D*

The dividing streamline (see section 4.3.2) is one way to characterize the extent of the recirculation zones. It is defined as the streamline that ends at the stagnation point of the main vortex (section 4.3.2). It is the line that separates the falling film from the recirculation zone in a moving frame of reference. These lines are showing in Figures 5-31 and 5-32 for all cases. Even though it is difficult to measure the film thickness at the bubble bottom, it is clear from Figure 5-32 that the falling film width increases for the cases of moving liquid.

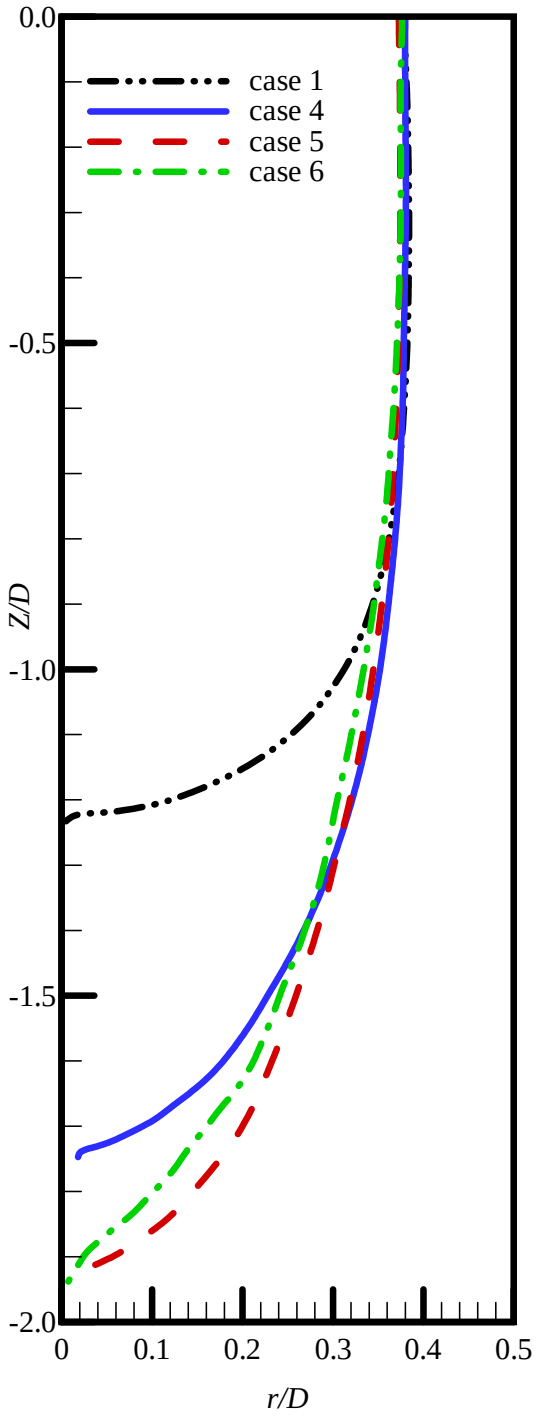

Figure 5-31: Dividing streamlines for the low viscosity cases

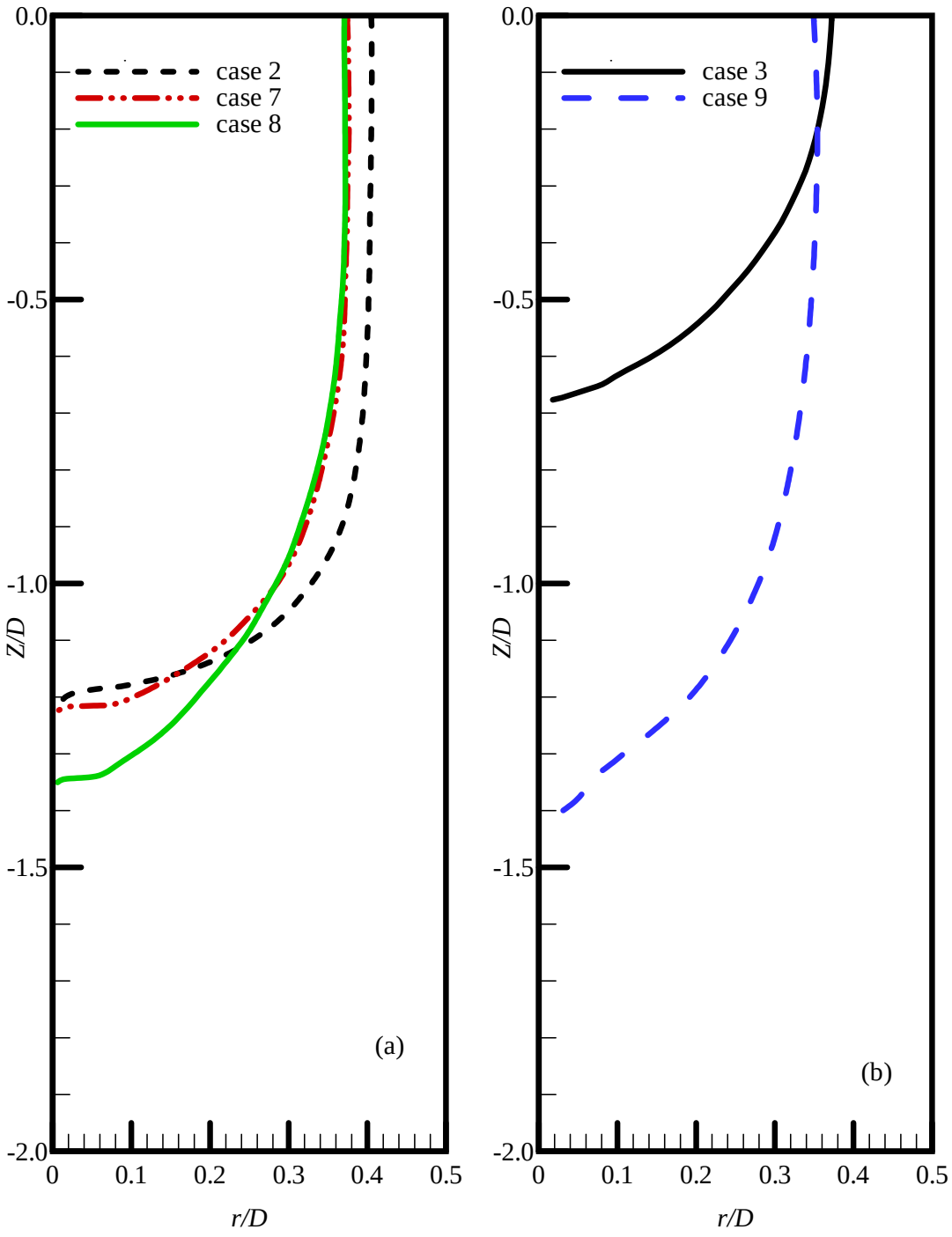

Figure 5-32: Dividing streamlines for: (a) the intermediate viscosity cases, (b) The high viscosity cases

5.5 Effects of the Upward Flowing Liquid on the Bubble Shape

The liquid flow rate affects the shape of the Taylor bubbles. Figure 5-33 shows the instantaneous nose shape and the developing falling film of bubbles rising in stagnant, laminar and turbulent upward flowing liquids. These bubble shapes were traced by hand from PIV images. Even though the shape of the bubble extracted from PIV images is always smaller than the real shape of the bubble (Nogueira *et al.*, 2003), qualitative information can be obtained from these images. The effects of the upward flowing liquid on the nose, the falling film and the oscillation of the trailing edge are discussed.

5.5.1 Nose Shape

From Figure 5-33, it is clear that the tip of the nose has a spherical shape in all three cases. The radius of curvature at the nose is smaller in the case of laminar flowing liquid. Apparently, the shape of the liquid velocity profile ahead of the Taylor bubble significantly affects its shape. A fully-developed laminar flow in a tube has a parabolic shape with largest velocity at the pipe centerline and zero velocity at the wall. In turbulent flow, a fairly flat velocity distribution exists across the middle section of pipe. The nose exhibits an axisymetric shape around the tube axis for both the stagnant and laminar cases. However, the instantaneous shape (shown in Figure 5-33) of the bubble becomes asymmetric in the case of a turbulent upward flowing liquid. This asymmetry is not biased toward one side of the tube and the mean shape is axisymmetric.

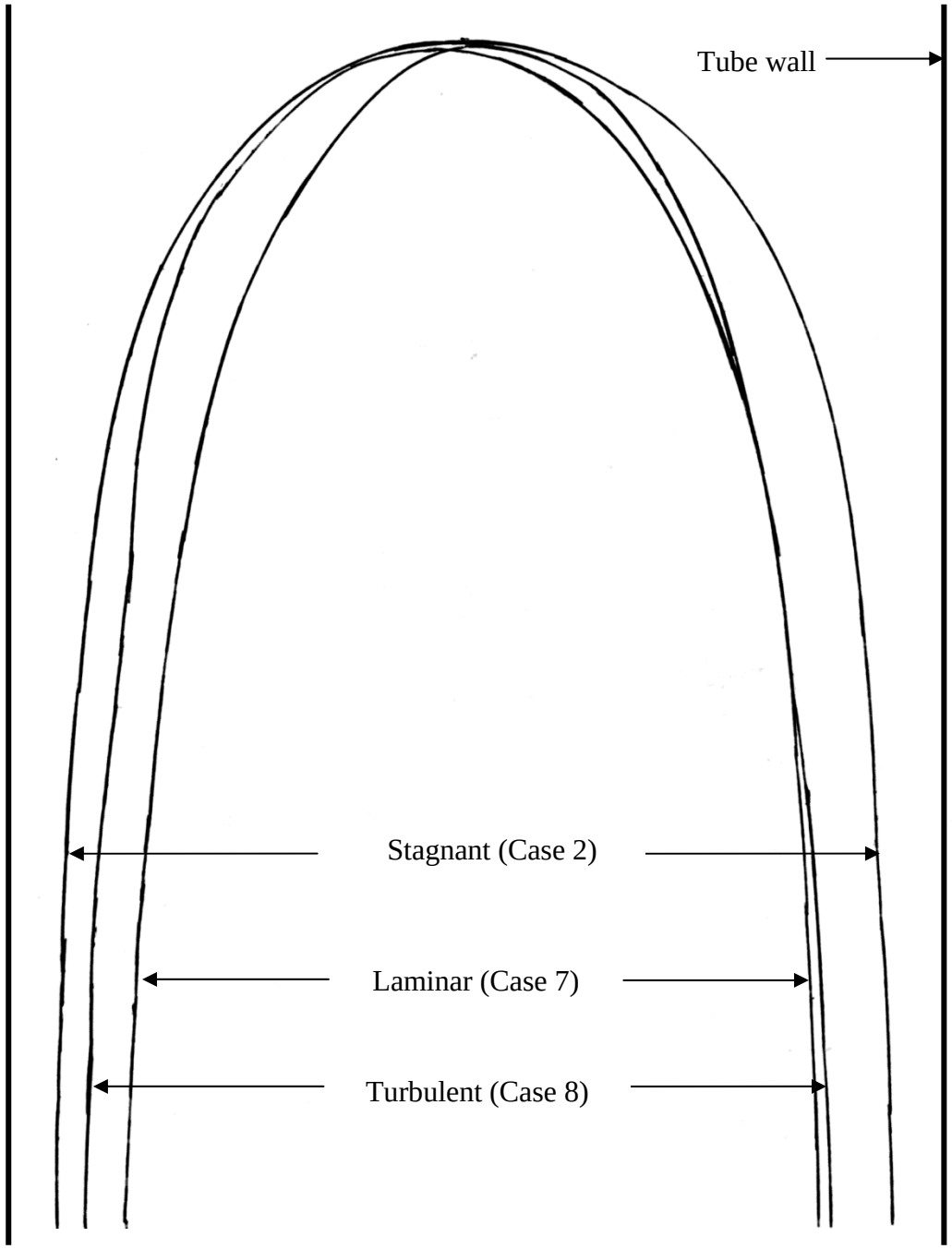

Figure 5-33: Bubble shape for the intermediate viscosity in stagnant, laminar and turbulent flows

5.5.2 Falling Film

In Figure 5-33, the falling film is thicker for the flowing liquid cases than for stagnant cases. Also, for laminar flow, the falling film is thicker than for turbulent flow. This is consistent with the findings of Zheng and Che (2006). In order to explain the film thickness difference between turbulent and laminar cases, a mass balance in the liquid was performed (refer to Section 3.6). A control volume moving at the bubble speed is used to check the mass balance. The top of the control volume is placed well ahead of the bubble where the flow is fully-developed (i.e. undisturbed). The bottom of the control volume can be placed at any axial location in the falling film. It was found that the liquid mass flow into the top of this control volume in the laminar case is higher than in the turbulent case. This increase in the liquid mass flow can be balanced in the falling film either by an increase in the film thickness or the film mean velocity or both. By looking at the film thickness (Figure 5-33) and the axial velocity profiles at Z/D=0.01 (Figures 5-19, 5-20), it is clear that the increase in the liquid mass flow in the laminar case was achieved by increasing both the film velocity and the film thickness.

5.5.3 Trailing Edge Oscillation

The effects of the flowing liquid on the bubbles bottom were discussed throughout Chapters 4 and 5. However, this discussion can be summarized into two main effects. First, as the liquid flow rate increases, the oscillating of the bottom surface increases. Second, it was observed that increasing the liquid flow rates increases the number of small bubbles shed from the bubble bottom. This may be due to high turbulence intensity and the oscillations of the bubble bottom in the near wake.

5.6 Bubble Coalescence

In this section, the coalescence of two consecutive Taylor bubbles is discussed based on the PIV velocity field measurements in the wake of single Taylor bubbles presented in Chapters 4 and 5. The wake region of Taylor bubbles is crucial in determining the characteristics of fully-developed slug flow. The minimum stable liquid slug length is defined as the minimum distance needed to re-establish a fully-developed velocity distribution in the liquid in front of the trailing Taylor bubble (Mossis and Griffith, 1962). Mossis and Griffith (1962) also stated that the trailing Taylor bubble is influenced by the velocity distribution ahead of it. They were the first to note (using a camera moving with the leading bubble) that the nose of the trailing bubble distorts and becomes alternately eccentric on one side or another of the tube. This has since been observed by many investigators. They obtained a minimum stable liquid slug length of 12-16*D*. The process of slug development and the prediction of minimum stable liquid slug length have since been investigated by several researchers (Pinto and Campos (1996), Wakuda (1999), van Hout *et al*. (2002), Zheng and Che (2006), and Mayor *et al.* (2007)). Table 5-4 summarises these research results. The early experiments suggest that this length does not depend on gas and liquid flow rates or fluid properties. However, the ranges of measured stable length shown in Table 5-4 suggest that this length does depend on the flow conditions and liquid properties. Pinto and Campos (1996) reported that this length depends on the flow regime in the bubble wake (or ranges of *N*). They divided the minimum stable length into two parts. One is the near wake of the leading bubble and the other is the distance needed by the liquid flow to reestablish its fully-developed conditions.

Table 5-8: Some minimum stable liquid slug length results from the literature.

Investigators	Flow conditions	Minimum stable length
Mossis and Griffith (1962)	Stagnant and upward flow water in a 25 mm tube	12-16*D*
Pinto and Campos (1996)	water and glycerol mixture in 19, 32, and 52 mm tubes	12.5*D*
Wakuda(1999)	Stagnant water in 22 mm tube	5*D*
van Hout *et al*.(2002)	Stagnant and upward flow water in a 25 mm tube	12*D*
Zheng and Che (2006)	Upward flow, water in a 35 mm tube	7.5-10*D*
Mayor *et al*.(2007)	Upward flow, water in 32 and 52 mm tubes	8-10*D*

Based on the PIV measurements in the wake of a single Taylor bubble made in this thesis, an attempt to explain the coalescence mechanism of the trailing bubble with the leading bubble can be made. The nine cases reported in this thesis are categorised based on the background liquid flow into three scenarios: bubbles rising in stagnant liquids, bubbles rising in upward laminar flow, and bubbles rising in upward turbulent flow.

5.6.1 Stagnant Liquid

Figure 5-34 is a schematic diagram of two Taylor bubbles and representative velocity profiles (in a fixed frame of reference) between the Taylor bubbles rising in stagnant water (Case 1). These velocity profiles are similar to the profiles in Figure 4-13 (Z/D = -0.5, -2, -4). They represent the flow in the first part of the minimum stable length (occupies around 5*D* in the stagnant water case) according to the definition of Pinto and Campos (1996). In this part,

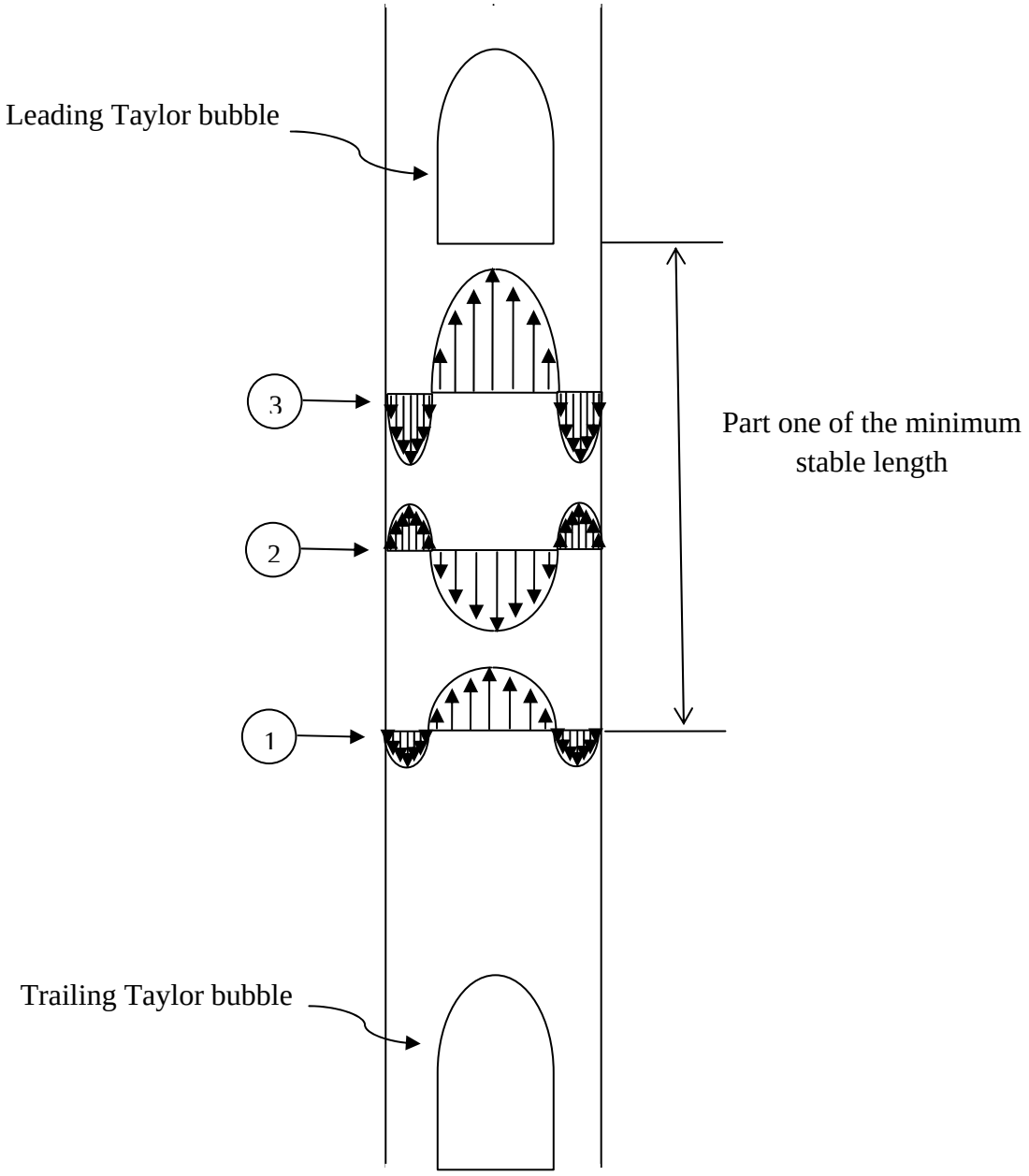

Figure 5-34: Schematic diagram of two Taylor bubbles rising in a vertical tube shown in a fixed frame of reference (not to scale)

the coalescence of Taylor bubbles can be interpreted based on the assumption that the bubble follows the maximum liquid velocity in the pipe cross section. First, the trailing bubble accelerates following the centerline velocity ahead of it (profile 1 in Figure 5-34). Next, the nose swings from one side of the tube wall to the other following the maximum velocity

close to the tube wall (Profile 2). Then, as the bubble enters the preliminary recirculation zone region (represented by Profile 3), it distorts significantly due to the high turbulence intensity and eventually merges with the leading bubble. According to the PIV measurements, the length of part one is about 4*D* in Cases 1 and 2 and 2*D* in Case 3. The liquid slug minimum stable length is 9*D* (Cases 1 and 2) and 2*D* in Case 3. These findings agree with the findings in Table 5-8.

5.6.2 Laminar Upward Liquid Flow

In both cases of a laminar background flow (Cases 7 and 9), the high turbulence intensity in the wake occupies a distance of around 4*D* even though the wake flows are turbulent in Case 7 and transitional in Case 9. The axial velocity at the centreline reaches its minimum at around 4*D* behind the bubble and then approaches the fully-developed value. For Case 7 (Figure 5-18), the velocity of a trailing bubble in the region $28D > Z > 4D$ will expect to be less than the velocity of a leading bubble. Therefore, the separation distance between the two bubbles will increase in this region and no coalescences will take place. In Case 7, the velocity at the tube centreline continues to increase in the whole measurement domain. For example, the liquid velocity at the tube centreline (V_z/U_{TB}) is 0.57 at 13*D* and it is 0.65 at 25*D*. This confirms the finding of Pinto *et al.* (1998) that the separation distance between the leading bubble and the trailing bubble increases as the bubbles rise in a laminar upward liquid flow when the separation distance exceeds about 5*D*. In contrast to Case 7, in Case 9, a fully-developed laminar flow (Figure 5-28) is achieved at around 10*D*. The difference in the distance to achieve fully-developed flow between Case 7 and 9 may be due to the fact that the flow patterns in the wake of the two cases are different. In Case 9, the flow in the wake

behind the bubble is transitional so that it takes the flow a shorter distance to return to a laminar flow. To this end, for the two laminar cases, the separation distance to have no bubble interaction is around 4*D*. However, the minimum stable length is 10*D* for Case 9 and > 28*D* for Case 7.

5.6.3 Turbulent Upward Liquid Flow

It is clear from Figures 5-6 to 5-8 that the fully-developed velocity profile for a turbulent upward flowing liquid is achieved as early as a distance of 4 tube diameters below the bubble. However, Figures 5-12 to 5-14 show that at 4*D* from the bubble bottom the turbulence intensity is still quite high and does not match the fully-developed turbulent flow until 12*D*. It can be concluded that the liquid slug minimum stable length for turbulent upward flowing liquid (Cases 4, 5, 6 and 8) is around 12*D*.

From the above discussion, the experimental results indicate that the flow pattern in the wake (laminar, transitional or turbulent) and the liquid flow rate play a role in the coalescence of Taylor bubbles. For example, two bubbles rising in laminar flow (Case 7) tend to move apart when they are separated by distance of 5~28*D*. For all turbulent cases, the liquid slug minimum stable length is around 12*D*. In stagnant cases, the liquid slug minimum stable length ranges from 2*D* to 9*D*, and depends on the flow regime in the bubble wake. These ranges agree with the literature.

6 Conclusions and Recommendations

After designing and constructing an apparatus to generate single Taylor bubbles rising in stagnant and flowing liquids in a 25.31 mm vertical tube (Re_L= 250 to 17,800), PIV measurements were taken around the nose and in the wake of Taylor bubbles. The working fluids were filtered tap water and mixtures of glycerol and water (μ=0.0010, 0.0050 and 0.043 Pa·s) and air. The shape of the Taylor bubbles was determined using digital photography and image processing techniques. Terminal velocities were measured using phase detectors. The conclusions, contributions and recommendations from this study can be summarized as follows:

6.1 Conclusions

6.1.1 Stagnant Liquid

1. The measured Taylor bubble rise velocity in stagnant liquids is constant for the three viscosities studied in this thesis. The rise velocity matches the expected value for the inertia-controlled regime.
2. Above the nose, the fluid at the centre of the tube moves upward. The bubble is first felt at z/D=0.5 above the nose for all three stagnant cases. Near the nose, the axial velocity of the liquid is approximately equal to the terminal velocity of the bubble and the direction is upward. The fluid midway between the wall and the tube centre has a strong radial velocity. The fluid close to the wall moves downward. In the falling film

region, the axial velocity increases and the film thickness decreases with increasing distance below the nose.

3. The shape of the bubble bottom is different from case to case. For the low viscosity liquid (μ=0.0010 Pa·s), the bubble bottom is highly irregular and oscillating. For the intermediate viscosity liquid (μ = 0.0050 Pa·s), the bubble bottom is flat and the bottom oscillations are much weaker than for the low viscosity case. For the high viscosity liquid (μ = 0.043 Pa·s), the bubble bottom has a concave shape and is not oscillating. The bubble bottom has sharp edges for the low and high viscosity cases and rounded edges for the intermediate viscosity case.
4. At the bubble bottom, the falling film penetrates into the liquid below the bubble driving a toroidal recirculation zone behind the bubble. The type of the wake depends on the dimensionless inverse viscosity. In this study, the high viscosity case has a laminar wake and the low and intermediate viscosity cases both have turbulent wakes.
5. In a frame of reference moving with the bubble, the near wake mainly consists of one large vortex. For the low viscosity case, the wake is turbulent and the primary recirculation zone extends from the bubble bottom surface to 1.23D below the bubble. In this region, the maximum value of the upward velocity is 3.2U_{TB}.
6. For the intermediate viscosity, the wake is turbulent and the length of the primary recirculation zone is 1.22D. However, the existence of a quiet zone (a very weak recirculation zone at the centre of the tube immediately underneath the bubble) is observed in the wake structure. The maximum value of the axial upward velocity is 2.3U_{TB}.

7. For the high viscosity, the length of the primary recirculation zone is reduced to 0.68*D*. The length of the recirculation zone measured here does not include the part of the wake inside the concave tail of the bubble. The maximum value of the axial upward velocity is $2.8U_{TB}$.
8. The viscosity is clearly affecting both the structure and the size of the primary recirculation zone.
9. The minimum stable liquid slug length (the minimum distance needed to re-establish a fully-developed velocity distribution in the liquid in front of a trailing bubble) is 9*D* for the low and intermediate viscosity and 2*D* for the high viscosity. It depends on the flow regime in the wake. In turbulent wake cases (the low and intermediate viscosity), the minimum stable liquid slug length is 9*D*. In laminar wake case (high viscosity), it is 2*D*.

6.1.2 Flowing Liquid

1. In the upward flowing cases, the type of the wake depends on the relative motion between the two phases (relative Reynolds number). The wake is turbulent in all cases except the high viscosity, laminar flow case where the wake is transitional.
2. The length of the primary recirculation zone depends on both the liquid viscosity and the flow rate. In general, the length of the primary recirculation zone increases with increasing liquid flow rate. For the low viscosity cases, the length of the primary recirculation zone increases from 1.23*D* for the stagnant case to 1.73*D* for Re_L= 9,200 and becomes essentially constant at 1.90*D* for $Re_L \geq$ 13,600. For the intermediate

viscosity, the length of the recirculation zone in the flowing case (Re_L=1,500) equals that of stagnant case (1.22*D*). However, the quiet zone region was not observed in the flowing case. The length of the recirculation zone is increased to 1.34*D* for Re_L=3,900. For the high viscosity, the length of the recirculation region is elongated from 0.65*D* for the stagnant case to 1.4*D* for Re_L=260.

3. One other effect of increasing the liquid flow rate is to shift the axial location of the vortex centre toward the bubble bottom. For example, in the low viscosity cases, even though the wake length stays constant for $Re_L \geq$ 13,600 the axial location of vortex core is shifted from *Z*=-0.52*D* to *Z*=-0.42*D* as the flow rate increases. Increasing the liquid flow has only a slight effect on the radial location of the vortex centre (*r/D*=0.26~0.29). This may be due to the tube wall confinement.
4. The shape of the liquid velocity profile ahead of the Taylor bubble significantly affects its shape. The radius of curvature at the nose is smaller in the case of laminar flowing liquid.
5. The flowing liquid cases show that the falling film thickness increases with increasing flow rate.
6. As the liquid flow rate increases oscillations of the bottom surface also increase. Also, it was observed that increasing the flow liquid rate increases the number of small bubbles shed from the bubble bottom.
7. For laminar upward flow, the separation distance to have no bubble interaction is around 4*D*. However, the minimum stable length is 10*D* for the high viscosity and >28*D* for the intermediate viscosity.

8. The minimum stable liquid slug length for turbulent upward flowing liquid is around 12*D*.

6.2 Contributions

1. A two-phase, gas-liquid vertical flow loop was designed and constructed to create Taylor bubbles that rise in stagnant and upward flowing liquids. This loop has a pumping system which is able to deliver different liquids (range of viscosities) at the desired flow rates. With minor modification to the injection system, this loop can be used to create other gas-liquid flow regimes such as bubbly and annular flows. The pumping system was also selected so that it can be used in a horizontal two-phase loop in the future.
2. It is noticed that the bottom of the bubble location is different from image to image. Therefore, the location of interface at the tube centerline is determined using the Inspector® image processing software. To improve the data averaging in the wake, the velocity field data are shifted axially based on the bubble bottom location for each bubble. Then an ensemble average of the shifted velocity fields is calculated.
3. The PIV measurements in this study have added new insights into the characteristics of the wake of Taylor bubbles rising in stagnant and upward flowing liquids for all possible flow regimes. The present investigation provides new information of the effect of the bubble bottom shape on the wake of Taylor bubbles. For example, for the intermediate viscosity, the wake of Taylor bubble rising in stagnant liquid, a very

weak recirculation zone at the centre of the tube immediately underneath the bubble is observed for the first time as a result of the round edges of the bubble bottom surface.

4. Very few studies have appeared in the literature which focused on the wake structure of a single Taylor bubble rising in a flowing liquid. This thesis provides detailed information about the wake characteristics and the effects of the liquid flow rate on the wake. Specific contributions include information about the primary recirculation zone parameters (size, vortex centre location, .etc) and the effect of the liquid flow rate on the bubble nose shape and bottom surface shape. For example, even though the recirculation zone in the wake gets larger with increasing the liquid flow rate, the axial location of the vortex centre shifts toward the bubble's bottom. Also, these detailed experimental results can be used to verify computational fluid dynamics modeling of slug flow.
5. In the present investigation, the interaction between Taylor bubbles was analyzed based on PIV measurements in the wake of a single Taylor bubble rising in stagnant or flowing liquids. The experimental results showed that the liquid flow rate plays a role in the interaction of the bubbles. For example, for laminar flow and intermediate viscosity, the PIV measurements ($28D > Z > 4D$) showed that the liquid velocity at the tube centerline continues to increase for the whole measurement domain (fully-developed laminar flow in a pipe is not re-established). This explains the finding of Pinto *et al.* (2001) that the separation distance between the leading bubble and the trailing bubble increases as the bubbles rise in a laminar flow when the separation distance exceeds about $5D$.

6.3 Recommendations

1. The mean velocity field does not reveal the unsteady structure of the wake of Taylor bubbles. Analyzing the instantaneous flow fields can provide quantitative information about coherent structures of the flow. For example, applying proper orthogonal decomposition analysis in the wake may reveal the effect of Taylor bubble bottom oscillation on the wake structure.
2. The experimental study for the two laminar flow cases has shown that a fully developed laminar flow is achieved at 10D behind the bubble in one case (Re_L=260) but the other case (Re_L=1,500) showed signs of undeveloped laminar flow even at the end of the measurement domain (28D). It would be interesting to carry out more velocity measurements in laminar flow at different flow conditions (1,500 > Re_L > 260) and extend the domain of the measurements behind the bubble (> 60D).
3. Part of the difficulty in making measurements close to the wall was the optical distortion associated with the curved walls of the tube. This difficulty can be solved if the liquid and the tube material have the same index of refraction. Another difficulty was the optics set up (large field of view, proper particle seeding) which limits making better measurements close to the wall and gas–liquid interface. This can be done by considering a smaller field of view (higher spatial resolution)
4. To provide better insight into the wake interaction with the falling film, film thickness and velocity measurements should be undertaken in the falling film at different viscosities and flow rates. Such measurements will reveal the hydrodynamics of the falling film (turbulent, laminar).

5. To provide a better understanding of the coalescence of two Taylor bubbles, PIV measurements in the liquid ahead of the trailing bubble should be performed. This requires a bubbles injection mechanism that is capable of consistently releasing two bubbles a specific distance apart.

References

Adrian, R. J., (1991), Particle-imaging techniques for experimental fluid mechanics, *Annu. Rev. Fluid Mech.* 23, 261-304.

Adrian R. J., (2005), Twenty years of particle image velocimetry, *Exp. Fluids*, 39,159–169.

Adrian, R. J. and Westerweel, J., (2011), *Particle Image Velocimetry*, Cambridge University Pres, New York, USA.

Adrian, R.J., Christensen, K.T., (2000), Analysis and interpretation of instantaneous turbulent velocity field, *Exp. Fluids* 29, 275-290.

Aladjem Talvy, C., Shemer, L., and Barnea, D., (2000), On the interaction between two consecutive elongated bubbles in a vertical pipe, *Int. J. Multiphase Flow* 26, 1905-1932.

Angeli, P. and Gavriilidis, A., (2007), Hydrodynamics of Taylor flow in small channels: a review, *Proc. IMechE.* 222, 737-751.

Araújo, J.D.P., Miranda, J.M., Pinto, A.M.F.R., Campos, J.B.L.M. (2012), Wide-ranging survey on the laminar flow of individual Taylor bubbles rising through stagnant Newtonian liquids, *Int. J. Multiphase Flow* 43, 131-148.

Araújo, J.D.P., Miranda, J.M., Campos, J.B.L.M. (2013), Flow of two consecutive Taylor bubbles through a vertical column of stagnant liquid – A CFD study about the influence of the leading bubble on the hydrodynamics of the trailing one, *Chem. Eng. Sci.* 97, 16-33.

ASME (2005), PTC 19.1, Test Uncertainty, ASME, New York.

Brown, R.A.S., (1965), The mechanism of large bubbles in tubes I. Bubble velocities in stagnant liquids, *Can. J. Chem. Eng.* 43, 217-223.

Bugg, J. D., Mack, K., and Rezkallah, K.S., (1998), A numerical model of Taylor bubbles rising through stagnant liquids in vertical tubes, *Int. J. Multiphase flow* 24, 271-281.

Bugg, J.D. and Rezkallah, K.S. (1998), An analysis of noise in PIV images, *J. Visualizatio,* 1(2), 217-226.

Bugg, J.D. and Saad, G.A. (2002), The velocity field around a Taylor bubble rising in a stagnant viscous fluid: numerical and experimental results, *Int. J. Multiphase Flow* 28, 791-803.

Campos, J.B. L.M. and Guedes de Carvalho, J.R.F., (1988), An experimental study of the wake of gas slugs rising in liquids, *J. Fluid. Mech.* 196, 27-37.

Clift, R., Grace, J.R., and Weber, M.E. (1978), *Bubbles, Drops, and Particles*, Academic Press Inc., London, UK.

Coppus, J.H.C., Rietema, K. and Ottengraf, S.P.P. (1977), Wake phenomena behind spherical-cap bubbles and spherical-cap bodies. *T. I. Chem. Eng-Lond*, 55, 122-129.

Davies, R.M. and Taylor, G.I., (1950), The mechanics of large bubbles rising through liquids in tubes, *P. Roy. Soc. Lond. A* 200, 375-390.

DeJesus, J.D., Ahmad, W., and Kawaji, M., (1995), Experimental study of flow structure in vertical slug flow, *Proc. 2nd ICMF*, Kyoto, April 3-7.

Fabre, J. and Line, A. (1992), Modeling of two-phase slug flow, *Ann. Rev. Fluid Mech.*, 24, 21-46.

Goldsmith, H.L., and Mason, S.G., (1962), The movement of single large bubbles in closed vertical tubes, *J. Fluid Mech*. 14, 42-54.

Griffith, P. and Wallis, G.B. (1961), Two-phase slug flow, *ASME J. Heat Transfer* 83, 307–320.

Hart, D. (2000), PIV error correction, *Exp. Fluids* 29, 13-22.

Huang H., Dabiri D., and Gharib M. (1997), On errors of digital particle image velocimetry. *Meas. Sci. Technol.* 8, 1427–1440.

Kang, C.W., Quan, S., and Lou, J., (2010), Numerical study of a Taylor bubble rising in stagnant liquids, *Phys. Rev. E* 81, (6) 066308.

Keane R. D. and Adrian R. J., (1990), Optimization of particle image velocimetry: I. double pulsed systems, *Mea. Sci. Technol.* 1, 1202–1215

Li, X., Tian, W., Chen, R., Su, G.,and Qiu, S. (2013), Numerical simulation on single Taylor bubble rising in LBE using moving particle method, *Nucl. Eng. Des*. 256, 227–234

Liu, Y., Wang, P.Y, Wang, J., and Du, Z.H. (2013), Investigation of Taylor bubble wake structure in liquid nitrogen by PIV technique, *Cryogenics* 55-56, 20-29.

Lourenco L.M. and Krothapalli A. (1995), On the accuracy of velocity and vorticity measurements with PIV, *Exp Fluids* 18(6):421–428

Lu, X. and Prosperetti, (2009), A numerical study of Taylor bubbles, *Ind. Eng. Chem. Res.*, 48, 242–252.

Mao, Z.S. and Dukler, A. E., (1991), The motion of Taylor bubbles in vertical tubes II: Experimental data and simulations for laminar and turbulent flow, *Chem. Eng. Sci.* 46, 2055-2064.

Mayor,T.S., Ferreira, V., Pinto, A.M.F.R., and Campos, J.B.L.M., (2007), Hydrodynamics of gas-liquid slug flow along vertical pipes in laminar regime: experimental and simulation study, *Ind. Eng. Chem. Res.* 46, 3794-3809

Mayor, T.S., Ferreira, V., Pinto, A.M.F.R., and Campos, J.B.L.M., (2009), Hydrodynamics of gas-liquid slug flow along vertical pipes in turbulent regime an experimental study, *Int. J. Heat and Fluid Flow* 29, 1039-1053.

Moissis, R. and Griffith, P., (1962), Entrance effects in two-phase flow, *ASME J. Heat Transfer* 84, 366-370.

Nicklin, D. J., Wilkes, J. O. and Davids, J. F. (1962), Two-phase flow in vertical tubes, *T. I. Chem. Eng. Lond.* 40, 61–68.

Nogueira, S., Sousa, R.G., Pinto, A.M.F.R., Riethmuller, M.L., and Campos, J.B.L.M., (2003), Simultaneous PIV and pulsed shadow technique in slug flow: a solution for optical problems, *Exp. Fluids* 35, 598–609.

Nogueira, S., Riethmuller, M.L., Campos, J. B. L.M., and Pinto, A.M.F.R., (2006a), Flow in the nose region and annular film around a Taylor bubble rising through vertical columns of stagnant and flowing Newtonian liquids, *Chem. Eng. Sci*. 61, 845–857.

Nogueira, S., Riethmuller, M.L., Campos, J. B. L.M., and Pinto, A.M.F.R., (2006b), Flow patterns in the wake of a Taylor bubble rising through vertical columns of stagnant and flowing Newtonian liquids: an experimental study, *Chem. Eng. Sci*. 61, 7199-7212

Overmars E.F.J., Warncke, N.G.W., Poelma, C., and Westerweel, J. (2010), Bias errors in PIV: the pixel locking effect revisited, *15th Int. Symp. on Applications of Laser Techniques to Fluid Mechanics*, Lisbon, Portugal, July 05-08.

Pinto, A. M. F. R., Coelho Pinheiro, M.N., and Campos, J.B.L.M., (1998), Coalescence of two gas slugs in co-current flowing liquid in vertical tubes, *Chem. Eng. Sci*. 53, 2973-2983.

Pinto, A.M.F.R. and Campos, J.B.L.M., (1996), Coalescence of two gas slugs in a vertical column of liquid, *Chem. Eng. Sci*. 51, 45-54.

Polonsky, L., Barnea, S., and Shemer, D., (1999a), Averaged and time-dependent characteristics of the motion of an elongated bubble in a vertical pipe, *Int. J. Multiphase flow* 25, 795-812.

Polonsky, S., Shemer, L., and Barnea, D., (1999b), The relation between the Taylor bubble motion and the velocity field ahead of it, *Int. J. Multiphase Flow* 25, 957-975.

Prasad, A.K., Adrian, R.J., Landreth, C.C., and Offutt, P.W. (1992), Effect of resolution on the speed and accuracy of particle image velocimetry interrogation, *Exp. Fluids* 13, 105-116.

Quan, S.P., (2011), Co-current flow effects on a rising Taylor bubble, *Int. J. Multiphase Flow* 37, 888-897.

Raffel, M., Willert, C. and Kompenhans, J., (2007), *Particle Image Velocimetry: Practical Guide*, Springer, Berlin.

Saad, G.A., (1999), Particle image velocimetry measurements around a rising Taylor bubble, *M.Sc.Thesis*, Department of Mechanical Engineering, University of Saskatchewan, Saskatoon.

Shemer, L., Gulitski, A. and Barnea, D, (2005), Experiments on the turbulent structure and void fraction distribution in the Taylor bubble wake, *Multiphase Sci. Technol.* 16.1, 103-122.

Shemer, L., Gulitski, A. and Barnea, D, (2007), On the turbulent structure in the wake of Taylor bubbles rising in vertical pipes. *Phys. Fluids* 19. 035108-(1-13)

Shinneeb, A.M. (2006), Confinement effects in shallow water jets, *Ph.D. Thesis*, Department of Mechanical Engineering, University of Saskatchewan, Saskatoon.

Shinneeb, A.-M., Bugg, J.D., and Balachandar, R. (2004), Variable threshold outlier identification in PIV data, *Meas. Sci. Technol* 15, 1722-1732.

Sotiriadis, A.A. and Thorpe, R.B. (2005), Liquid re-circulation in turbulent vertical pipe flow behind a cylindrical bluff body and a ventilated cavity attached to a sparger, *Chem. Eng. Sci*. 60, 981-994.

Sousa, R.G., Riethmuller, M.L., Campos, B.L.M. and Pinto, A.M.F.R. (2005), Flow around individual Taylor bubbles rising in stagnant CMC solutions: PIV measurements, *Chem. Eng. Sci.*, 60, 1859-1873.

Taha, T. and Cui, Z.F., (2006), CFD modeling of slug flow in vertical tubes, *Chem. Eng. Sci.* 61, 676-687.

Taylor, A.M.K.P. and Whitelaw, J.H., (1984), Velocity characteristics in the turbulent

near wakes of confined axisymmetric bluff bodies, *J. Fluid Mech.* 139, 391- 416.

Tomiyama, A., Sou, A. and Sakacuchi, T. (1996), Numerical simulation of a Taylor bubble in stagnant liquid inside a vertical pipe, *JSME Int. J.*, Series B, 39, No. 3.

Tudose, E.T. and Kawaji, K., (1999), Experimental investigation of Taylor bubble acceleration mechanism in slug flow, *Chem. Eng. Sci.*, 54, 5761–5775.

van Hout, R., Barnea, S. and Shemer, D., (2002b), Translational velocities of elongated bubbles in continuous slug flow, *Int. J. Multiphase Flow* 28, 1333-1350.

van Hout, R., Gulitski, A., Barnea, S., and Shemer, D., (2002a), Experimental investigation of the velocity field induced by a Taylor bubble rising in stagnant water, *Int. J. Multiphase Flow* 28, 579-596.

Vassalow, P. and Kumar, J., (1997), PIV velocity measurements in the wake of an obstruction simulating a Taylor bubble in a duct, *ASME Fluids Eng. Div. Summer Meet.*, Vancouver, Canada.

Wakuda, K., (1999), The coalescence mechanism of multiple slug bubbles, *JSME, the 7th ICONE*, Tokyo, Japan, April 19-23.

Westerweel, J., Dabiri, D., and Gharib, M. (1997), The effect of a discrete window offset on the accuracy of cross-correlation analysis of digital PIV recordings, *Exp. Fluids* 23, 20-28.

White, E.R., Beardmore, R.H., (1962), The velocity of rise of single cylindrical air bubbles through liquids contained in vertical tubes, *Chem. Eng. Sci*. 17, 351-361.

Zheng, D. and Che, D., (2006), Experimental study on hydrodynamics characteristics of upward gas-liquid slug flow, *Int. J. Multiphase Flow* 32, 1191-1218.

Zukoski, E.E, (1966), Influence of viscosity, surface tension, and inclination angle on the motion of long bubbles in closed tubes, *J. Fluid Mech.* 25, 821-837.

Appendix A: Taylor Bubble Terminal Velocity

The Taylor bubble rise velocity measurements are used to set the separation time between the lasers pulses in the PIV measurements. In addition, they are used to estimate the time for the bubble to travel from the lower phase detector to the measurement location. This time is used to adjust the PIV system delay trigger time and thereby position the bubble at any desired location in the measurements plane.

The terminal velocities were measured using the phase transition detectors described in Section 3.1.2. The distance between the detectors was 1 m. The lower detector was placed 3 m above the bubble release valve. The transit time was measured from the phase detector signal using a digital oscilloscope.

Figure A-1 shows the Taylor bubble rise velocity in stagnant water. For a tube which is open to the atmosphere at the top, the rise velocity of the Taylor bubble increases with the bubble size. This is due to the fact that the bubble expands as it rises. The rise velocity of a Taylor bubble is affected by the velocity of the liquid ahead of it. This was experimentally confirmed by Polonsky *et al*. (1999b) and Sousa *et al*. (2006). They showed that the growth of the bubble induces an increase in the bubble velocity and a corresponding displacement of the liquid ahead of it. In contrast to an open-top tube, the rise velocity of the bubble for closed-top tube is constant regardless of the bubble size.

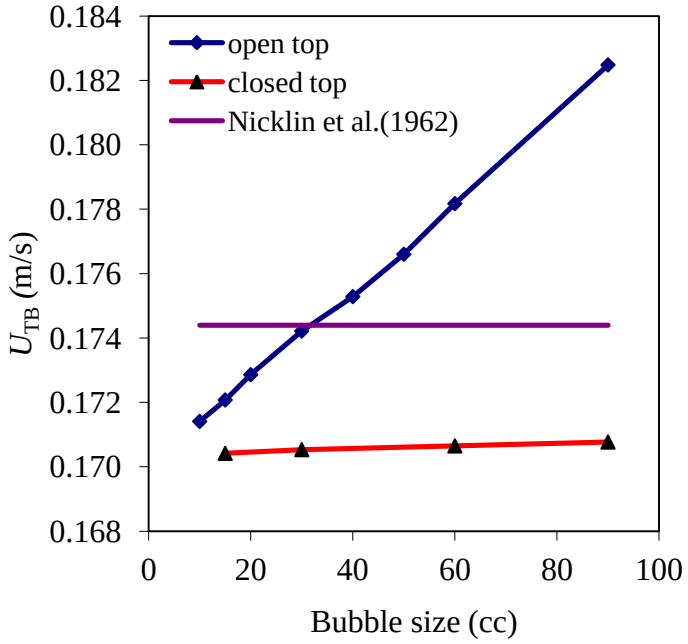

Figure A-1: The velocity of Taylor bubbles rising in stagnant water

The Taylor bubble rise velocities were also calculated using the following equation by Nicklin *et al*. (1962),

$$U_{TB} = CU_L + 0.35\sqrt{gD}, \qquad \text{(A.1)}$$

where the constant C takes the value of 1.2 when the liquid flow regime is turbulent.

The rise velocity of Taylor bubbles in concurrent upward flowing water is presented in Figure A-2. For a given liquid velocity, the rise velocity increases with increasing bubble size. However, this effect of bubble size on the rise velocity tends to decrease as the liquid flow rate increases. This is due to the fact that the contribution of the bubble expansion to the velocity ahead of the bubble becomes very low. At a liquid velocity of 0.29 m/s (*Re* =7,660), the Nicklin equation goes from underestimating (for bubble size of 10 cc) the

bubble velocity (for bubble size of 10 cc) to overestimating (for bubble size of 60 cc) the bubble velocity by 22%. This error decreases as the liquid velocity increases and becomes 2% for the liquid velocity of 1.59 m/s. Another observation from the data is that, for a given bubble size, the length of the bubble increases with increasing flow rate. This indicates that the film thickness increases with increasing flow rate.

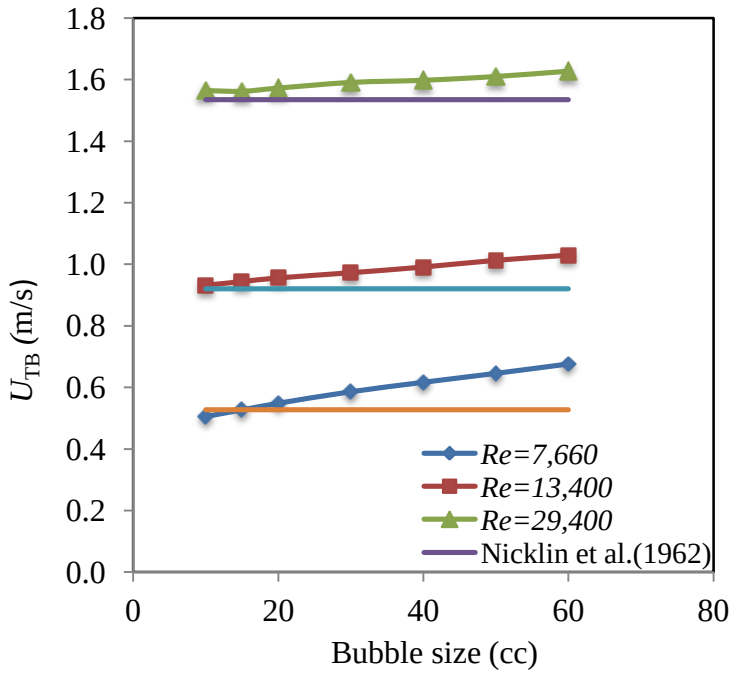

Figure A-2: The velocity of Taylor bubble rising in concurrent upward flowing water

Appendix B: Shape of the Bottom Surface of Taylor Bubbles at Different Flow Conditions

The following figures show instantaneous shape of the bottom of Taylor bubbles rising in stagnant and upward flowing liquids. These images were extracted from PIV images and enhanced using Matrox Inspector® image processing software. In these images, the bottom part of the bubble, part of the near wake, and the falling film region can be seen clearly. The bright dots in the images are the PIV seeding particles.

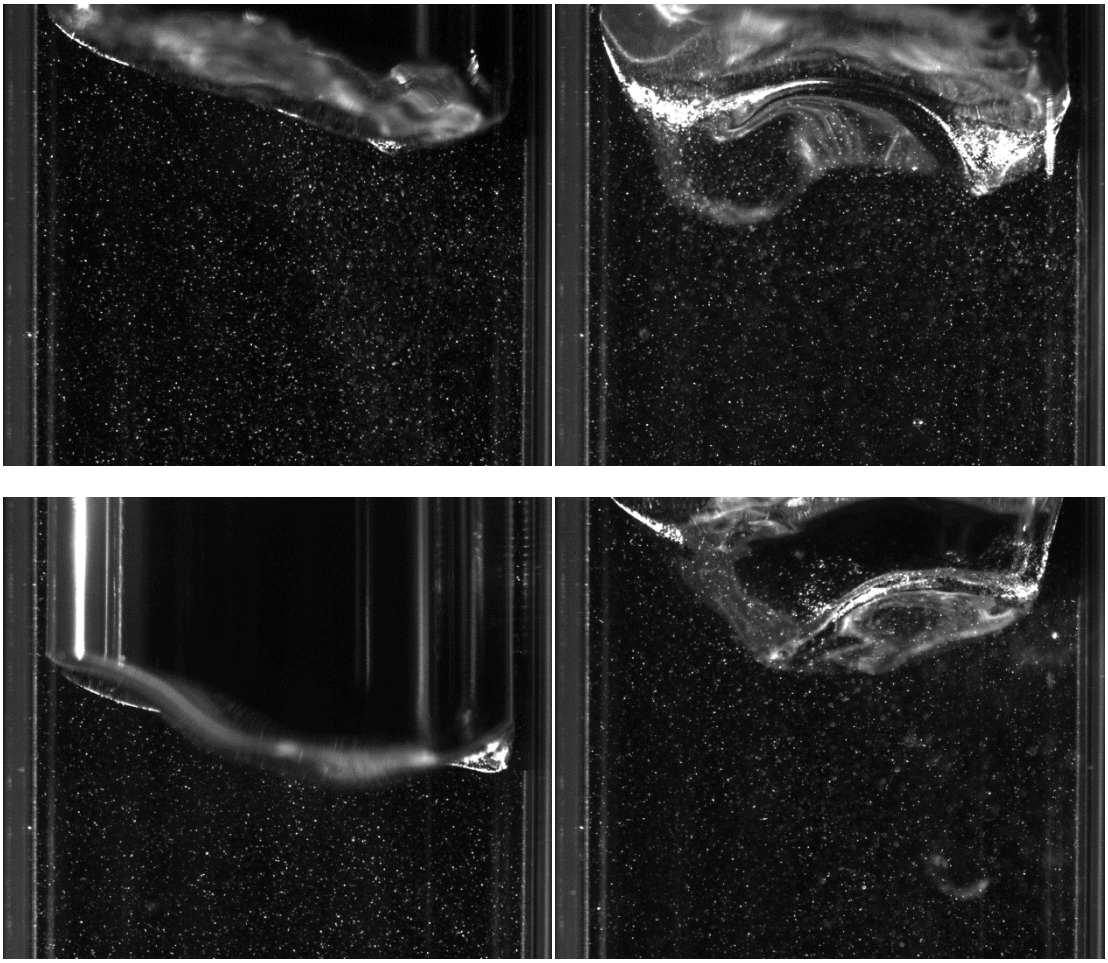

Figure B-1: Shape of the bottom surface of Taylor bubbles rising in stagnant liquid Case 1 (Re_{TB} = 4,400, N = 12,600).

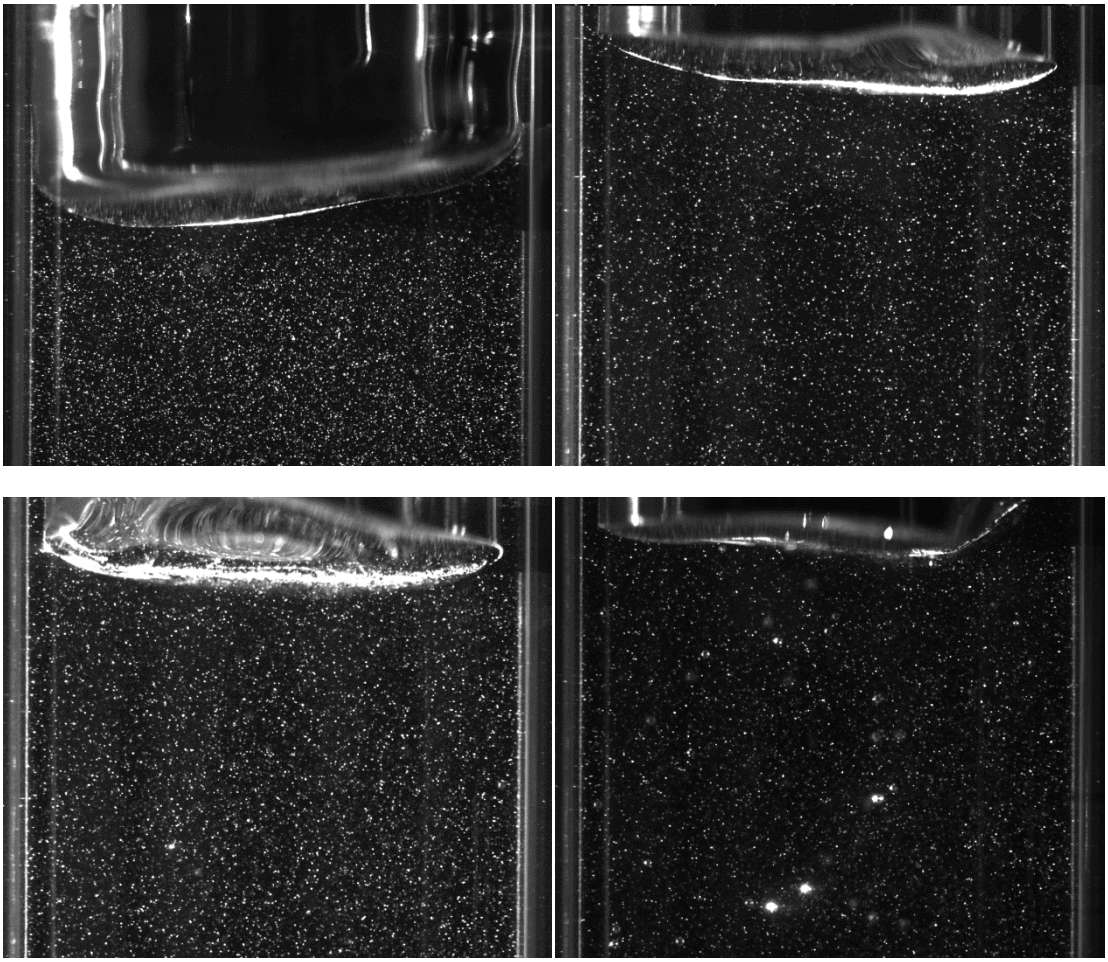

Figure B-2: Shape of the bottom surface of Taylor bubbles rising in stagnant liquid Case 2 (Re_{TB} = 1,000, N = 2,850).

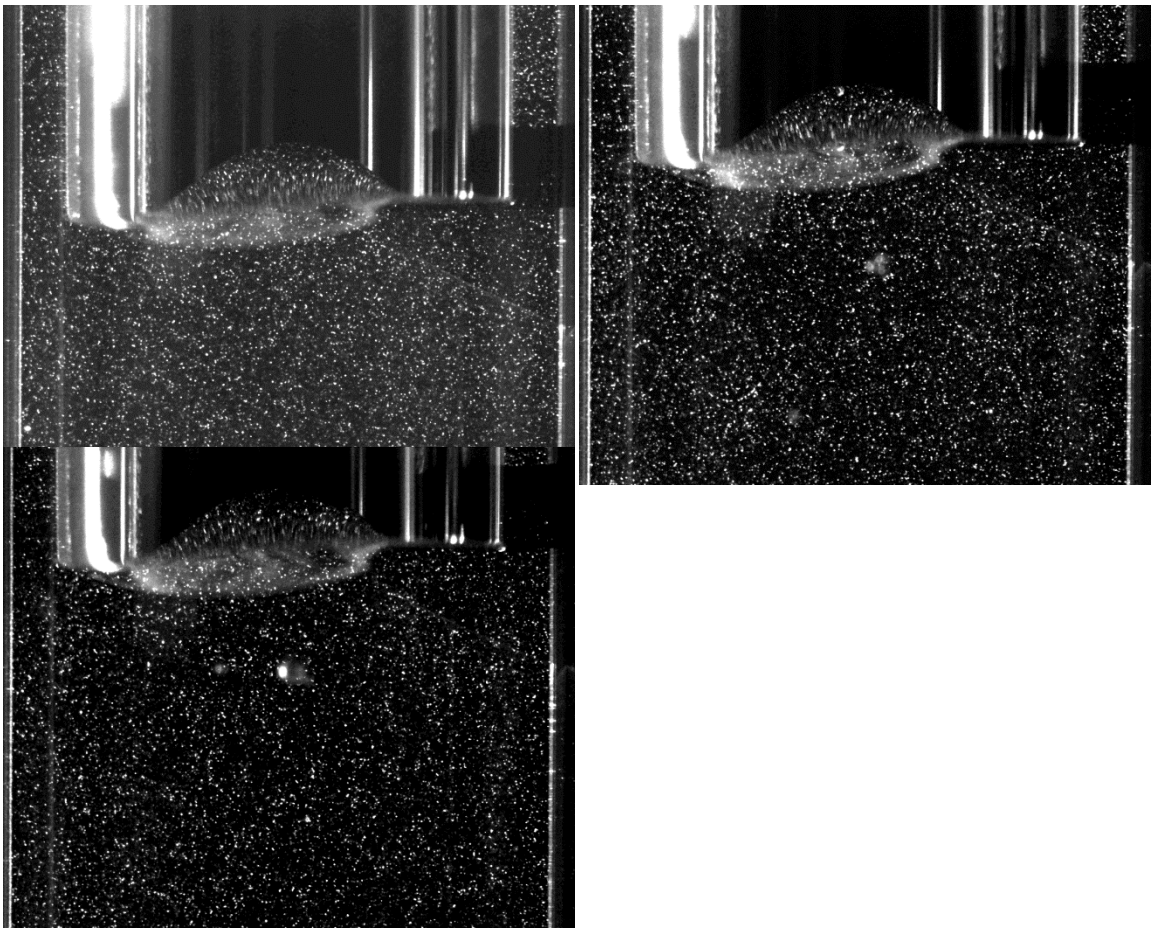

Figure B-3: Shape of the bottom surface of Taylor bubbles rising in stagnant liquid Case 3 (Re_{TB} = 120, N = 352).

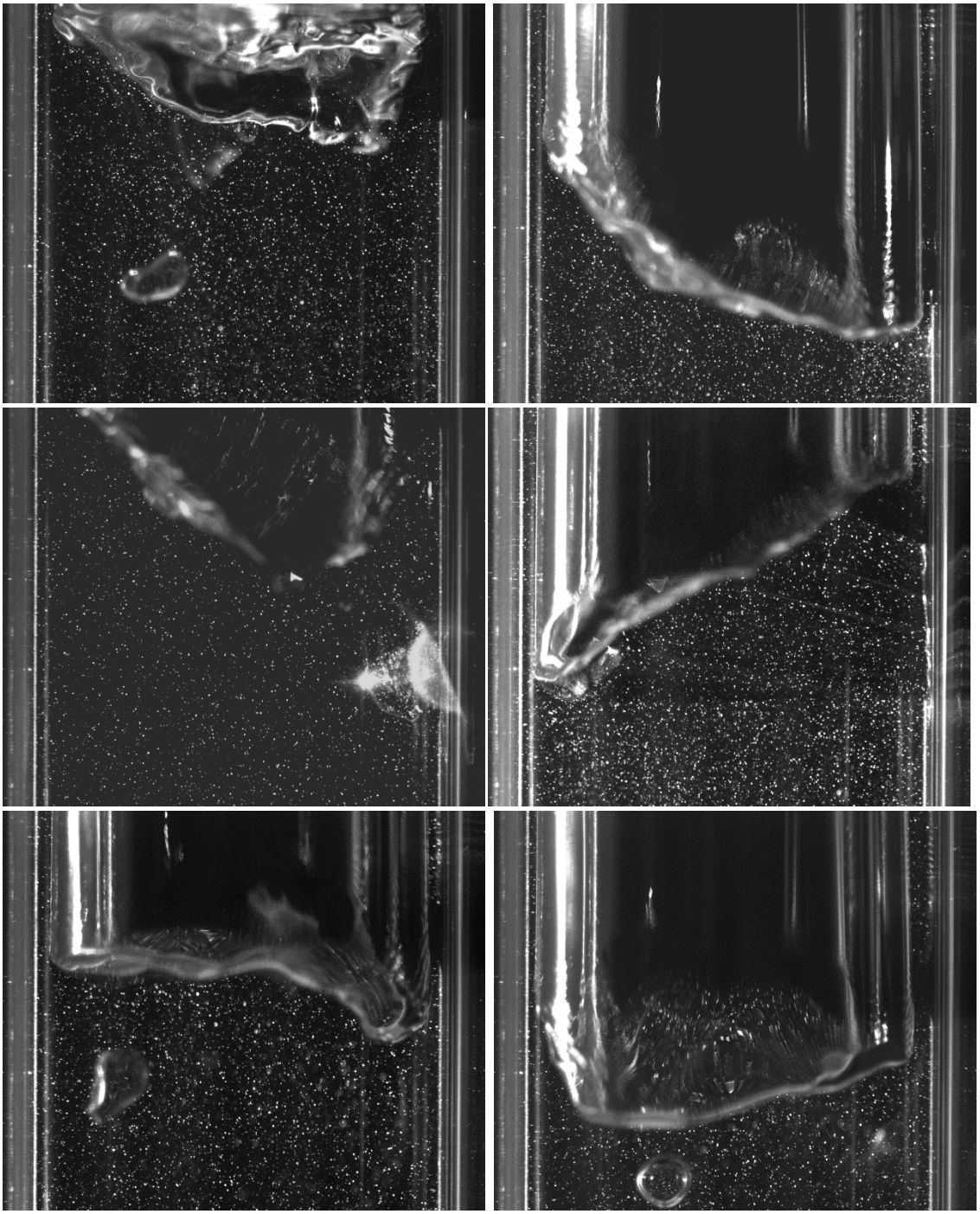

Figure B-4: Images of the bottom surfaces of Taylor bubbles rising in upward flowing water under Case 4 (Re_{TB} = 15,400, Re_{L} = 9,200)

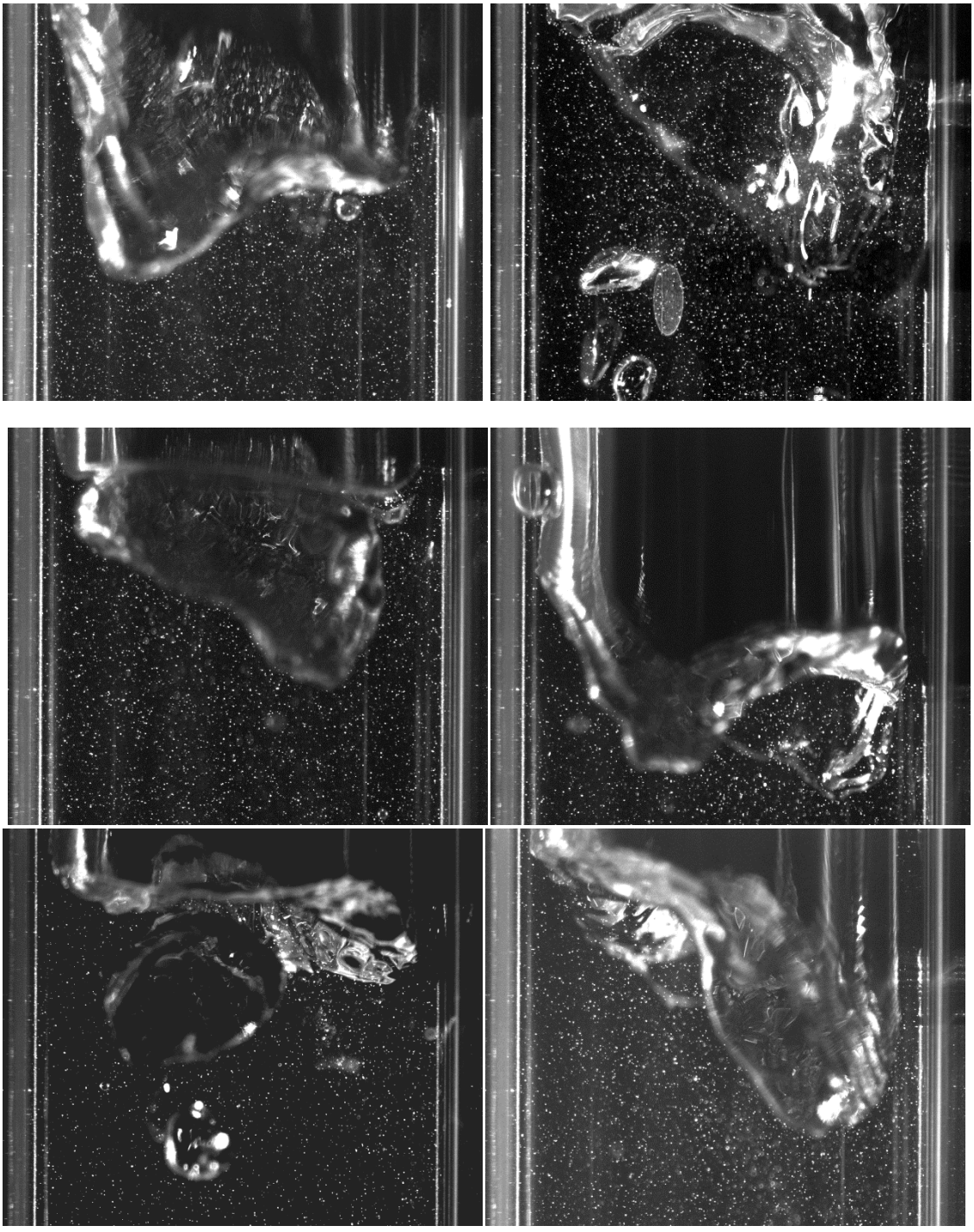

Figure B-5: Images of the bottom surfaces of Taylor bubbles rising in upward flowing water Case 5 (Re_{TB} = 20,700, Re_{L} = 13,600)

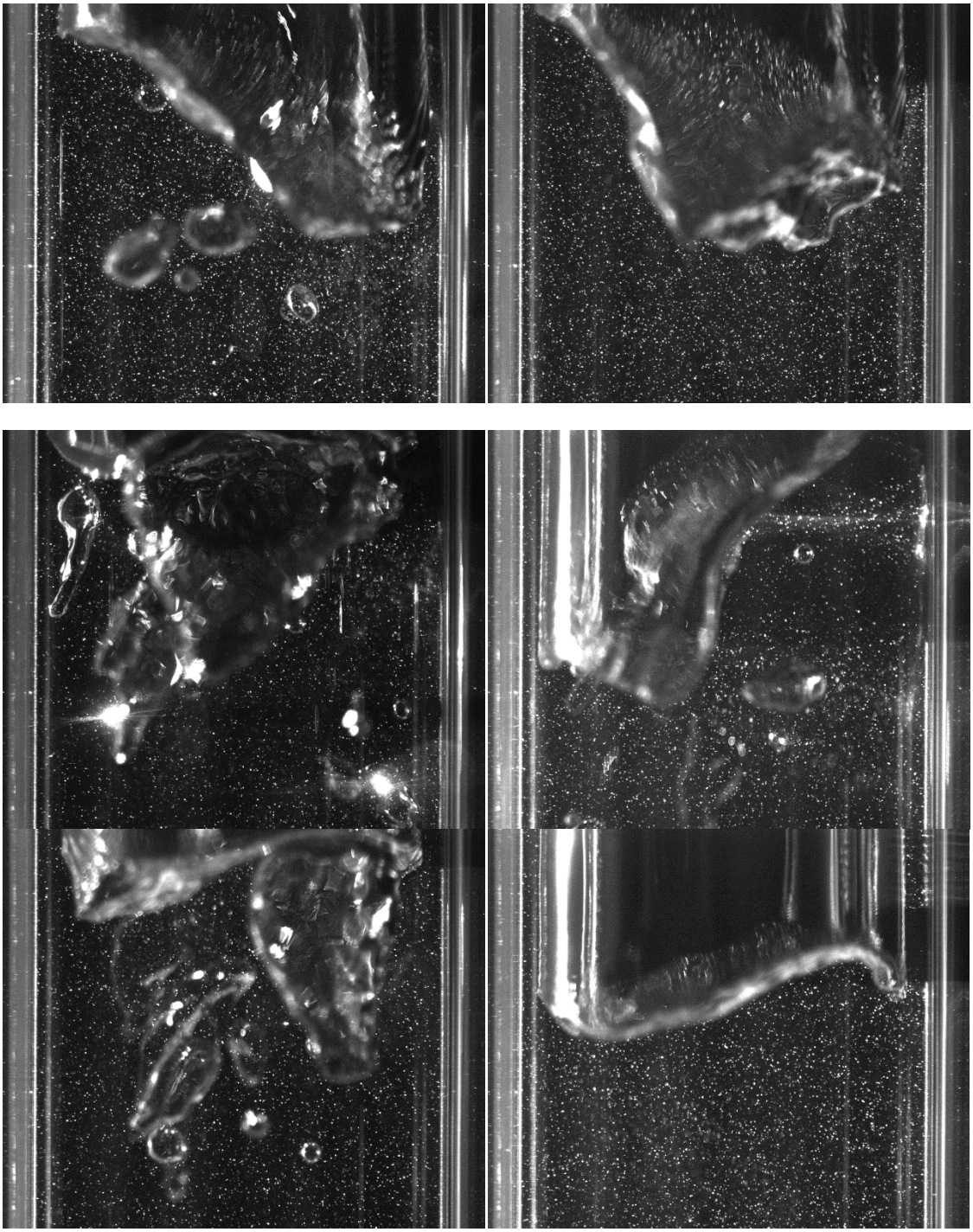

Figure B-6: Images of the bottom surfaces of Taylor bubbles rising in upward flowing water Case 6 (Re_{TB} = 25,800, Re_{L} = 17,800)

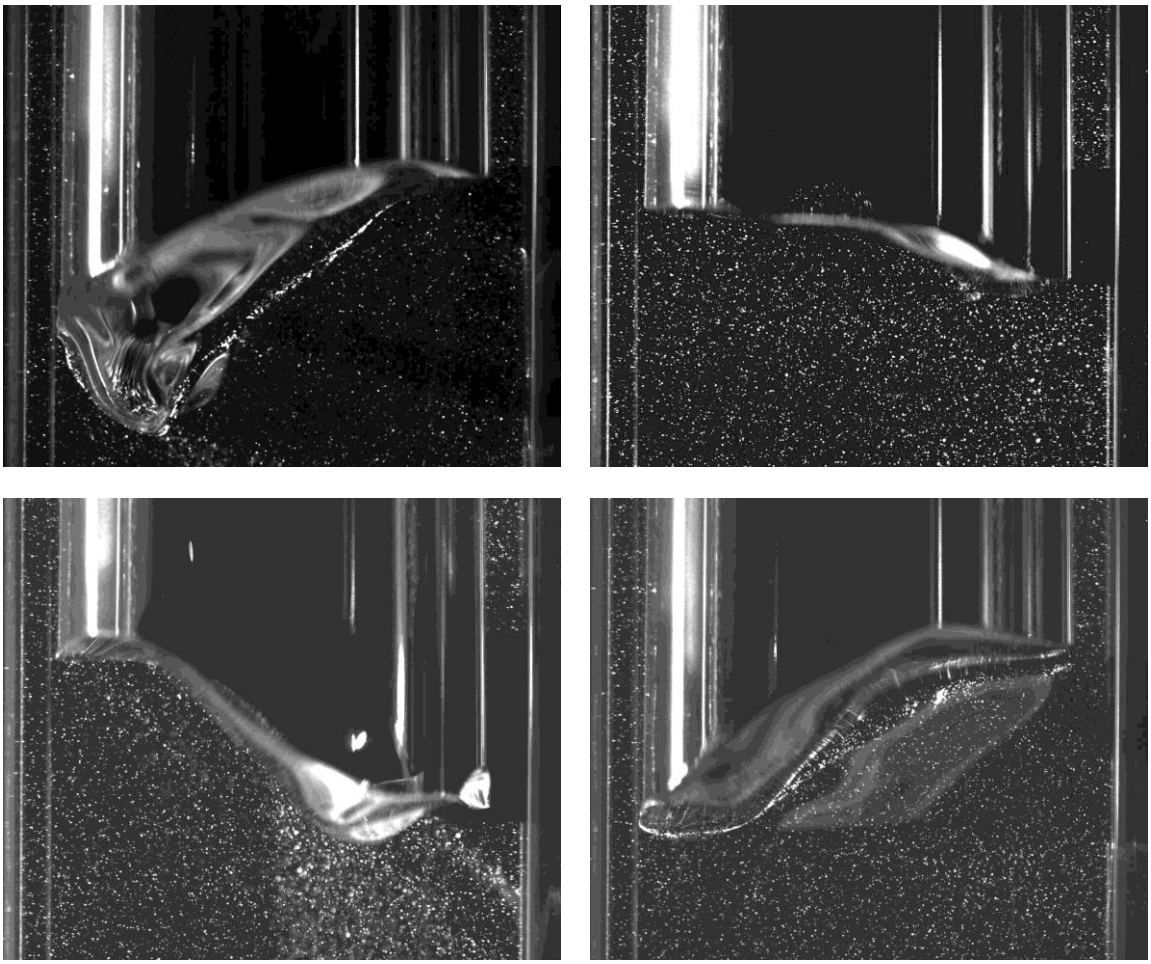

Figure B-7: Bottom surfaces of Taylor bubbles rising in an upward flowing mixture of water and glycerol: (a) Case 7 (Re_{TB} = 3,800 & Re_{L}= 1,500)

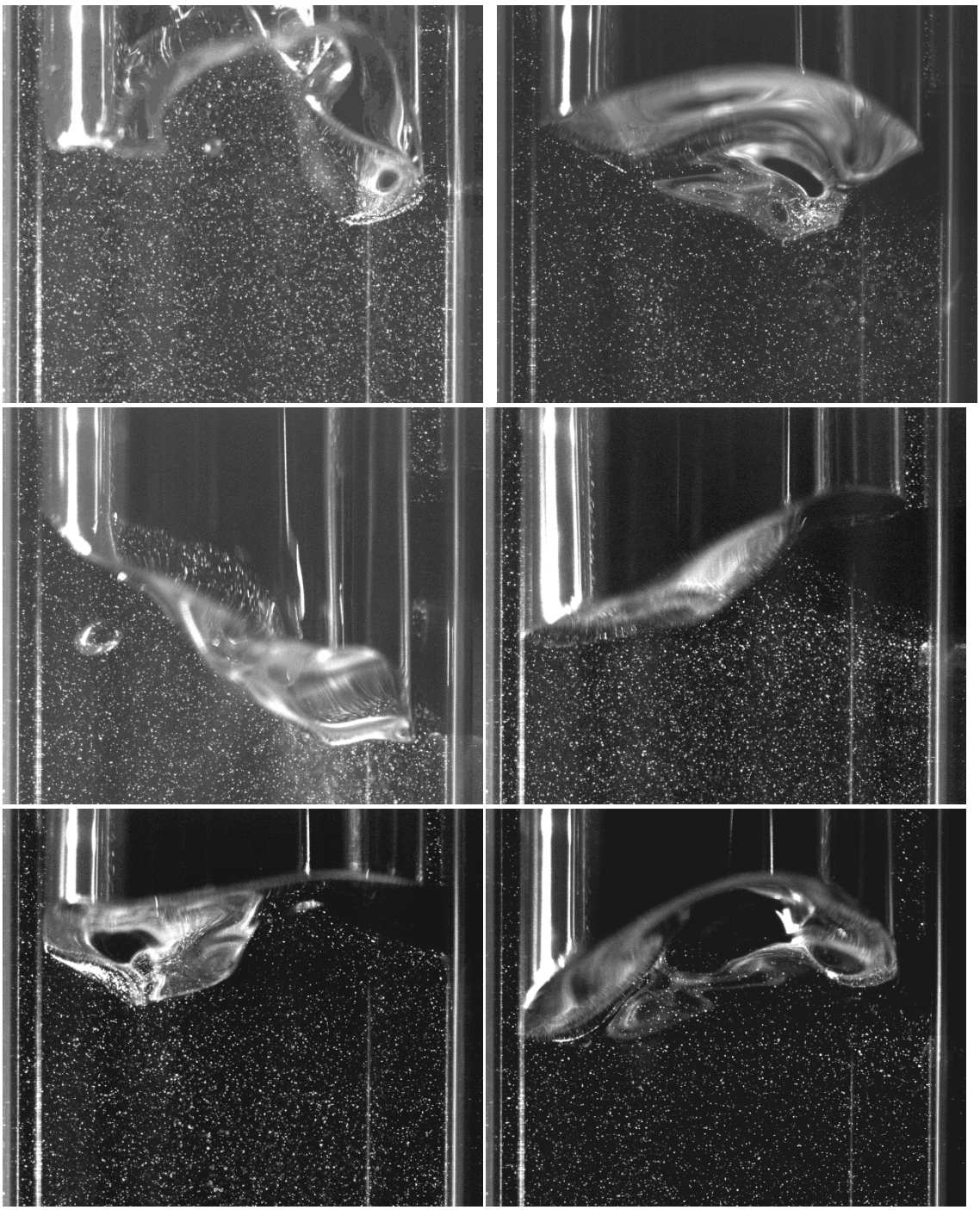

Figure B-8: Bottom surfaces of Taylor bubbles rising in an upward flowing mixture of water and glycerol Case 8 (Re_{TB} = 5,700 & Re_{L} = 4,000)

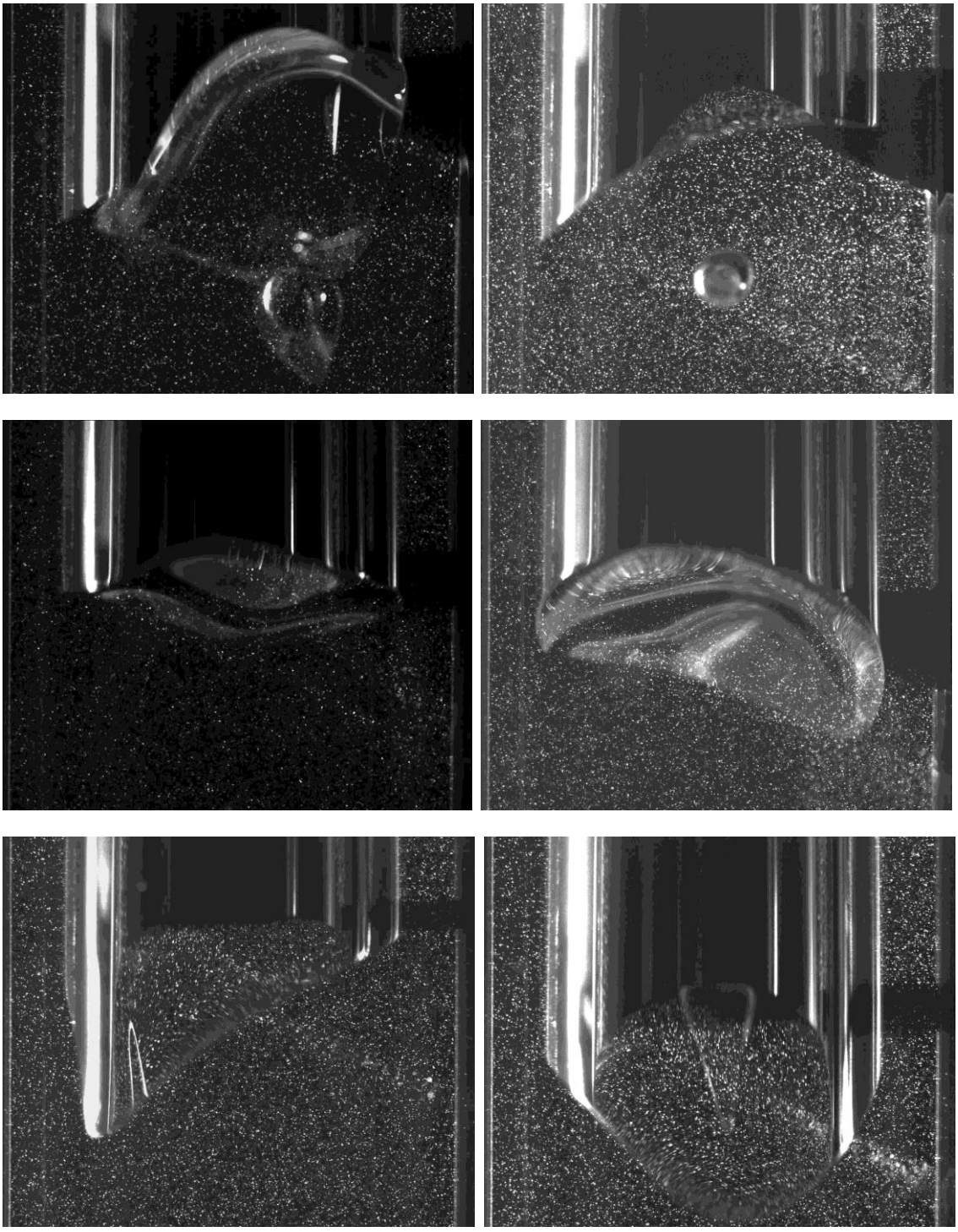

Figure B-9: Bottom surface of a Taylor bubble rising in upward flowing mixture of water and glycerol: Case 9 (Re_{TB} = 620 & Re_{L} = 260)